GENERATION OF OLIGODENDROCYTES AND CHARACTERISATION OF THEIR ROLE IN AXONAL SUPPORT

Liliana Domingues Pedro

Graduate School of Systemic Neurosciences

LMU Munich

Dissertation der
Graduate School of Systemic Neurosciences der
Ludwig-Maximilians-Universität München

15th June, 2022

Supervisor:
Prof. Dr. Mikael Simons
Institute of Neuronal Cell Biology,
Technical University Munich
German Centre for Neurodegenerative Diseases (DZNE)

First Reviewer: Prof. Dr. Mikael Simons
Second Reviewer: Prof. Dr. Dominik Paquet
Third Reviewer: Dr. Sarah Jäkel

Date of Submission: 15 of June of 2022
Date of Defence: 17 of February of 2023

Table of Contents

Abstract

Glial cells, comprising of oligodendrocytes, astrocytes and microglia, have come a long way from their simplistic description as nerve glue. Today, we know that neuron-glia interactions are a fundamental aspect of neuronal function and brain homeostasis. Oligodendrocytes (OLGs) are the myelinating glia of the central nervous system forming myelin sheaths that enwrap axons. These cells are involved in axonal maintenance and survival, neuronal circuitry adaptation and immunomodulation. However, many aspects of oligodendrocyte physiology and pathology are still not completely understood. Factors that have contributed to the knowledge gaps associated with these cells include the complicated and inefficient protocols for the isolation of primary cells, the lack of defined stage specific markers and of adequate transgenic tools that would allow the manipulation of these cells *in vitro*.

In this thesis I conducted a comparative study to evaluate the differentiation efficiency of OLGs derived from human induced pluripotent stem cells (iPSCs) via the ectopic expression of oligodendrocyte transcription factors. I aimed to provide benchmarking criteria for the reproducibility and robustness of iPSC derived OLGs (iOLGs) protocols. I observed that iPSCs overexpressing solely SOX10 differentiated, at low yields, into O4 and MBP expressing iOLGs, while overexpression of a combination of three transcription factors, SOX10, OLIG2 and NKX6.2 (SON) lead to a higher differentiation efficiency. By including a purification step I significantly improved oligodendrocyte differentiation yields and reduced the population heterogeneity. The gene expression profile of SON-induced iOLGs confirmed the expression of oligodendrocyte differentiation markers. Furthermore, using a co-culture platform with iPSC-derived neurons, astrocytes and microglia we showed that these cells can migrate within the culture and form myelin-like structures *in vitro*.

In this thesis I also aimed to address the wider knowledge gap of the mechanism of axonal support by myelinating oligodendrocytes. Oligodendrocytes secrete ferritin heavy chain (FTH1) protein, which may be internalised by neighbouring neurons and act as an antioxidant defence system by storing and detoxifying the excess of neuronal intracellular iron. Interestingly, *Fth1* mRNA is among the three most highly abundant transcripts found in purified myelin, despite not behaving like a myelin-resident protein. Given the importance of FTH1 protein for neuronal protection it is reasonable to expect that the targeted transport and local translation of *Fth1* mRNA could effectively provide a way for oligodendrocytes to rapidly respond to external stimuli. As such I aimed to characterise the nature of the *Fth1* transcript in oligodendrocytes. *Fth1* mRNA shows the characteristic granular distribution along the distal processes, reminiscent of other locally repressed mRNAs in both mouse and human oligodendrocytes. Moreover, *Fth1* mRNA is not associated with processing bodies or stress granules in mature oligodendrocytes, instead it appears to be a unique type of cytoplasmic RNA. To identify the RNA-binding proteins that promote *Fth1* mRNA localization or translation repression,

I developed a proteomics approach to selectively isolate native RNA-protein complexes. I identified 19 potential protein candidates that could be associated with *Fth1* mRNA translocation and/or translation repression in oligodendrocytes.

In conclusion, our study is the first step to establish a standardised method for oligodendrocyte differentiation via ectopic transcription factor expression. Indeed, continuous improvement of the established protocols will allow the development of reproducible and cost-effective human iPSC-derived oligodendrocyte models and ultimately facilitate the utilisation of the iPSC technology to study the mechanisms and pathways of human OLG migration and myelination. In addition, our study also suggests the existence of a previously unknown RNA trafficking mechanism for *Fth1* mRNA and local protein translation in myelin. We also identified potential *Fth1* mRNA binding proteins that could provide additional insights into the impact of neuronal cues in the regulation of FTH1 protein expression and secretion by oligodendrocytes.

Introduction

1. Oligodendrocytes are the myelin producing cells

Myelin evolved as an essential structure for the optimal function of the vertebrate nervous system. As body size increased the acquisition of myelin sheaths facilitated rapid impulse propagation while maintaining the small axonal diameter, effectively increasing neuronal processing speed and energetic efficiency (Zalc 2016; Hill et al. 2018).

In the central nervous system (CNS) myelin sheaths are produced by oligodendrocytes (OLGs) and in the peripheral nervous system by Schwann cells. Despite sharing functional characteristics, these cells differ in developmental origin (OLG: subventricular zone; Schwann cells: neural crest), the number of myelinated axonal segments per cell (OLG: up to 60; Schwann cells: 1) and myelin protein composition (OLG: 17% (Patzig et al. 2011); Schwann cells: 0.2% of proteolipid protein (Jahn et al. 2009)). This thesis will focus on oligodendrocytes and CNS myelin, for a complete comparison between these two cell types, see reviews by Stassart et al. 2018 and Nave and Werner 2021.

Myelination is a multistep process, tightly controlled by intrinsic and extrinsic factors that coordinate various steps of proliferation to differentiation and myelination. During embryonic development oligodendrocyte precursor cells (OPCs) proliferate and migrate throughout the CNS. OPCs then differentiate into pre-myelinating oligodendrocytes (pre-mOLGs) that extend multiple processes towards permissive axons. Once committed to an axonal tract, pre-mOLGs initiate membrane outgrowth and axonal wrapping, differentiating into mature myelinating oligodendrocytes (mOLG) followed by myelin compaction and axonal domains formation (Simons and Nave 2015; Mitew et al. 2014).

Myelin sheaths are multilamellar lipid rich membranes that concentrically wrap around neuronal axons. Besides facilitating fast saltatory nerve conduction by accumulating sodium channels at the Nodes of Ranvier, myelin is also involved in maintaining axonal functional integrity (Frühbeis et al. 2013; Mukherjee et al. 2020) and neuronal trophic support (Du and Dreyfus 2002). New evidence also suggests that oligodendrocytes may also play a role in neuronal information processing (Moore et al. 2020) and immunomodulation (Falcão et al. 2018).

Given the complexity of the OLG differentiation process and the importance of myelin in CNS physiology, it is not surprising that oligodendrocyte and myelin dysfunction can lead to serious pathologies. Dys- and demyelinating diseases can be acquired or inherited and represent a large and heterogeneous group with very different etiologies and clinical pathophysiologies. Multiple Sclerosis, a chronic inflammatory disease, is among the most common myelin disorders. Other examples include autoimmune disorders, such as acute

disseminated encephalomyelitis, and hereditary diseases such as leukodystrophies (Stadelmann et al. 2019; Duncan et al. 2021). Myelin abnormalities are also found in many other neurological and psychiatric conditions such as Alzheimer's diseases (Nasrabady et al. 2018), amyotrophic lateral sclerosis (Lorente Pons et al. 2020) and schizophrenia (Cassoli et al. 2015).

In the last decades new research has expanded our understanding of oligodendrocyte development, myelin homeostasis and the importance of glia-neuron communication. However, recent studies have brought to light discrepancies between mouse and human oligodendrocyte transcriptome and mitogen response that should be considered when translating data from mouse models to the human physiology (van Tilborg et al. 2018; Bradl and Lassmann 2010). Technological developments in human OLGs derived from induced pluripotent stem cells (iPSCs) can complement and validate the translation of findings from animal models to the human situation.

The following sections will discuss general concepts of oligodendrocyte development and differentiation, emphasising the importance of studying human oligodendrocytes by summarising species-specific discrepancies. I will further elaborate on the role of mRNA active transport and local translation in the development of myelin. I will discuss recent evidence showcasing the role of ferritin heavy chain (FTH1) secretion in the support and maintenance of neuronal integrity by oligodendrocytes. Finally, I will summarise *in vivo* and *in vitro* mouse and human OLG models, with a focus on the different methods currently used to differentiate iOLG from iPSCs, establishing the need to develop a uniform methodology.

1.1. Oligodendrocyte development and differentiation

In both human and mouse CNS the course of oligodendrocyte differentiation follows a similar pattern and can be divided into distinct stages: oligodendrocyte precursor cell, pre-myelinating oligodendrocyte and myelinating oligodendrocyte. These stages can be characterised by specific cell morphologies and the expression of specific sets of transcription factors and protein markers (Czepiel et al. 2015) (Fig 1).

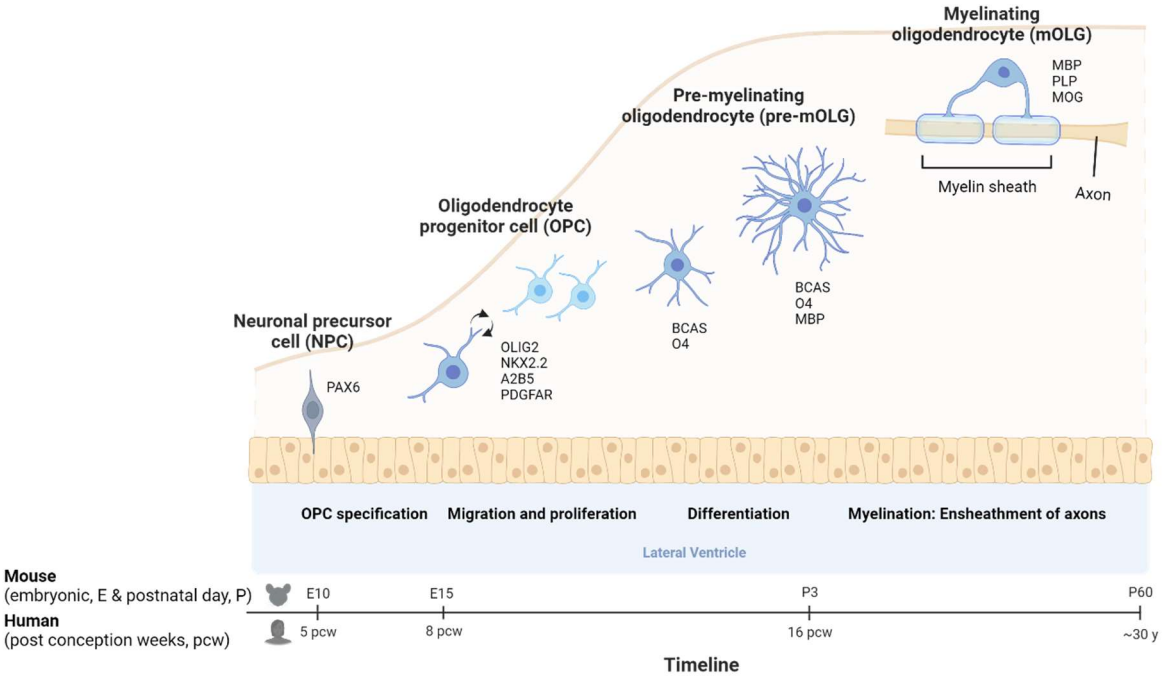

Fig 1 - Myelination is a multistep process, tightly controlled by intrinsic and extrinsic factors that coordinate various steps of oligodendrocyte proliferation and differentiation. Schematic illustration of the different stages of oligodendrocyte development from neuronal precursor cells until myelinating oligodendrocyte. Top: OLG precursor cells originate from neuroepithelial zones surrounding the ventricles, where NPCs differentiate into OPCs under the influence of OLG specific transcription factors OLIG2, NKX2.2, and SOX10. OPCs migrate and proliferate across the brain. At their final destination, OPCs will initiate differentiation into BCAS+ and O4+ pre-mOLGs, and finally into mature OLGs that produce myelin sheaths and wrap around neuronal axons. Myelination oligodendrocytes can be characterised by the expression of the myelin proteins MBP, CNP and MOG. Bottom: Parallel timelines of mouse and human oligodendrogliogenesis and myelinogenesis are shown. The time points were defined based on the expression of different oligodendrocyte lineage markers, adapted from Jakovcevski et al. 2009. Created with BioRender.com.

During development OPCs are generated in three sequential waves from the neuroepithelial zones surrounding the ventricles. Following the initial period of neurogenesis, neuronal precursor cells (NPCs) commit to the oligodendroglial lineage under the influence of morphogens like Sonic Hedgehog (Tong et al. 2015; Jakovcevski et al. 2009). Sonic Hedgehog activates cascades of transcription factors including NK2 homeobox 2 (NKX2.2) and oligodendrocyte transcription factor 2 (OLIG2) (Nery et al. 2001; Briscoe et al. 1999). OLIG2 induces the initial activation of SRY-box 10 (SOX10). Interestingly, SOX10 is both a target gene and an interactor of OLIG2 creating a positive feedback loop that maintains OLIG2 expression in SOX10-expressing cells (Küspert et al. 2011). With both of these transcription factors being considered oligodendroglial lineage markers.

OPCs are highly proliferative cells with a bipolar or tripolar morphology, expressing surface markers such as gangliosides recognized by the antibody A2B5 and the platelet-derived growth factor receptor alpha (PDGFRA) (Czepiel et al. 2015). Chemotactic cues

and mitogens like PDGFA and neurotrophin 3 (NT3) will promote OPC proliferation and inhibit differentiation in both human and mice cultures, allowing the OPCs to disperse throughout the forebrain. Conversely, basic fibroblast growth factor (FGF2) had no effect in human OPCs, despite well-documented mitogenicity and synergy with PDGFA in rodent culture systems (Mitew et al. 2014; Wilson et al. 2003).

Once the OPC population has achieved a relatively uniform distribution throughout the future white and grey matter, a fraction will differentiate into pre-myelinating oligodendrocytes. Some OPCs remain as stable residents throughout adulthood (5% of all cells in the mouse brain and 3% of all cells in the human brain) and are thought to be important for myelin maintenance, but also have functions beyond myelination (Gautier et al. 2015; Yeung et al. 2014).

Due to a limited set of reliable tools to visualise and manipulate pre-mOLG, considerably less is known about this state of oligodendrogenesis when compared to OPCs. Recently, the breast carcinoma amplified sequence 1 (BCAS1) (Fard et al. 2017) and the ectonucleotide pyrophosphatase/phosphodiesterase 6 (ENPP6) were identified as two markers for pre-myelinating and early myelinating oligodendrocytes (Xiao et al. 2016).

Pre-mOLGs are characterised by a highly branched morphology. These post-mitotic cells exist as a transient state between OPCs and myelinating oligodendrocytes. As OPCs exit the cell cycle, they undergo dramatic changes in chromatin organisation which is associated with the downregulation of proliferative response genes such as *WNT* and *PDGF* as well as the activation of myelin regulatory factor (*MYRF*) (Aprato et al. 2020; Goldman and Kuypers 2015; Emery et al. 2009). Once induced, MYRF mediates the progression of pre-mOLG to a mature myelinating stage by positively regulating the expression of myelin proteins such as myelin basic protein (MBP), proteolipid protein 1 (PLP1), myelin oligodendrocyte glycoprotein (MOG) and 2′,3′-cyclic nucleotide 3′-phosphodiesterase (CNP) (Emery et al. 2009).

In order to initiate myelination pre-mOLGs extend and retract their processes towards neurons to find permissive axons. To date, the question of which axonal factors or oligodendrocyte sensing molecules are involved in triggering myelination is still unknown. Despite this, several factors such as axonal calibre, neuronal activity and interactions with integrin and tyrosine kinase extracellular receptors have been show to control the extent and timing of myelination, but not whether myelination will occur (Stadelmann et al. 2019; Bradl and Lassmann 2010).

As the appropriate axon is selected, myelination is initiated and pre-mOLGs transition to myelinating oligodendrocytes. This transition is marked by rapid changes in plasma membrane architecture and composition. mOLGs synthesise and wrap several concentric layers of myelin around the axons (Fig 2A). Interestingly, the ensheathment of multiple axons by one oligodendrocyte appears to be a coordinated event, with all axons

ensheathed within 12–18 hours (Barres 2008; Czopka et al. 2013). Within such a short time frame, mOLGs have to produce and sort high amounts of membrane proteins and lipids. An additional complexity is that myelination is heavily dependent on the specific spatial distribution of the myelin proteins, with the individual components often sorted and transported by different mechanisms.

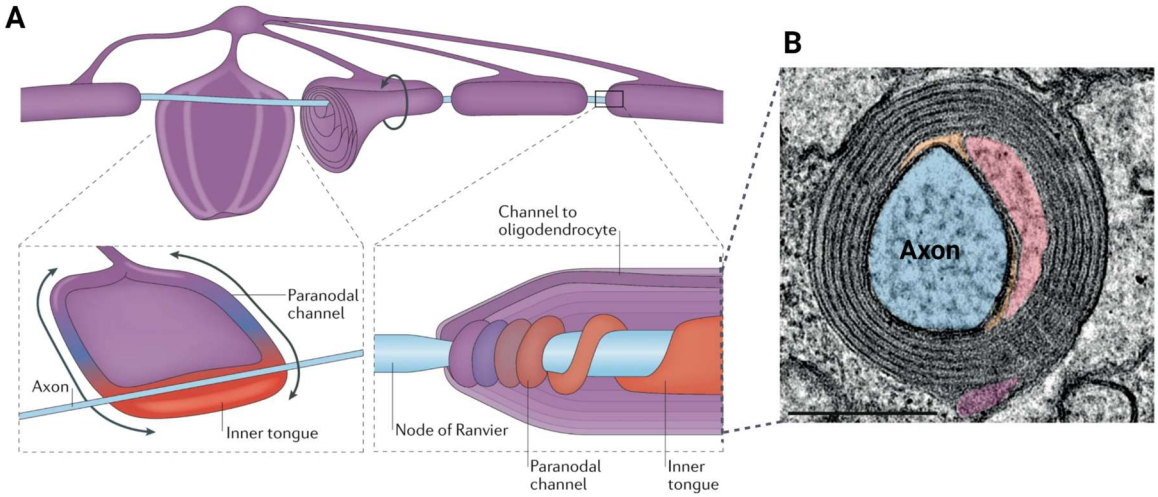

Fig 2 - Myelinating oligodendrocytes synthesise and wrap several concentric layers of myelin around the axons. (A) Schematic illustration of the myelin wrapping process. The myelin sheet comprises an inner compacted area (dark purple) and an outer cytoplasmic channel (light purple). Multiple concentric layers of myelin are wrapped around the axon to create the myelin sheath with an inner tongue (red) running along the axon. The outer edge of the myelin wraps, flanking the node of Ranvier, forms the paranodal loop structure. **(B)** Representative electron micrograph of a myelinated axon cross section. In the center of concentric layers of myelin, we can find the axon (blue). The inner (red) and outer (purple) myelin tongues, together with the periaxonal space (orange, small space between axon and myelin) are visible. The periodicity of myelin can be observed by the repeating sequence of thick major dense lines and the thin intraperiod lines. Even though the intraperiod lines appear as a single line, in reality they consist of two thin lines, corresponding to the closely apposed outer sides of the original cell membrane. The major dense lines are condensed cytoplasm. Scale bar 500 nM. Data source: Wolf et al. 2021.

The myelin multi-lamellar structure is achieved by three main myelin proteins PLP1, MBP and CNP. PLP1 and MBP are both proteins with adhesive function within the myelin sheath. Upon synthesis at the rough endoplasmic reticulum, PLP1 is transported via transcytotic vesicles to the myelin membrane (Baron et al. 2015). PLP1 contributes to the adhesion of the apposed external membrane surfaces (intraperiod lines on electron microscopy). MBP is locally translated at the cytosolic membrane surface and is involved in myelin compaction (major dense lines) (Fig 2B). *Mbp* mRNA is assembled into RNA-granules in the cell body and transported along the processes until the myelin membrane synthesis site (Ainger et al. 1993), Local regulation of mRNA translation is increasingly recognized as an important consequence of cell–cell interactions, enabling precise spatial control of cellular responses, such as the process of membrane fusion involved in compaction. Indeed, defects in *Mbp* mRNA transport results in an accumulation of MBP protein in the cell body and myelination defects (Lyons et al. 2009). CNP on the other

hand, interacts with cytoskeleton to maintain the non-compact cytoplasmic channels, necessary for metabolic support, within the sheath. Little is known about the sorting and trafficking of this protein (Snaidero et al. 2017; Stassart et al. 2018).

Developmental myelination is genetically predefined and follows a fixed chronological and topographically sequence of events. Due to the anatomical and complexity differences of the mouse and human brain, it is during the myelination process that we observe the biggest differences between both species. In mice, it takes approximately 3 weeks for OPCs to develop, mature and start myelination. In humans this process can take up to 20 weeks (Czepiel et al. 2015). Since research on mammalian brain development has mostly been carried out in rodents, it is useful to understand how the various myelination stages correlate between mice and human forebrain development. The first early OPCs (PDGFRA+) appear at 8 post conception weeks (pcw) in the human forebrain, which can be compared to E15 (embryonic day) in mice. The first MBP+ pre-mOLGs are detected at 16 pcw in humans, comparable to P3 (postnatal day) in mice. Most strikingly, human developmental forebrain myelination takes decades, compared to weeks in mice (P20) (Jakovcevski et al. 2009) (Fig 1). The inter-species differences are not limited to the developmental myelination, but also to the remyelination response after myelin damage (Franklin et al. 2021). Showcasing the need to take careful consideration when extrapolating results from animal models to the human situation. But ethical concerns and a lack of easy access to human primary cells and tissue make it difficult to study the biology of human oligodendrocytes. Induced pluripotent stem cells (iPSC) are an attractive non-invasive technique to easily acquire human OLG (Chanoumidou et al. 2020; Kuhn et al. 2019).

1.2. Active mRNA transport and local translation

Myelin compaction requires the expression of MBP protein at the cytosolic surface and of PLP1 at the extracellular surface of the membrane bilayer. While PLP1 is transported in vesicles to the assembly site of myelin sheaths, MBP is transported as an mRNA from the cell body before being translated within the sheath (Stadelmann et al. 2019).

Active transport and local translation of transcripts within myelin sheaths is a known regulatory mechanism that allows for the careful control of protein expression in time and space. Localising mRNAs transport and translation is regulated in the context of specific ribonucleoprotein (RNP) complexes. The composition of RNP complexes is determined by a combination of cis-regulatory motifs within the mRNA sequence and of trans-acting proteins. The cis-acting localization elements can be very heterogeneous in size and structure and are often, but not exclusively, located within the mRNA 3′ untranslated regions (UTR) (Doyle and Kiebler 2011; Besse and Ephrussi 2008). A well-defined RNA localization element can be found in the *Mbp and Mobp* mRNAs, containing two partially overlapping 11 nucleotide sequences that are recognized by heterogeneous

nuclear ribonucleoprotein A2 (HNRNPA2) and thus named A2 response element (A2RE) (Munro et al. 1999; Ainger et al. 1993; Schäfer et al. 2016). The binding of *Mbp* mRNA to HNRNPA2 leads to the formation of RNA-granules and the dynamic recruitment of other factors required for the targeted transport, translational repression (HNRNPE1 and sncRNA715) and protein synthesis (arginyl-tRNA synthetase, elongation factor 1a) (Barbarese et al. 1995; Torvund-Jensen et al. 2014). Depending on the cell type and upon arrival at the final subcellular destination, localising mRNAs can either be derepressed by spatially restricted machinery or maintained in a repressed state until a specific signal leads to their activation (Gunkel et al. 1998; Besse and Ephrussi 2008). As *Mbp* mRNA granules reach the oligodendroglial distal process, HNRNPA2 and other granule repressor proteins are phosphorylated by the Fyn kinase. As a result the RNA granule is dissociated and the mRNA released of the transport machinery, allowing localised MBP protein synthesis to occur (White et al. 2008; Müller et al. 2013) (Fig 3). Studies have reported that neuronal activity increases the axonal surface expression of L1 adhesion molecules that mediate oligodendroglia Fyn activation and thus regulate local MBP synthesis and myelination (Wake et al. 2011). An interesting question is whether different mRNAs are co-transported and co-regulated in a single RNA-granule. Some evidence in neurons suggested that microinjected mRNAs containing similar A2RE targeting sequences can be co-assembled into the same granule (Gao et al. 2008), but single-molecule studies appear to argue against mRNA multiplexing (Batish et al. 2012; Mikl et al. 2011).

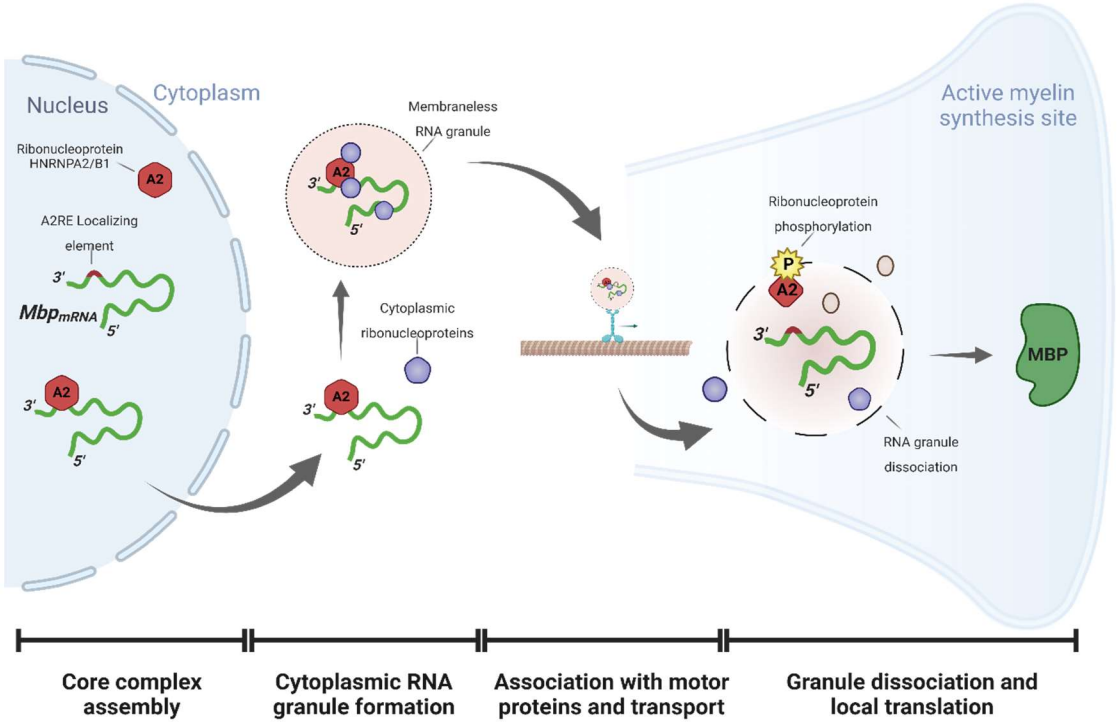

Fig 3 - Active transport and local translation of *Mbp* mRNA within the myelin sheath. In the nucleus, specific heterogeneous nuclear ribonucleoproteins (HNRNPA2B1) bind to the localising element within the 3'UTR region of *Mbp* mRNA (A2RE, red). Further ribonucleoproteins (brown circles) and nuclear export factors (orange, oval) bind to the transcript and form the core mRNA-protein complex. The mRNA–RNP

complex is then exported to the cytoplasm, where additional mRNA-binding proteins associate with the mRNA and repress translation during transport. The mature RNA granules can then associate with motor proteins and be transported to the target site along the microtubule network (brown, tubular figure). Alternatively, the granule can be transported by piggyback in association with other membranous organelles (for example, mitochondria, not shown in the model). Finally, after reaching the target site, the HNRNPA2/B1 is phosphorylated by the Fyn kinase, leading to a change in the protein's conformation and the dissociation of the RNA granule. The transcript is then released and translated into protein. Created with BioRender.com

Investigations into *Mbp* mRNA dynamics have provided significant insights into the interactions of the multiple RNA-binding proteins and associated *cis*-acting mRNA sequences. However, we know very little about the mechanisms that promote localization or translation of the other hundreds of myelin transcripts found in purified myelin fractions (Thakurela et al. 2016).

1.3. Myelin support function

Even though the underlying mechanisms are not well understood, OLGs also have important functions in axonal metabolic support and maintenance of axonal long-term integrity (Saab et al. 2013). OLGs appear to sense the metabolic status of neurons via glutamate sensitive NMDA receptors. These receptors localised at the oligodendroglial membrane, respond to the increased axonal activity leading to the release of lactate that is taken up and utilised by axons to generate mitochondrial ATP (Saab et al. 2016). The NMDA receptors can also induce the release of oligodendrocyte derived exosomes or microvesicles. These exosomes locally transfer specific cargos of metabolites, proteins and RNAs that are internalised and utilised by the neurons. (Frühbeis et al. 2013). One such protein secreted in oligodendrocyte derived exosomes is ferritin heavy chain (FTH1) that protects neurons against iron-mediated cytotoxicity (Mukherjee et al. 2020). Indeed, iron is a redox-active metal that accumulates in the brain with ageing. Dysregulation of iron homeostasis can lead to the production of lethal oxygen reactive species, lipid peroxidation and ultimately cell death. FTH1 is essential to store and detoxify excess intracellular iron. Secretion of FTH1 by oligodendrocytes may be part of a neuronal protective system in the ageing brain (Mukherjee et al. 2020; Ward et al. 2014).

Cytosolic iron levels can regulate the synthesis of FTH1 protein by promoting the repression or translation of pre-existing mRNAs. Under conditions of limited iron supply, the iron responsive element binding proteins 1 and 2 (IRP1 and IRP2) bind to a highly conserved stem loop in the 5'UTR region of the *Fth1* mRNA, the iron regulatory element (IRE), and block mRNA translation. Increased levels of iron reduce the binding affinity of IRP1 and lead to the degradation of IRP2, allowing the translation of *Fth1* mRNA (Ponka 1999; Crichton et al. 2012). The interplay between IRPs and IREs of *Fth1* mRNA have formed the basis of much of our understanding of *Fth1* mRNA–protein interactions and translational regulation, but it is interesting that increases in FTH1 protein levels are

attributed to increased translation and not transcription, as the levels of *Fth1* mRNA remain constant (Burke et al. 2017).

Fth1 mRNA in oligodendrocytes is among the three most highly abundant transcripts (*Mbp*, *Mopb*, and *Fth1*) found in purified myelin when compared to brain lysates and myelinating oligodendrocytes (Thakurela et al. 2016; Gould et al. 2000) (Fig 4A). *Fth1* mRNA levels are increased in myelin fractions of adult mice (P75 vs juvenile P20) (Fig 4B). Conversely, relatively small amounts of FTH1 protein can be found in myelin when compared to brain lysates of adult mice and other typical myelin proteins (CNP) (Mukherjee et al. 2020) (Fig 4C). Interestingly, a longer *Fth1* mRNA isoform, associated with the presence of a 3'UTR, is enriched in myelin (Gould et al. 2000). The cytoplasmic regulation of translation by 3'UTR is of increasing interest because these can not only affect message stability but also message localization and translation. This particular transcript also shows high expression levels in non-neuronal cells of the adult hippocampus when compared to the fetal brain (Percy et al. 1998), suggesting that different *Fth1* RNA isoforms might have different functional roles and as such different regulatory pathways. The presence of high levels of *Fth1* mRNA with a 3'UTR region in the myelin sheath could suggest a mechanism for the active transport of this transcript, followed by its local translation and secretion in exosomes upon neuronal signalling. Targeted transport and local translation of *Fth1* mRNA could effectively provide a way to rapidly respond to external stimuli, as a single mRNA can give rise to multiple copies of a protein, particularly effective for cells with distinct membrane domains separated by large distances.

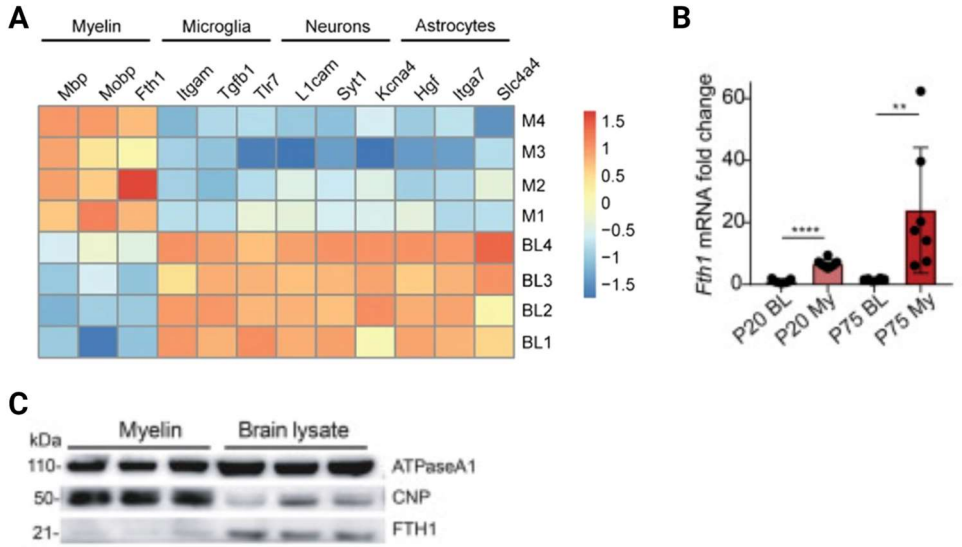

Fig 4 - *Fth1* mRNA is among the three most highly abundant transcripts in myelin, but FTH1 does not behave like a myelin-resident protein. (A) Heatmap displaying reverse CT values from RT-qPCRs performed on myelin biochemically purified from the brains of 4 individual mice (M1–4) compared to the respective brain lysates (BL1–4) at six months of age. Values were colour coded as shown on the left. The expression of three specific transcripts were analysed per cell type: oligodendrocytes or myelin, microglia, neurons and astrocytes. Myelin-related mRNAs *Mbp* and *Mopb*, and of *Fth1* were strongly increased in

myelin fractions when compared to brain lysates. Data source: Thakurela et al. 2016. **(B)** Relative change of *Fth1* mRNA expression in brain lysates (BL) and myelin fractions (My) from P20 (active myelination) and P75 (myelination is complete) wild-type mice. Corroborating A, the data shows that myelin fractions are enriched for *Fth1* transcripts as compared to total brain lysates. Additionally, it shows that *Fth1* mRNA myelin expression is still enriched even after myelination is considered complete. Data are means ± SD; Two-tailed unpaired Student's t test between brain lysate and myelin fractions at the respective age. $**p < 0.01$, $***p \leq 0.0001$. Data source: Mukherjee et al. 2020. **(C)** Immunoblot analyses of brain lysates and myelin fractions obtained from P75 wild-type mice probed for the ubiquitous ATPaseA1, the myelin specific protein CNP and FTH1 protein. Surprisingly, despite previous data suggesting high *Fth1* mRNA expression, relatively small amounts of FTH1 protein are found in myelin fractions compared to brain lysates. Data source: Mukherjee et al. 2020.

Taken together, FTH1 protein does not behave like a myelin-resident protein and further supports a cytoprotective function for FTH1 protein in post-myelinating cells. Moreover, the presence of high levels of *Fth1* mRNA in the myelin sheath could suggest a mechanism for the active transport of this transcript, followed by its local translation and secretion in exosomes upon neuronal signalling.

2. Mouse and human oligodendrocyte models

Our current understanding of OLG development, function and dysfunction is predominantly based on rodent studies. As the transcriptional progression during OLG development is highly conserved between mice and humans, insights from mouse developmental biology have been successfully applied to human oligodendroglial development (Douvaras et al. 2014). On the other hand, recent studies have shown inter-species differences in gene profiles (Jäkel et al. 2019), signalling factors response, myelination temporal progression (Bradl and Lassmann 2010) and remyelination response after myelin damage (Franklin et al. 2021). This could account for the very high ratio (>90%) of therapeutic compounds that fail to reproduce promising effects in experimental autoimmune encephalomyelitis (EAE) mouse models when tested in Multiple Sclerosis patients ('t Hart et al. 2021). Taken together, the development of human oligodendrocyte models would serve as an important experimental platform to better understand human OLG biology and to potential complement and validate findings from animal models.

Ethical concerns and the limited access to human primary cells prevent a detailed understanding of human oligodendrogenesis, with many aspects of human OLG biology and myelination still largely unknown. Recently, a number of protocols have been described to differentiate oligodendrocytes from induced pluripotent stem cells (iPSC) in both two- and three-dimensional culture systems. Oligodendrocytes can be generated by recapitulating *in vitro* the fundamental steps of embryonic development or by ectopic expression of oligodendrocyte specific transcription factors (Kim et al. 2019; Chanoumidou et al. 2020). Continuous improvement of the established protocols will

promote and facilitate the utilisation of the iPSC technology to study human OLG biology and disease.

2.1. Oligodendrocyte mouse models:

Mouse models are important tools in oligodendrocyte research. The development of genome editing tools and imaging techniques have allowed the use of transgenic mice for the characterization of OLG genes and proteins and to study OLG physiology and pathology. The use of knock-out/in mice models and of fluorescent reporters under the regulation of the OLG promoters, can facilitate the characterization of specific OLG cell stages and disease associated states both *in vivo* and *in vitro* (Kuhn et al. 2019).

Several protocols have been developed to isolate and culture mouse oligodendrocytes from all developmental stages. The isolation of OLG from the CNS is based on the expression of typical surface markers, such as PDGFRA or A2B5 for OPCs; O4 or GalC for pre-mOLG and MOG for mOLG (Emery and Dugas 2013). Primary cultures are suitable for studying proliferation, survival and differentiation of OLG, as well as drug screening. Co-culturing systems between mouse oligodendrocytes and neurons (Pang et al. 2012) or nanofibers (Lee et al. 2012) have also been developed to study the myelination process.

Nevertheless, developing mouse models is time-consuming and expensive. Primary cells are also difficult to transfect and do not propagate well, creating the need for constant fresh tissue. Immortalised cell lines derived from primary mouse OPCs, such as Oli-neu, have been developed by forced expression of an oncogene. Oli-neu cells express the typical immature OLG markers and can be differentiated into pre-mOLGs by adding dibutyryl cAMP (Jung et al. 1995). Immortalised cell lines are consistent, robust and low cost, however, due to the unpredictable nature of immortalisation mutations any assumption and translation to any physiological function has to be corroborated by additional models (Kuhn et al. 2019).

2.2. Oligodendrocyte human models:

Human OPCs can be isolated from embryonic tissue, surgery biopsies and post-mortem brains. Ethical concerns, tissue availability and the limited proliferation potential of human OLGs are major limiting factors to work with human cells. Additionally, poor correlation between different studies are hampered by sample heterogeneity inherent to the use of tissues from different donors and ages (Kuhn et al. 2019; Czepiel et al. 2015).

Immortalised oligodendroglial cell lines, such as HOG and MO3.13 can provide a homogeneous and highly proliferative alternative. However, like all immortalised OLG cell lines, they represent an immature OLG unable to differentiate into a mOLG. A recent study showed that HOG and MO3.13 cells represent heterogeneous cell populations with the potential to differentiate towards cell-types other than OLGs. Suggesting that these

cell lines may not represent an appropriate model to study human oligodendrocytes (De Kleijn et al. 2019).

Another potential source of human OLG is through the direct reprogramming of fibroblast. Young, adult, and old-aged fibroblasts can be transdifferentiated into O4+ oligodendrocyte-like cells via the overexpression of oligodendrocyte transcription factors (e.g., SOX10, OLIG2 and NKX6.2). Reprogramming efficiency is low and varies between fibroblast of different tissue origins, suggesting that the source tissue might affect conversion efficiency and limiting the use of this technique on large-scale assays. Further characterization of these induced oligodendrocyte-like cells is necessary to evaluate their capacity to form compact myelin sheaths and the extent to which these cells reflect primary oligodendrocytes (Chanoumidou et al. 2021).

Similar to direct reprogramming, the use of iPSCs to generate oligodendrocytes derived from healthy and diseased donors is a useful approach to potential complement animal models and studying species- and patient-specific features. iPSCs are generated by reprogramming somatic cells via forced expression of specific pluripotency-related transcription factors such as OCT4, SOX2 and NANOG or other molecules that modulate the expression of these proteins (Czepiel et al. 2015). iPSCs could provide a scalable, renewable and easier to edit source of human OLG cells. Differentiation of human OLGs from iPSC can be achieved by recapitulating *in vivo* conditions with specific growth factors (e.g., T3, NT3, IGF, PDGFA) or by inducing the overexpression of specific transcription factors (Kuhn et al. 2019). Unfortunately, differentiation of human iPSCs into cortical myelinating oligodendrocytes is still challenging. Despite the common endpoint, each protocol uses different approaches with different transcription factors, delivery approaches and differentiation methodologies (e.g., embryoid bodies versus monolayer during NPC differentiation), that prevent direct comparisons between studies.

Monocultures of iPCS derived OLG (iOLG) could allow for the genetic and biological manipulation of these cells, without the confounding influence of other brain cell types. However, there are aspects of oligodendrocyte function, especially the myelination process, that are difficult to study in monocultures. Oligocortical organoids and spheroids can facilitate the study of cell-cell interactions and complement *in vivo* studies (Kuhn et al. 2019). OPCs are rarely observed in organoids generated by allowing iPSC cells to differentiate spontaneously, but exposure to specific patterning factors in spheroid models can increase the OLG population. However, organoids and in particular with non-guided cell fate, show limited reproducibility and inconsistent cellular composition. Moreover, cortical spheroids show sparse myelination and lack the appropriate molecular architecture of myelinated axons, suggesting that there are still additional, extrinsic and/or intrinsic cues required for robust OLG formation, differentiation, and survival (Marton et al. 2019; Andrews and Nowakowski 2019; Madhavan et al. 2018).

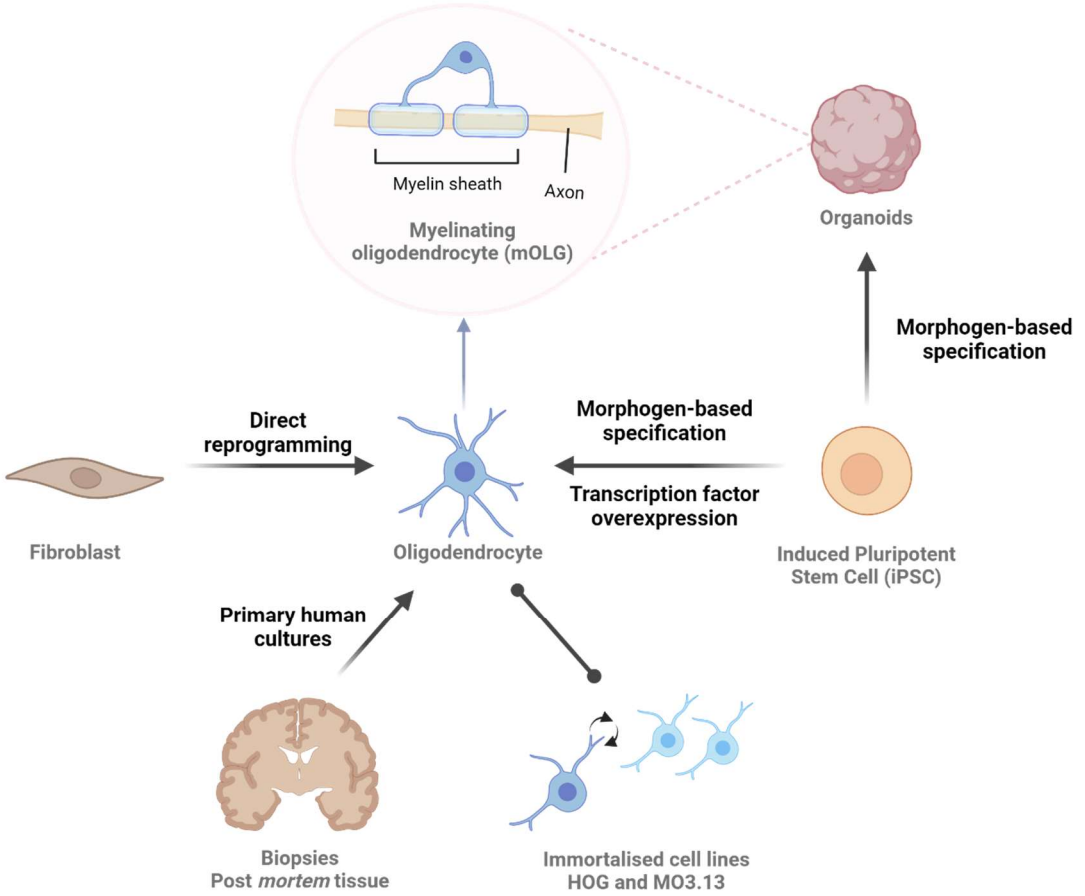

Fig 5 - Human oligodendrocyte models are key to the understanding of oligodendroglial biology in health and disease. Left: Fibroblasts can be directly converted into oligodendrocytes by forced expression of specific transcription factors. However, reprogramming efficiency is low and varies between fibroblasts of different tissue origins. Bottom left: Primary cultures of human oligodendrocytes can be isolated from surgery biopsies, resected tissue or post mortem brains. However, the limited availability of viable human brain tissue is a limiting factor. Bottom right: Oligodendroglial cell lines HOG and MO3.13 can be used as a model of human oligodendrocytes arrested in an immature developmental stage that show very limited differentiation potential. Right: Human induced pluripotent cells (iPSC) are derived from somatic cells and can be differentiated *in vitro* using morphogen-based patterning techniques or by ectopic expression of selected transcription factors, which significantly accelerates differentiation and increases efficiency. Top Right: Human cortical brain organoids contain neurons, astrocytes and oligodendrocytes that co-developed both spatially and temporally. The different cell types are differentiated using morphogen-based patterning techniques. Created with BioRender.com

2.3. iPSC derived oligodendrocyte protocols:

The generation of OLGs from human iPSC in a rapid and efficient manner can facilitate research into oligodendrocyte physiology, disease modelling, drug testing and therapeutic OLG transplantation. The first detailed OLG differentiation protocols from iPSCs attempted to reproduce the temporal signalling sequence along the oligodendroglial lineage. These methods are especially desirable to obtain patient-derived cells and study genetic diseases, however cell yields are variable and require long culture times (44%-70% O4+ cells in 75 days and 34% of MBP+ cells after 95 days) (Wang

et al. 2013; Douvaras et al. 2014). In general, these protocols include the sequential exposure to neural inducing factors, such as SB431542 and LDN193189 (i.e., dual SMAD inhibition) to accelerate the production of PAX6+ neural stem cells; followed by ventralising morphogens that activate the Hedgehog pathway, like purmorphamine or smoothened agonist (SAG) and retinoic acid (RA) to promote OPC differentiation. Subsequent exposure to the mitogens PDGFA and NT3 supports OPC expansion; and insulin growth factor (IGF), hepatocyte growth factor (HGF) and thyroid hormone (T3) potentiate oligodendrocyte maturation (Douvaras et al. 2014; Douvaras and Fossati 2015). iPSC-derived OLGs showed a similar gene expression profile to primary human OLG in single cell RNA sequencing data (Chamling et al. 2021) and when implanted in *shiverer* mice (*MBP-/-*), iOLGs developed in the white matter producing functional myelin structures (Wang et al. 2013; Douvaras et al. 2014).

In an effort to increase efficiency and reduce differentiation time, recent methods have been focusing on ectopic expression of oligodendrocyte specific transcription factors. Overexpression of SOX10 alone can induce expression of the pre-mOLG marker O4, but further differentiation is limited. A combination of OLIG2 and SOX10 substantially increased the oligodendroglial lineage commitment and progression into mature MBP+ mOLGs (Pawlowski et al. 2017; Ehrlich et al. 2017). Moreover, using a lentiviral approach, Ehrlich et al. 2017 defined SOX10, OLIG2 and NKX6.2 (SON) as the most efficient combination with 70% O4+ cells by day 28 and 30% MBP+ cells by day 35. Surprisingly, a year later and also using a lentiviral approach, but with only the SOX10 transcription factor, García-León et al. 2018 showed similar differentiation yields with shorter times, with 60% O4+ cells by day 7 and 20% of MBP+ cells after 18 days. In both studies, iOLGs showed a transcriptional profile similar to primary human oligodendrocytes that were able to myelinate axons in *in vivo shiverer* mouse models. Additionally, avoiding the use of lentiviral vectors by integrating the SOX10 transcription factor in a safe harbour locus significantly increased oligodendrocyte yields up to 89% O4+ cells and 100% MBP+ cells (García-León et al. 2018; García-León et al. 2020).

The conflicting results reflect the different methodological approaches and media compositions used in each study. The lack of standardisation of methodologies makes reproducibility a significant challenge. A comparison of protocols is required to establish the best practices of making iOLGs. Most importantly, it will allow the continuous improvement of the established protocols and facilitate the utilisation and dissemination of the iPSC technology to study human myelin biology and diseases.

3. Hypothesis and aims

Oligodendrocytes are the myelinating cells of the central nervous system, involved in axonal maintenance, survival and circuitry adaptation. Hence, it is not surprising that oligodendrocyte and myelin dysfunctions can lead to serious pathologies. Our current

knowledge about OLGs is predominantly based on rodent studies, but recent evidence have shown inter-species differences in gene profiles, signalling factors response and remyelination response after myelin damage. Thus, we believe that human oligodendrocytes derived from induced pluripotent stem cells are an important experimental platform to better understand human oligodendrocyte biology and potentially complement findings from animal models. However, differentiation of human iPSCs into cortical myelinating oligodendrocytes is still challenging and the results often appear difficult to reproduce. I conducted a comparative study aiming to establish a standardised method for the differentiation of oligodendrocytes from iPSCs via ectopic expression of oligodendroglia transcription factors. In short, we believe that the continuous improvement of established protocols will allow the development of reproducible and cost-effective human oligodendrocyte models to study the mechanisms and pathways of human OLG development, myelination and dysfunction.

In this thesis I also aimed to address the knowledge gap of the mechanism of cytotoxic axonal support by myelinating oligodendrocytes. In previous investigations, we observed that oligodendrocytes secrete ferritin heavy chain protein, which may be internalised by neighbouring neurons. Ferritin heavy chain protein will then act in the neurons as an antioxidant defence system by storing and detoxifying excess intracellular iron. Given the high abundance of *Fth1* mRNA and the relatively small amounts of FTH1 protein in myelin, we hypothesise that the targeted transport and local translation of *Fth1* mRNA in myelin could effectively provide a way for oligodendrocytes to rapidly produce and secrete FTH1 protein in response to external stimuli from neurons. To test our hypothesis, I characterised the expression of *Fth1* mRNA in oligodendrocytes throughout differentiation *in vitro* and *in vivo*. I also investigated the relation between *Fth1* mRNA and other locally translated myelin mRNAs: *Mbp* and *Mobp*. In addition, I established a proteomics approach to further investigate the potential *Fth1* mRNA binding proteins involved in *Fth1* mRNA transport and local translation. We believed that an improved understanding of the aspects governing the dynamics of localising mRNAs in the brain could further elucidate the role of oligodendrocytes in axonal support and unravel potential new cellular and molecular mechanisms underlying myelin-axon communication.

Project 1: A comparative study of iPSC derived oligodendrocyte differentiation via transcription factors ectopic expression

The current chapter includes the research article "A comparative study of iPSC derived oligodendrocyte differentiation via transcription factors ectopic expression". This article reports a comparative study of two methodologies to differentiate oligodendrocytes from iPSCs via ectopic expression of oligodendroglia transcription factors.

Contributions:
Liliana D. Pedro, Carolina Cardoso Gonçalves, Agata Rhomberg, Julien Klimmt, Gernot Kleinberg, Dominik Paquet and Mikael Simons

The author of this thesis is the first author of this manuscript. LDP, DP and MS designed the approach. DP, JK and CCG established the neuronal and astrocyte differentiation protocol. GK and DP developed the microglia differentiation protocol. CCG and JK established 3D co-culture systems. LP and CCG conducted and imaged 3D co-cultures in this manuscript. AR provided technical assistance with RT-qPCRs. LP collected the data, analysed the data and performed statistical analysis and data visualization. LP wrote the manuscript.

A comparative study of iPSC derived oligodendrocyte differentiation via transcription factors ectopic expression

Liliana D. Pedro[1,2,3], Carolina C. Goncalves[3,4], Agata Rhomberg[1,2], Julien Klimmt[3,4], Gernot Kleinberg[6], Dominik Paquet[*2,5] and Mikael Simons[*1,2,5,7]

[1]Institute of Neuronal Cell Biology, Technical University Munich, 80802 Munich, Germany
[2]German Center for Neurodegenerative Diseases (DZNE), 81377 Munich, Germany
[3]Graduate School of Systemic Neuroscience (GSN), 82152 Planegg, Germany
[4]Institute for Stroke and Dementia Research (ISD), 81377 Munich, Germany
[5]Munich Cluster of Systems Neurology (SyNergy), 81377 Munich, Germany
[6]ISAR Bioscience GmbH, 82152 Planegg, Germany
[7]Max Planck Institute of Experimental Medicine (MPI-EM), 37075 Goettingen, Germany
*Correspondence: dominik.paquet@med.uni-muenchen.de (DP), mikael.simons@dzne.de (MS)

Oligodendrocytes (OLGs) are the myelin producing cells of the central nervous system. The development of human oligodendrocyte models would serve as an important experimental platform to better understand human OLG biology and potentially complement findings from animal models. Unfortunately, differentiation of human induced pluripotent stem cells (iPSCs) into OLGs (iOLGs) is still challenging and the lack of reproducible protocols is a major limiting factor to the wide accessibility of iOLGs. Here, we developed a strategy to evaluate the differentiation efficiency of iOLG under the ectopic expression of the transcription factors, SOX10 and SOX10, OLIG2, and NKX6.2 (SON). Our work highlights that the differences in differentiation efficiency found between the transcription factors cannot be reduced to neuronal specification methodology, media composition or donor variability. Overexpression of SOX10 solely generated low yields of O4+ and MBP+ oligodendrocytes. The combination of three transcription factors, SON, greatly improved the differentiation efficiency, up to ±12% of MBP+ iOLGs within 24 days of differentiation. Moreover, by including a purification step we significantly improved oligodendrocyte differentiation yields to ±25% MBP+ iOLGs and reduced the population heterogeneity. Co-culture of SON-iOLGs with iPSC-derived neurons, astrocytes and microglia showed that iOLGs can disperse within the culture and form myelin-like structures *in vitro*. This study establishes a standardised method to generate iOLGs, which will allow the development of reproducible and cost-effective human iPSC-derived oligodendrocyte models.

Introduction

In mammalian central nervous systems (CNS) oligodendrocytes (OLG) form myelin, a multi-layered lipid-rich membrane around axonal membranes. Myelin promotes fast saltatory nerve conduction by electrically insulating axons and establishing axonal domains (Stassart et al. 2018; Stadelmann et al. 2019), it also has important functions on axonal metabolic support (Saab et al. 2013; Nave 2010) and information processing (Moore et al. 2020).

In order for myelination to occur, oligodendrocytes follow an intrinsic program of proliferation, migration and differentiation. Oligodendrocyte precursor cells (OPCs) arise from the cortical subventricular zone (Huang et

al. 2020). These highly proliferative cells migrate and populate the CNS, finally differentiating into post-mitotic pre-myelinating oligodendrocytes (pre-mOLGs). Pre-mOLGs have a highly branched morphology and will extend their processes to sense surrounding axons. Upon finding permissive axons, pre-mOLGs will further mature into myelinating oligodendrocytes (mOLGs) and myelinate nearby axons (Mitew et al. 2014; Emery 2010).

Since our knowledge on human oligodendrocytes is limited, results from rodents are often extrapolated to human cells. The spatial and transcriptional progression of oligodendrocyte development in rodents is very similar to that of humans, with timing the major difference between the two species. It takes 3 weeks for mouse OPCs to differentiate and start myelinating, while in humans this process can take up to 22 weeks (i.e., 16 post conception weeks) (Czepiel et al. 2015; van Tilborg et al. 2018). Myelination is resolved in rodents by postnatal day 60, while in humans myelination extends over 22 years of age (Bradl and Lassmann 2010; Jakovcevski et al. 2009). Other reported differences between species include OPC transcriptome discrepancies, signalling molecule responses (Bradl and Lassmann 2010) and the remyelination response after myelin damage (Franklin et al. 2021).

Human OPCs have been successfully isolated from fetal and post-mortem adult brain tissue, but ethical concerns and poor access make it difficult to study these cells. Induced pluripotent stem cells (iPSC) are an attractive non-invasive technique to acquire human OLG (Chanoumidou et al. 2020; Kuhn et al. 2019). The first protocols differentiated oligodendrocytes from human iPSC (iOLG) by exposing the cells to specific growth factors that recapitulate the *in vivo* signalling cascades of embryonic development. This method is especially desirable to obtain patient-derived cells and study genetic conditions. However, cell yields are variable and require long culture times (44%-70% O4+ cells in 75 days and 34% of MBP+ cells after 95 days) (Wang et al. 2013; Douvaras et al. 2014).

In an effort to increase efficiency and reduce differentiation time, recent methods have focused on the ectopic expression of oligodendrocyte specific transcription factors. Initial publications showed that overexpression of SOX10 solely can induce expression of the pre-mOLGs marker O4, but the cells failed to mature (Pawlowski et al. 2017; Ehrlich et al. 2017). Using a lentiviral approach, Ehrlich et al. 2017 defined SOX10, OLIG2 and NKX6.2 (SON) as the most efficient combination, with 70% O4+ cells by day 28 and 30% MBP+ cells by day 35. Surprisingly, a year later and also using a lentiviral approach, but with only the SOX10 transcription factor, García-León et al. 2018 showed similar differentiation yields with shorter times, with 60% O4+ cells by day 7 and 20% of MBP+ cells after 18 days. In both studies, iOLGs showed a transcriptional profile similar to primary human oligodendrocytes that were able to myelinate axons in *in vivo* mouse models. By avoiding the use of lentiviral vectors, and their inherent risk of insertional mutagenesis, the SOX10 transcription factor can be stably integrated into the safe harbour locus, thereby significantly increasing oligodendrocyte yields up to 89% O4+ cells and 100% MBP+ cells (García-León et al. 2018; García-León et al. 2020).

The conflicting results might reflect the different methodological approaches and media compositions. To differentiate iPSCs into NPCs Ehrlich et al. 2017 used dual SMAD inhibition and embryoid bodies, while García-León et al. 2018 generated NPCs by dual SMAD inhibition in adherent culture conditions. Previous research showed that neural induction under fully adherent conditions results in a more uniform and consistent yield of NPCs than embryoid bodies (Chambers et al. 2009). The lack of standardisation of methodologies makes reproducibility a significant challenge.

Here, we describe a streamlined iOLG differentiation strategy optimised for high yields and purity that uses transgene-based

expression of transcription factors. It also facilitates the comparison between the iOLGs differentiation capacity under the ectopic expression of different transcription factors. We showed that overexpression of SOX10 in combination with OLIG2 and NKX6.2 outperforms the ectopic expression of SOX10 alone. This approach yields up to ±12% MBP+ iOLGs within 24 days of differentiation, compared to ±5% of MBP+ iOLGs when using only SOX10. Furthermore, adding an O4 antigen purification step to our protocol significantly increased the efficiency and sample homogeneity to ±25% of MBP+ SON-iOLG within 12 days after sorting. The gene expression profile of the SON-iOLG cell line confirmed the expression of OPC markers OLIG2 and NKX2.2 and the differentiation markers MBP, PLP and MOG. Finally, co-culture with iPSC-derived neurons and astrocytes in a 3-dimnesional tissue model showed that SON-iOLGs can form myelin-like structures *in vitro*.

Results

Generation of stable iPSCs for the inducible expression of oligodendrocyte specific transcription factors. The development of human oligodendrocyte from iPSCs is becoming an important experimental model to complement findings from animal models. Currently available protocols show conflicting results that reflect different methodological approaches and do not allow for direct comparisons; thus, limiting the availability of this cell model to many groups. Therefore, we aimed to investigate and establish a standardised method for the differentiation of oligodendrocyte from human iPSCs through the ectopic expression of oligodendrocyte specific transcription factors. Among all the transcription factors tested in the different publications, SOX10 (García-León et al. 2018) and the combination SOX10, OLIG2 and NKX6.2 (SON) (Ehrlich et al. 2017), were described as the most efficient to accelerate oligodendroglial specification. Moreover, integration of the transcription factor in a safe harbour locus significantly increased oligodendrocyte yields and reproducibility (García-León et al. 2020).

To allow for direct comparison, avoid off-target effects and reduce the clonal variation associated with all genome editing technologies (Lee et al. 2019), we generated an iPSC master cell line (MCL) with a flippase (FLP) recombinase-mediated cassette exchange (RMCE) in the natural integration site of the Adeno Associated Virus type 2 (*AAVS1*) locus to generate all the transgenic iOLG cell lines (Fig 1A) (Ordovás et al. 2015). The master cell line contained an FRT-flanked cassette with a GFP and a hygromycin-resistance/thymidine kinase selection cassette (HYG-TK) linked by a P2A self-cleavage site. One heterozygous targeted clone (A18-P1C11) was chosen for further characterisation (Fig Sup1A) and incorporation of the oligodendrocyte specific transcription factors. The coding sequences for each transcription factor combination were cloned into the same tetracycline (tetO)-inducible vector, as well as a fluorescent protein (SOX10-GFP; SON-RFP) and a puromycin selection cassette, flanked by FRT sites (Fig 1A). The RMCE SOX10-GFP and SON-RFP cell lines were selected through a combination of positive and negative selection and further characterised (Fig Sup 1 and 2). The activity of the inducible promoter was tested by adding Doxycycline (Dox) and the dual SMAD inhibitors to the cell lines for 72h. Both cell lines showed high expression of the respective fluorescent proteins, exclusively under the presence of Dox (SOX10-GFP: 97.1% ± 2.3%; SON-RFP: 91.7% ± 4.4%) (Fig 1C). The cell lines also show some transgene expression mosaicism, as observed by the variable intensity of the transcription factors expression, SOX10 and OLIG2. Within the SON-RFP cell line a few RFP-negative cells (<9%) can be observed after Dox treatment. The presence of RFP-/OLIG2-/SOX10- cells (Fig 1C, red asterisk) suggest some level of transgene silencing (Ordovás et al. 2015), while RFP-/OLIG2+ cells (Fig 1C, white asterisk) point to a downregulation of the RFP cassette due to its downstream location in relation to the IRES

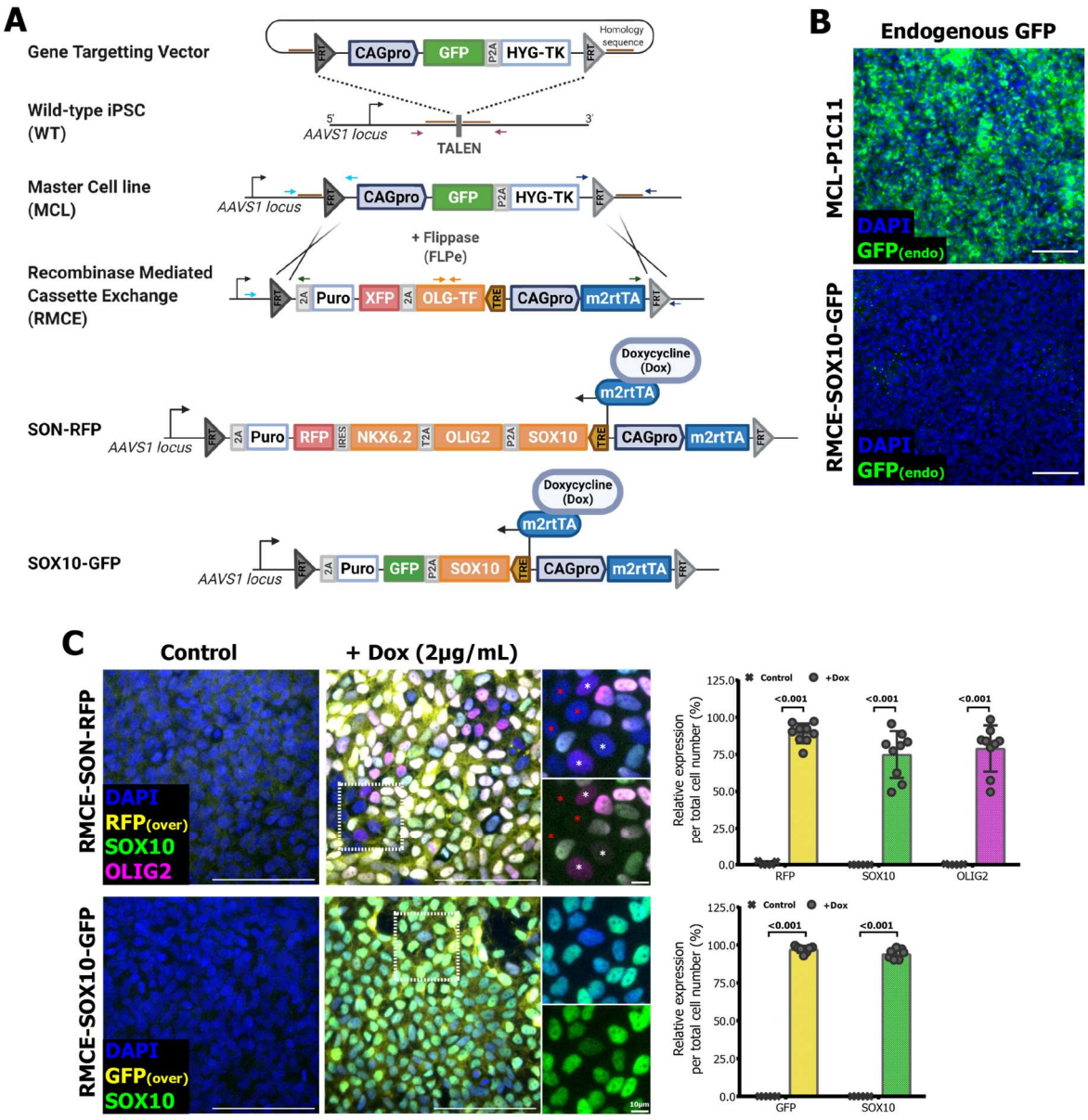

Fig 1 - RMCE strategies can facilitate the systematic comparison of phenotypes between iOLG cell lines. (A) Schematic of safe harbour strategy used to generate the cell lines. The original wild type locus and master cell line gene targeting vector flanked by heterotypic FRT sequences are depicted with the homology regions (thick brown bars) to the *AAVS1* locus. Donor vectors with the transcription factors sequences of interest (SON-RFP and SOX10-GFP) were transfected with FLPe recombinase into the MCL and double selected for puromycin (Puro) resistance and lack of thymidine kinase (TK) sensitivity. The surviving cells are the result of successful recombinase-mediated cassette exchange (RMCE) that retain a tetracycline responsive element (TRE) activated by the presence of Dox. Pink, turquoise, dark blue and orange arrows represent the location of the genotype primers used to determine the insert and correct insertion of the different cell lines. **(B)** Top: representative immunocytochemistry images of GFP endogenous expression in undifferentiated MCL cells; bottom: after recombinase-mediated cassette exchange the GFP-HYG-TK cassette of the MCL is exchange by the Dox induced transcription factors and the endogenous GFP is no longer expressed in undifferentiated and non-induced RMCEs. **(C)** Representative immunostaining and quantification of the fluorescent markers and transcription factors expression after treatment with 2 µg/mL of Dox for 72h. Top: Dox treatment of the SON-RFP cell line induced the significant expression of RFP (yellow), SOX10 (green) and OLIG2 (pink). Bottom: in the SOX10-GFP cell line Dox induced the significant expression of GFP (yellow) and SOX10 (green). No fluorescent

markers or transcription factor staining are found in non-induced controls. Variations in the transcription factor staining intensity reflects the cell lines' transgene expression mosaicism. Additionally, the SON-RFP cell line shows some level of transgene silencing found in RFP-/OLIG2-/SOX10- cells (red asterisk) and the downregulation of the RFP cassette in RFP-/OLIG2+ cells (white asterisk). Data are represented as mean ± SD of 5 to 9 technical replicates. Multiple t-test statistical analysis between control and Dox treatment for each marker and corrected for multiple comparisons with Holm-Sidak method. Scale bar 100 µm.

element (Fig 1A) (Chan et al. 2011).

SOX10, OLIG2 and NKX6.2 overexpressing cells differentiate into mature MBP-expressing oligodendrocytes more efficiently than SOX10 alone. To generate iOLGs from the SOX10-GFP and SON-RFP iPSC lines, we followed a similar approach to García-León et al. 2018. In this protocol NPCs are efficiently derived from iPSCs when exposed to dual SMAD inhibitors together with retinoic acid (RA) (day 0-8). By adding smoothened agonist (SAG) (day 8-12) we activate the hedgehog signalling pathway and promote the differentiation of NPCs to glial progenitors. Subsequent exposure to Dox induces the overexpression of the specific transcription factors and accelerates oligodendroglial specification. Mitogens such as platelet-derived growth factor receptor alpha (PDGFA), hepatocyte growth factor (HGF), and neurotrophin 3 (NT3) support OPC expansion; and insulin growth factor (IGF), 3',5'-cyclic AMP (cAMP), biotin (Bio) and thyroid hormone (T3) potentiate oligodendrocyte maturation (day 12-32) (Fig 2A). Treatment time frames, cell seeding densities and Dox concentration were empirically determined based on the expression of the appropriate oligodendrocyte stage markers as detected by immunostainings (Fig Sup 3). Both cell lines differentiate at similar rates, and show similar expression levels of the pluripotency stem cell marker OCT4, the neuronal stem cell marker PAX6 as well as OPC markers NKX2.2 and OLIG2. As expected OCT4 expression levels are quickly downregulated once differentiation starts (Sup Fig 4B). At the end of neuroectoderm patterning at day 8, more than 60% of cells expressed PAX6 (SOX10-GFP: 64.8% ± 0.7%; SON-RFP: 71.3% ± 3.9%) and we can observe the emergence of the first cells of glial lineage, as evidenced by immunostaining of the two OPC markers OLIG2 and NKX2.2 (Fig. 2B and C). Subsequent treatment with the ventral patterning factor SAG resulted in a substantial increase of at least 13-fold in the expression of OPC factors NKX2.2 and OLIG2, at day 12. OLIG2 expression is a useful early marker of successful specification of NPCs toward OPC generating domains (Stacpoole et al. 2013), respectively (Fig. 2B and C). The protocol, at this first differentiation stage, is highly reproducible among the different cell lines and trials. The starting cell density was found to be the biggest contributor to the variance in the OLIG2 and NK2.2 cell percentage at day 12.

Next, we assessed the terminal differentiation potential of iOLGs *in vitro* after transcription factor induction via Dox. The expression of the SOX10 or SON transcription factors is concurrent with the respective fluorescent markers, GFP and RFP. After 12 days of Dox treatment approximately 38% of the cells expressed a fluorescent marker (SOX10-GFP: 39.0% ± 3.2%; SON-RFP: 37.6% ± 12.1%) (Fig 2D). Despite increasing Dox concentrations, the percentage of GFP+ and RFP+ cells never reached 100% (Fig Sup 3A and B), suggesting some level of transgene silencing and/or expression mosaicism, supporting previous observations (Fig 1C), or a lack of potential of some cells to differentiate into that direction (due to other reasons than the transgene). Immunofluorescent staining confirmed the expression of the O4 markers and MBP protein by day 24, further showing complex cell morphologies ranging from highly branched to myelin-like sheaths (Fig 2E).

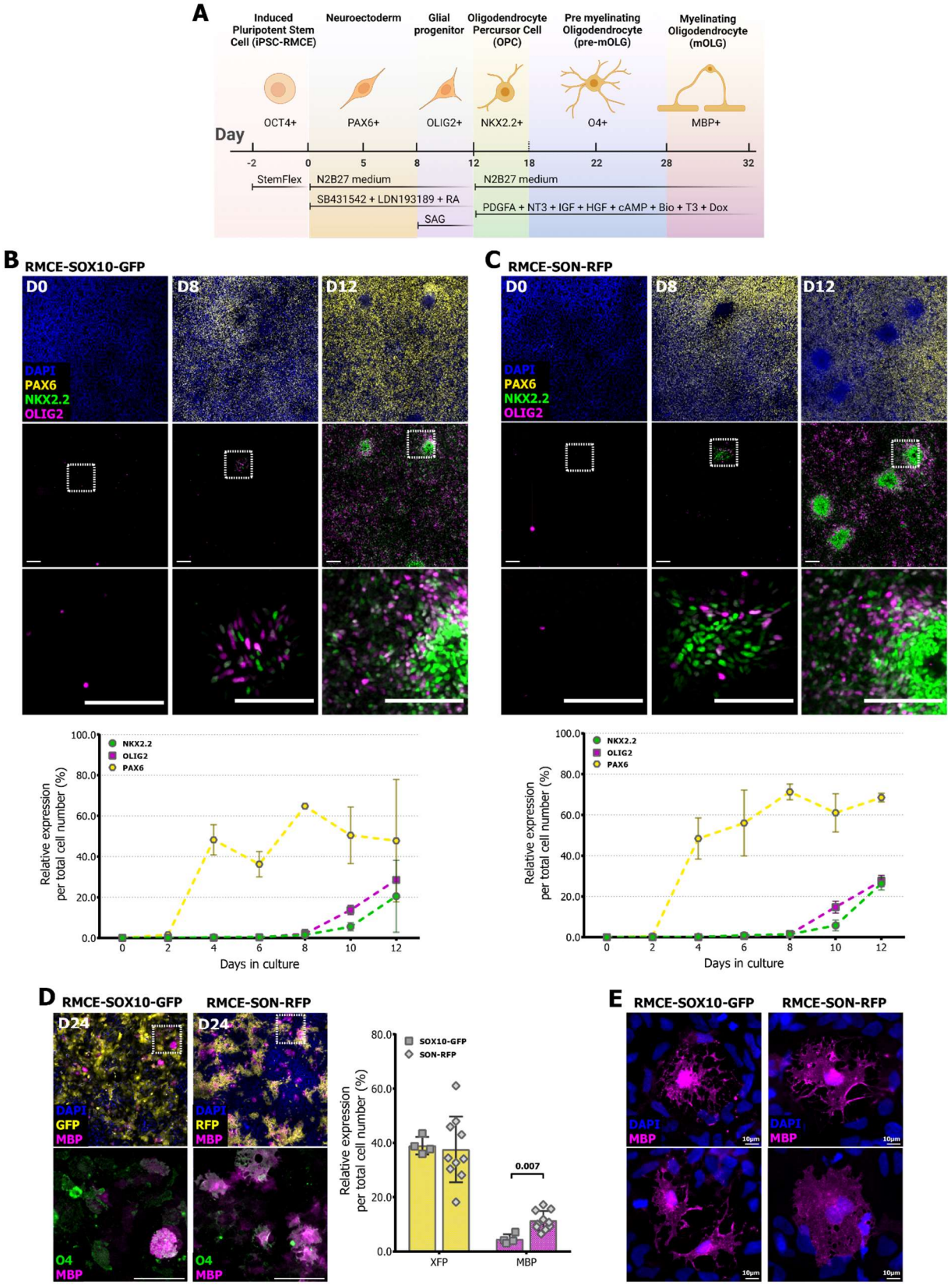

Fig 2 - iPSCs overexpressing SOX10-GFP and SON-RFP can differentiate into mature oligodendrocytes. (A) Diagram of the differentiation protocol timeline showing representations of the different cell stages, the respective stage markers, and media compositions. RA: all-trans retinoic acid; SAG:

smoothened agonist; PDGFA: platelet-derived growth factor; NT3: neurotrophin 3; IGF-I: insulin-like growth factor-1; HGF: hepatocyte growth factor; cAMP: N6,2′-O-Dibutyryladenosine 3′,5′-cyclic monophosphate sodium salt; Bio: Biotin; T3: thriiodothytonine. **(B and C)** Representative immunostaining and quantification of the sequential expression of neuronal progenitors (PAX6+, yellow) and OPCs (OLIG2+, pink and NKX2.2+, green) through the first 12 days of differentiation. Data are represented as mean ± SD of 2 independent experiments. Scale bar 100 μm. **(D)** Representative immunostaining and quantification of the mature oligodendrocytes. At day 24 approximately 40% of the cells are sensitive to Dox induction as shown by the expression of the fluorescent markers GFP and RFP (XFP, yellow). The SON-RFP cell line expresses significantly more mature MBP+ oligodendrocytes (pink). The SOX10-GFP cell line appears to express more O4+ (green) but MBP- pre-mOLGs suggesting that it might differentiate at a slower pace. Data are represented as mean ± SD of 4 to 10 independent experiments for the SOX10-GFP and SON-RFP cell line, respectively. Multiple t-test statistical analysis between cell lines for each marker and corrected for multiple comparisons with Holm-Sidak method. Scale bar 100 μm. **(E)** Representative immunostaining at high magnification of mature MBP+ oligodendrocytes from the SOX10-GFP (left) and SON-RFP (right) cell lines at day 24. SOX10-GFP cells show highly branched morphologies associated with late pre-mOLGs. SON-RFP cells show bigger myelin-like sheaths, characteristic of terminally differentiated and mature mOLGs. Scale bar 10 μm.

Semi-automated quantification of these markers showed that 11.8 ± 3.6% of the total SON-RFP cells expressed MBP, compared to only 4.5 ± 1.8% MBP+ cells of the total SOX10-GFP population (Fig 2D). Interestingly, the SOX10-GFP cell line showed more O4+/MBP- cells when compared to the SON-RFP cell line (Fig 2D; green cells) suggesting that the SOX10-GFP line might differentiate at a slower pace.

Introducing an antigen purification step can improve differentiation efficiency and reduced sample heterogeneity. To increase oligodendrocyte differentiation efficiency, reduce population heterogeneity and eliminate contaminant cells, we established a iOLGs magnetic-activated cell sorting (MACS) step using antibodies against endogenous A2B5 and O4 surface antigens (Fig 3A and B). The A2B5 antibody binds to surface gangliosides and A2B5+ OPCs were previously characterised as highly proliferative early-stage OPCs with bipolar or tripolar morphology. Though the A2B5 antigen may be expressed in other glial cells and developing neurons, A2B5+ cells could potentially provide a cell population of proliferative oligopotent progenitor cells capable of sustained long-term culture and expansion (Scolding et al. 1999). O4 binds to sulfatide and galactocerebroside molecules. O4+ OLGs show a multipolar morphology found on late-stage OPCs and post-mitotic immature pre-mOLGs. Therefore, O4 is a more reliable marker for OPCs committed to the oligodendroglial fate (Yang et al. 2011).

Using MACS purification 6 to 8 days after Dox induction, we purified A2B5+ SOX10-GFP and SON-RFP iOLGs and further cultured these cells for 12 days (Fig 3A), during which the number of cells increased more than 8-fold and 18-fold, respectively. Immunocytochemical analysis with mature OLG markers showed that only 1.5% ± 0.2% of SOX10-GFP and 13.1% ± 0.5% of SON-RFP derived cells were MBP+ (Fig 3C). The A2B5-sorted cells show a branched morphology, with multiple fine cell processes resembling early pre-mOLGs. Moreover, more than 60% of the cell population for both lines was negative for the respective fluorescent marker, suggesting the presence of low Dox induction competency and/or contaminant cells within the A2B5+ sorted cells. As a control, we plated at the same cell density both the A2B5- and the A2B5+ fractions for the SON-RFP cell line (Fig Sup4A). In line with the previous observation the SON-RFP cell line showed significantly more RFP+ cells in the A2B5-negative fraction when compared to the positively sorted cells (A2B5-: 46.9% ± 13.0%; A2B5+: 28.7% ± 4.3%).

Interestingly, even though we obtained a significantly lower percentage of MBP+ cells (4.6% ± 3.9%) in A2B5- cells, they showed a more mature morphology with myelin-like sheaths and O4+ staining. Overall, the data suggests that A2B5 purification did not significantly improve oligodendrocyte differentiation yields, as measured by percentage of MBP+ cells, or efficiently reduce the population heterogeneity, as determined by RFP+ cells, when compared to the non-sorted protocol at the same differentiation stage (see D30 non sorted in Fig 2D vs Ab-D12 sorted in Fig 3C).

Purification of post-mitotic oligodendrocytes using anti-O4 magnetic microbeads at 6 to 8 days after Dox induction was only possible in the SON-RFP cell line, due to a lack of O4 expression in the SOX10-GFP cell line, once again suggesting that the SON-RFP and SOX10-GFP cell populations do not differentiate at the same rate. Following trials to purify O4+ cells from the SOX10-GFP cell line at later time points provided inconsistent results with very low yields (data not shown). O4 Sorting yields for the SON-RFP oligodendrocytes (O4 beads+ cell number/input total cell number) ranged from 8% to 15%. As expected O4+ cells showed less proliferative aptitude with only an approximate 5-fold increase in the total cell number after 13 days in culture. In O4+ cultures, mature MBP+ iOLGs account for 24.7% ± 11.6% of the total cell number, with approximately 71.0% ± 6.23% RFP+ cells, a statistically significant increase in the yield and homogeneity of the culture when compared to the O4- fraction (Fig 3D) and the non-sorted protocol (see D30 non sorted in Fig 2D vs Ab-D13 sorted in Fig 3D; MBP p-value: 0.004; RFP p-value: <0.001). Moreover, a large fraction of the MBP-negative cells in the positively sorted fraction also show O4 expression, indicating that they have the ability to further differentiate into mature oligodendrocytes. Together, the data demonstrate the capability of improving oligodendrocyte differentiation efficiency using a cell sorting approach based on cell surface O4 antigen for late-stage OPCs and immature oligodendrocytes.

SON-iOLGs express maturation markers and exhibit myelin-like sheaths in co-culture systems. In all tested conditions the SON-RFP cell line outperformed the SOX10-GFP cell line, showing a significantly higher expression of mature MBP+ oligodendrocytes. As such, we aimed to further characterise this cell line by analysing its gene expression dynamics and *in vitro* differentiation capacity.

To assess the kinetics of SON-RFP oligodendroglial specification, we conducted a RT-qPCR analysis to compare the expression levels of different oligodendrocyte markers throughout the differentiation protocol, with and without O4 antigen sorting. GAPDH was previously shown to have a constant expression level during oligodendrocyte differentiation and was used as a reference gene (Marton et al. 2019). The resulting threshold cycle (Ct) values were normalised to day 2 for the standard differentiation protocol or day 18 when analysing sorted cells. As expected, we observed a downregulation of the pluripotency markers OCT4 and NANOG (Fig Sup4C), and the upregulation of the NPC marker PAX6 (Fig 4A) after initiating the treatment with the dual SMAD inhibitors and retinoic acid combination, reflecting the loss of the undifferentiated nature of the human iPSCs and its further differentiation into the neuroectoderm lineage Further specification of these cells into the oligodendroglial lineage can be observed after day 8 with the increasing expression of the transcription factors, OLIG2 and NKX2.2 (Fig 4A). This data is further supported by previous immunostaining results, showing increasing levels of OLIG2 protein after day 8 (Fig 2C). Indeed, the OLIG2 expression in human tissue is found in early precursor cells originating from the subventricular zone and ganglionic eminences (Fig Sup4D), after which these cells undergo extensive proliferation and migrate into the

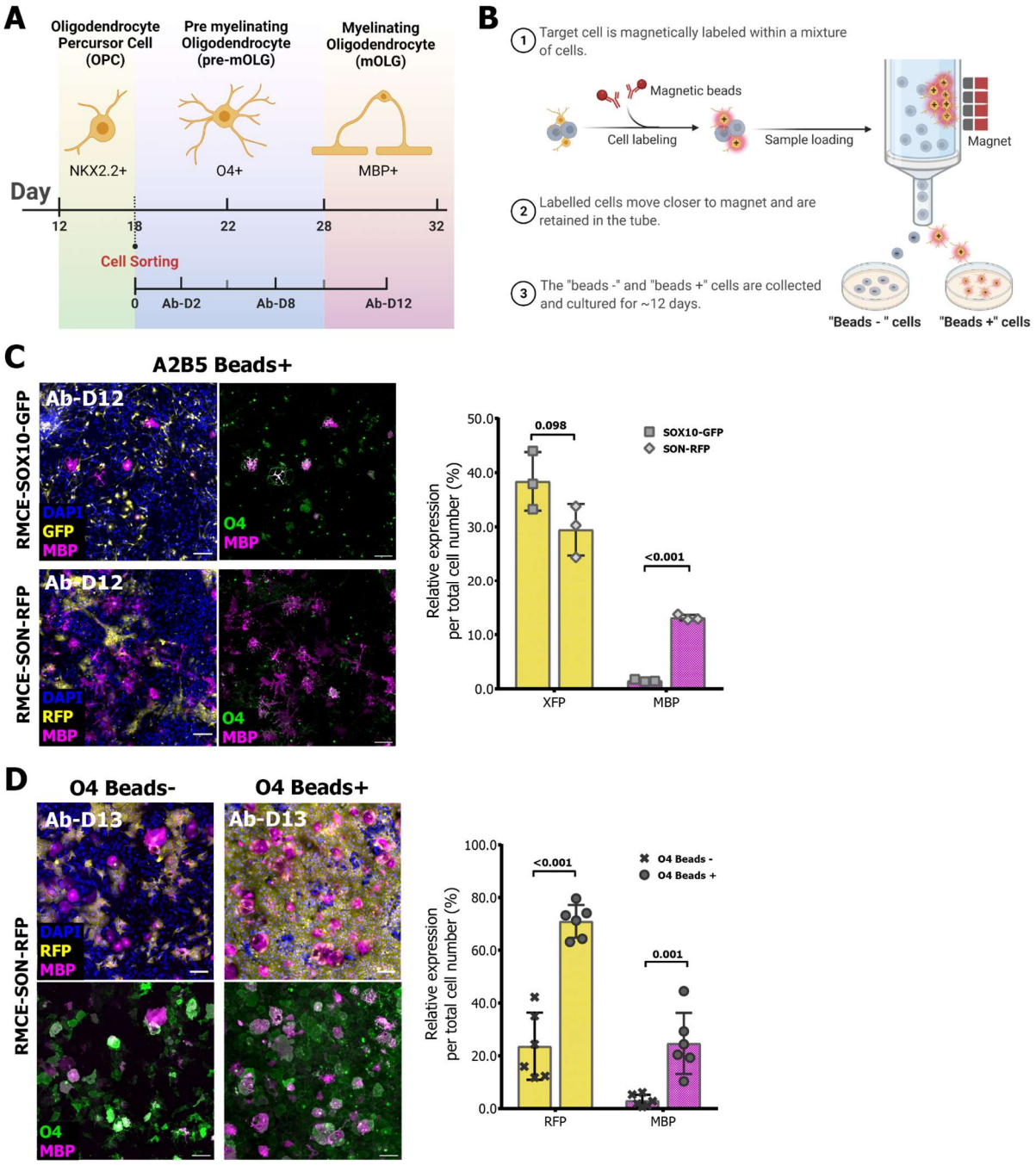

Fig 3 - Cells sorted with the A2B5 antigen further differentiated into highly ramified pre-mOLGs, while cells sorted with the O4 antigen differentiated into mature iOLGs. (A) Diagram of the purification protocol timeline showing the equivalent time points in the standard non-sorted protocol (Ab-D0 = D18). The different cell stages and respective markers are depicted. **(B)** Magnetic-activated cell sorting (MACS) strategy, where magnetically labelled antibodies bind to the cell surface antigens. The magnetically labelled cells (beads+, red) are retained within the column, while unlabelled cells (beads-, grey) flow through. By removing the magnet, target cells are eluted and cultured for approximately 10 days. **(C)** Representative immunostaining and quantification of A2B5+ cells cultured for an additional 12 days after sorting. Approximately 40% of the A2B5+ SOX10-GFP cells express the fluorescent marker GFP (XFP, yellow square), but only ±2% are MBP+ (pink square). Bottom: A2B5+ SON-RFP cells express significantly more mature MBP+ iOLGs (pink, diamond). These cells show a highly ramified morphology associated with pre-mOLGs. Data are represented as mean ± SD of 3 independent experiments. Multiple t-test statistical analysis between cell lines for each marker and corrected for multiple comparisons with Holm-Sidak

method. Scale bar 100 µm. **(D)** Representative immunostaining and quantification of the O4- (left) and O4+ (right) SON-RFP cells obtained after sorting. O4 sorting increased sample homogeneity as shown by the high levels of RFP+ cells (RFP, yellow) in the beads + fraction (circle) compared to the beads - fraction (cross). O4+ SON-RFP cells express significantly more MBP (pink) and virtually every cell expresses the O4 marker (green), suggesting the capability of these cells to terminally differentiate into mOLGs. Data are represented as mean ± SD of 6 independent experiments. Multiple t-test statistical analysis between cell lines for each marker and corrected for multiple comparisons with Holm-Sidak method. Scale bar 100 µm.

cortex (Naruse et al. 2017). However, the expression of the proliferative marker MKI67 did not markedly vary over the entire differentiation period, but there is a trend for a downregulation as the cells differentiate into mature and post-mitotic iOLGs (D26) (Fig 4A).

The gene expression heatmap clearly shows that many myelin associated genes had their highest expression levels after the Dox induction. The Dox effect in the ectopic expression of the transcription factors cassette can be observed by the significantly high expression of the SOX10 marker after D12 (Fig 4A). The upregulation of myelin genes, MBP, PLP1, myelin-associated glycoprotein (MAG) and myelin oligodendrocyte protein (MOG), after the overexpression of the SON transcription factors is a direct result of the oligodendroglial network positive feedback loops, in which OLIG2 or SOX10 induce other factors, such as MYRF, that will positively regulate myelin target genes and promote the OLG differentiation and myelination (Emery et al. 2009). The concurrence of high expression levels of the neuronal precursor marker PAX6, the OPC marker NKX2.2 and the myelin markers MBP and PLP1, after Dox induction clearly reflects the sample heterogeneity. Moreover, the expression of the synaptic marker synaptophysin (SYP) and the astrocytic marker glial fibrillary acidic protein (GFAP) may suggest the presence of non-OLG contaminant cells (Fig 4A).

Population heterogeneity is markedly reduced after O4 antigen sorting of the iOLG, as shown by the reduced expression of MKI67, PAX6, NKX2.2 and SYP and the upregulation of myelin genes in O4+ fraction (Fig 4B). Unexpectedly, the GFAP expression levels increased after purification. It is known that GFAP-expressing progenitor cells can produce neurons and oligodendrocytes, and previous studies showed that mouse glial cells expressing O4 are able to differentiate into astrocytes or oligodendrocytes in serum conditions (Trotter and Schachner 1989). Together the gene expression profile shows that overexpression of SON transcription factors, after treatment with a combination of dual SMAD inhibitors, RA and SAG promotes the establishment of an oligodendroglial identity and terminal differentiation into myelinating iOLGs.

To evaluate the differentiation capacity of iOLGs *in vitro*, we purified O4+ SON-iOLGs at day 18 and further cultured them with neurons and astrocytes in both 2D and 3D co-culture systems. Immunocytochemistry analysis of mature MBP+ iOLGs revealed the extensions of some cell processes along neuronal fibres in 2D co-cultures. Unfortunately, and similar to other research groups (Wang et al. 2013), while some myelin-like structures can be seen aligned with neuronal segments, these events are rare. It is possible that human oligodendrocytes require long-term cultures to myelinate, similar to the long myelination period observed in human cortical development (Fig Sup4D). However, monolayer co-culture systems cannot be maintained for long-term, as the cells will begin to detach from the coverslips. 3D co-culture systems offer some advantages, such as the ability to be maintained long-term, a microenvironment that can better mimic the appropriate cellular environment and

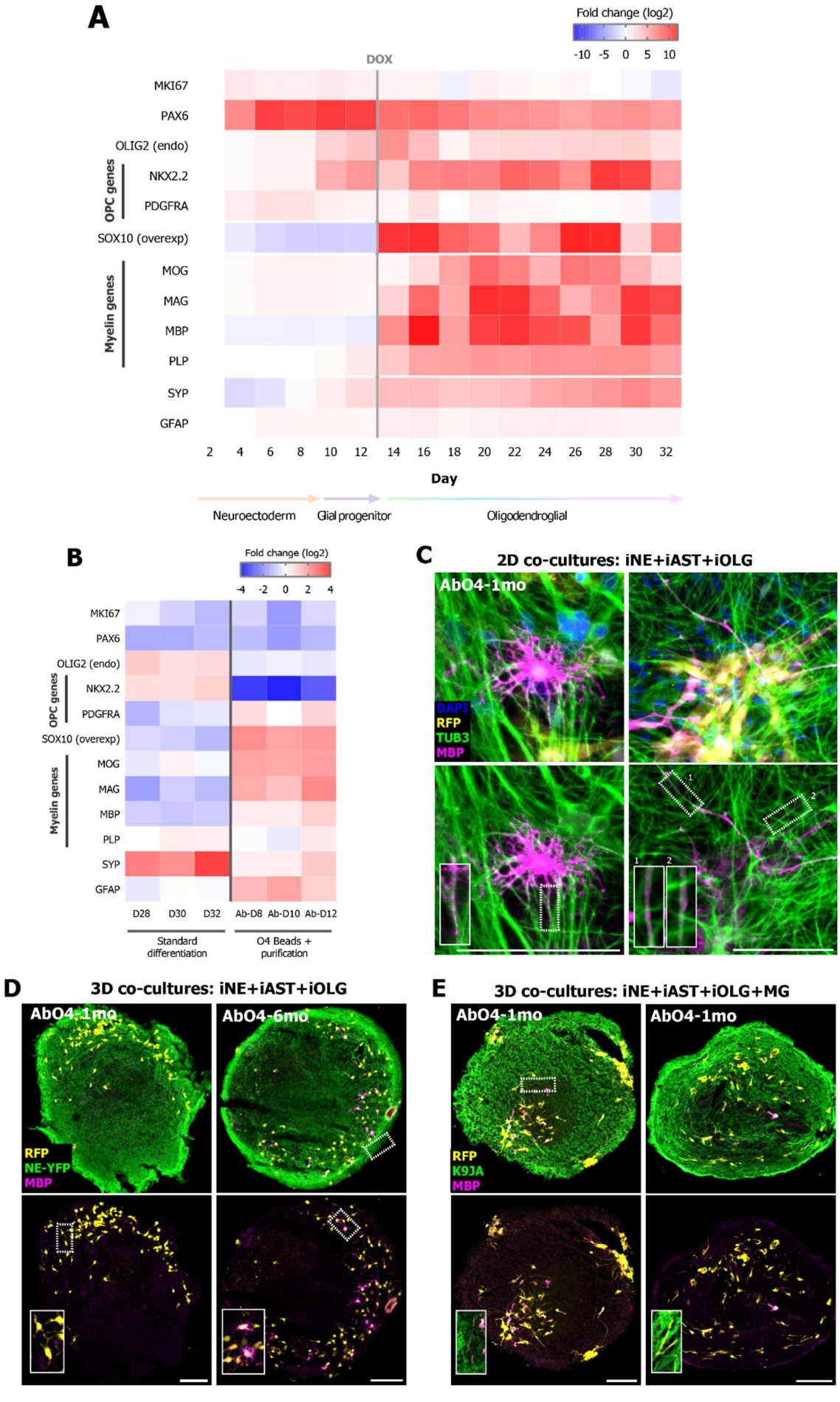
A
Fold change (log2)
-10 -5 0 5 10
DOX
MKI67
PAX6
OLIG2 (endo)
OPC genes
NKX2.2
PDGFRA
SOX10 (overexp)
Myelin genes
MOG
MAG
MBP
PLP
SYP
GFAP
2 4 6 8 10 12 14 16 18 20 22 24 26 28 30 32
Day
Neuroectoderm
Glial progenitor
Oligodendroglial
B
Fold change (log2)
-4 -2 0 2 4
MKI67
PAX6
OLIG2 (endo)
OPC genes
NKX2.2
PDGFRA
SOX10 (overexp)
Myelin genes
MOG
MAG
MBP
PLP
SYP
GFAP
D28 D30 D32 Ab-D8 Ab-D10 Ab-D12
Standard differentiation
O4 Beads + purification
C
2D co-cultures: iNE+iAST+iOLG
AbO4-1mo
DAPI
RFP
TUB3
MBP
D
3D co-cultures: iNE+iAST+iOLG
AbO4-1mo
AbO4-6mo
RFP
NE-YFP
MBP
E
3D co-cultures: iNE+iAST+iOLG+MG
AbO4-1mo
AbO4-1mo
RFP
K9JA
MBP

Fig 4 - Gene expression analysis confirms increased expression of myelin genes after O4 purification and co-culture in 3-dimensional brain tissue models demonstrates the formation of myelin-like structures. (A) Heatmap illustrating the temporal RT-qPCR analysis of the genes indicated on the left during the iOLGs differentiation protocol. Expression levels are normalised to day 2, with a cutoff of 33 cycles. Values were colour coded as shown on top. Data are represented as the fold change of the mean of 3 independent experiments. MKI67: Ki-67, marker of cell proliferation; PAX6: paired box 6, neuronal precursor marker; OLIG2 (endo): endogenous expression of OLIG2; SOX10 (overexp): Dox induced SOX10 overexpression; SYP: synaptophysin, synaptic marker; GFAP: glial fibrillary acidic protein, astrocytic marker. **(B)** Heatmap illustrating the RT-qPCR analysis of the marker genes comparing the non-sorted standard differentiation with O4+ SON-RFP sorted cells at equivalent timepoints. Expression levels are normalised to day 18, with a cut-off of 33 cycles. Values were colour coded as shown on top. Data are represented as the fold change of the mean of 3 independent experiments. **(C)** Representative immunostaining of the O4+ SON-RFP cells co-cultured with iPSC derived neurons and astrocytes in monolayer (2D) after 1 month (1mo). MBP+ iOLGs processes (pink) align with TUBB3 neuronal segments (green) and form myelin-like structures. However, the 2D monolayer co-culture system is not efficient with very few OLGs forming myelin-like structures. Boxes in white represent high-magnification insets. Scale bar 100 μm. **(D and E)** Representative immunostaining of O4+ SON-RFP cells co-cultured with iPSC derived neurons (iNE expressing membrane YFP) and astrocytes (iAST) **(D)**; and iPSC derived neurons, astrocytes and microglia (iMG) **(E)** in 3D co-culture spheroid systems. O4+ sorted iOLGs (yellow) are added on top of the previously formed 3D co-cultures. The presence of RFP+ and MBP+ cells within the culture shows that iOLGs migrate and differentiate within the culture. MBP+ iOLG processes (pink) are found at 6 months with iNE and iAST (D) and at 1 month in cultures with iMG (E). In the latter condition a few iOLGs also appear to align with K9JA+ neuronal segments (green) and potentially form myelin-like structures. Boxes in white represent high-magnification insets. Scale bar 100 μm.

preserve the tissue cytoarchitecture (Centeno et al. 2018). O4+ sorted SON-iOLGs were therefore added to a 3D brain tissue model containing iPSC-derived neurons (expressing membrane YFP) and astrocytes for 6 months. At 1 month, the iOLGs migrate into the entire 3D co-culture and further develop into MBP+ cells, suggesting iOLGs migration and differentiation. iOLGs appear to be distributed along the periphery of the culture where the dense axonal tracts are found (James et al. 2021). At 6 month the cultures exhibited MBP+ iOLGs with a highly branched morphology (Fig 4D). Some tube-like MBP+ segments are visible, but the high density of neuronal signal (YFP) makes it hard to distinguish individual processes and effectively assess co-localization. Further optimization of immunohistochemistry methodologies will facilitate the study and characterization of iOLGs in complex co-culture systems. Interestingly, 3D co-culture systems with iPSC-derived neurons, astrocytes and microglia at 1 month already showed many MBP+ cells and segments that align along K9JA+ neurons when compared to 3D co-culture systems of similar age without microglia (Fig 4E). This evidence raises interesting questions about the role of microglia during myelinogenesis, and perhaps a clue to resolve current human cortical myelination protocols that despite the longer culture times, still show sparse myelin formation, with limited evidence for compaction and axonal domain formation (Marton et al. 2019).

Discussion

Human OLGs derived from iPSCs could provide a scalable, renewable and easy to genome-edit source of cells that can facilitate research into oligodendrocyte physiology, disease modelling and drug testing. Unfortunately, differentiation of human iPSCs into cortical myelinating oligodendrocytes is still challenging and the results often appear difficult to reproduce between groups. Among all publications, two protocols stand out as achieving high differentiation yields while reducing culture

time. These iPSCs derived OLGs showed similar transcription profiles to human primary cells and were able to myelinate neurons in *in vivo* demyelination mouse models (Ehrlich et al. 2017; García-León et al. 2018). These protocols therefore have the highest potential of producing iOLGs in a cost-effective manner, thus facilitating further research into human OLGs. In 2017, Ehrlich and colleagues showed that overexpression of three oligodendrocyte specific transcription factors, SOX10, OLIG2 and NKX6.2, substantially increased the oligodendroglial lineage commitment with 70% O4+ cells by 28 days, of which 30% became MBP+ by 35 days (Ehrlich et al. 2017). A year later, García-León and colleagues showed that integration of the SOX10 transcription factor alone in a safe harbour locus, is sufficient to generate iOLG with significantly higher yields of up to 89% O4+ cells and 100% MBP+ cells (García-León et al. 2018; García-León et al. 2020). Surprisingly, earlier publications provided evidence that cells overexpressing SOX10 alone ultimately failed to mature (Ehrlich et al. 2017; Pawlowski et al. 2017). Nevertheless, the different neuronal differentiation methodologies, different media compositions and treatment time frames used for each of these protocols could account for the apparent conflicting results. Therefore, we aimed to conduct a comparative study to establish the best approach to efficiently generate iOLGs.

To allow for a comparable analysis between the overexpression of the different transcription factors, we used a recombinase mediated cassette exchange system integrated in the safe harbour locus *AAVS1*. Safe harbour locus integration allows for stable transgene expression without negatively affecting the modified cell. This cannot be achieved using standard random integration methods, which are associated with well-known limitations like off-target effects, variable transgene and copy number integration and variable and unpredictable transgene expression levels (Lee et al. 2019; Ordovás et al. 2015). Using FLP-FRT recombination we generated two RMCE cell lines expressing SOX10-GFP and SON-RFP under the influence of a tetracycline-inducible promoter. No leaky transgene expression was seen in the absence of Dox, and the percentage of GFP and RFP cells increased in a dose-dependent manner reaching a plateau of ±43% and ±68% activation when cells were treated with 8 µg/mL Dox, respectively. These cell lines also show some minor transgene expression mosaicism and low levels of transgene silencing. Interestingly, the transgene silencing pattern is only observed for the constructs under the tetracycline-inducible promoter, as the MCL appears to uniformly express the GFP marker under the strong constitutive promoter CAGGS and is exacerbated when adding Dox after the neural lineage differentiation. Together, the data supports the observations that the *AAVS1* locus shows variable transgene inhibition in a sequence and lineage-dependent manner in *in vitro* iPSCs progeny (Ordovás et al. 2015).

We tested and optimised different elements of the iOLG differentiation protocol, among the most impactful: cell seeding densities, treatment time frames and Dox concentration. It is important to keep in mind that iOLGs differentiation is a multistep process and thus small variations at each step can accumulate and generate significantly different outcomes. Using the SOX10-GFP and SON-RFP cell lines, we observed similar rates (±28%) of oligodendroglial lineage specification (OLIG2+) after treatment with the dual SMAD inhibitors, RA and SAG. Showing that this medium composition allows for the sequential development of neuronal progenitors (PAX6+) by day 4 and OPCs (OLIG2+ and NKX2.2+) by day 10. High expression of OLIG2 by day 12 is essential for the subsequent OPC specification (Ordovás et al. 2015; García-León et al. 2018) and variations in the OLIG2+ cell rates between reports have been previously attributed to the biological variability associated with human donor cells, that can impact differentiation

potency and cellular heterogeneity (Volpato and Webber 2020).

By overexpressing oligodendrocyte specific transcription factors after OPC specification we accelerate oligodendrocyte differentiation. Our data shows that OPCs overexpressing SOX10-GFP and SON-RFP can indeed differentiate into mature oligodendrocytes, as indicated by the expression of MBP and O4. However, in our experiments SOX10 alone induced the expression of MBP protein in only ±5% of the cells, which is in sharp contrast with previously reported yields of 89% (García-León et al. 2018; García-León et al. 2020). The transcription factors combination, SOX10, OLIG2 and NKX6.2, substantially increased the oligodendroglial lineage commitment, resulting in a significantly higher percentage of MBP+ cells: ±12% of the total cell number and ±31% of the total RFP+ cells; in line with Ehrlich et al. 2017.

As both cell lines behave the same up until the glial progenitor stage at day 12, the cellular phenotype after Dox treatment is solely driven by the transcription factor overexpression. During OLG development OLIG2 expression induces the initial expression of SOX10. SOX10 is both a target gene and an interactor of OLIG2 creating a positive feedback loop that maintains OLIG2 expression in SOX10-expressing cells. Because the transcription factors OLIG2 and SOX10 jointly define oligodendrocyte identity, overexpression of these transcription factors after oligodendroglial specification will promote the cells to establish the specific regulatory network that ensures the maintenance of oligodendroglial identity, as well as proper lineage progression and eventually terminal differentiation and myelination (Goldman and Kuypers 2015; Emery et al. 2009). Due to the network complexity, it is possible that by overexpressing SOX10 alone we create an imbalance in the overall transcription factors threshold leading to the lower differentiation rates observed in the SOX10-GFP cell line (Liu et al. 2007).

To increase oligodendrocyte differentiation efficiency and eliminate contaminant cells, we established a cell sorting step using antibodies against A2B5 and O4 surface antigens. SOX10-iOLG and SON-iOLGs were isolated with A2B5 magnetic beads and after 13 days *in vitro* approximately ±2 and ±13% of the cells, respectively, became MBP+ but showed an immature and highly ramified morphology. In contrast, ±25% of the similarly isolated and cultured O4+ cells from the SON-RPF line differentiated into MBP expressing myelinating iOLGs with myelin-like sheaths. Indeed, the data showed that O4 is the preferred purification target as it significantly improved iOLGs differentiation yields, while efficiently reducing the population heterogeneity, when compared to both the non-sorted protocol and A2B5 sorted cells.

To further characterise the stages of oligodendrocyte development in SON-iOLGs, we performed RT-qPCR analysis and compared the expression levels of several oligodendrocyte markers. Before the ectopic expression of the SON-RFP transcription factors begins, the observed pattern of gene expression is consistent with the sequential occurrence of different cell states: from pluripotent stem cells to neuronal precursors and finally OLIG2+ and NKX2.2+ glial progenitors. We additionally confirmed the expression of mature oligodendrocytes markers such as MBP, PLP1, MOG and MAG. As previously reported, we did not observe any PDGFRA+ cells, which was further confirmed by its low gene expression levels. The accelerated differentiation caused by the ectopic expression of the transcription factors could potentially bypass some of the intermediate OPC stages and force the direct conversion of OLIG2+ NPCs to late O4+ OLGs (García-León et al. 2018; Zhou et al. 2020). Future studies are necessary to confirm transcriptional similarity between the cells developed in this study and additional iPSC-OLG lines and primary human cortical oligodendrocytes.

The myelinating capacity of iOLGs was tested in *in vitro* co-cultures systems by adding SON-iOLGs into iPSC- derived neurons and astrocytes in 2D and 3D co-culture system for up to 6 months. O4+ sorted iOLGs migrate and differentiate within 2D and 3D co-cultures. In 2D co-cultures, MBP+ iOLG processes were found to be aligned along TUBB3 neuronal fibres. However, these events were neither frequent, nor reproducible to the same extent in the various trials. Similar observations have led researchers to functionally validate iOLGs by grafting these cells in the CNS of immune- and MBP-deficient shiverer mice (*Shi/Shi Rag2−/−)* (García-León et al. 2018; Ehrlich et al. 2017). Similar to slice cultures and xenografts, 3D iPSC co-culture systems offer some advantages relative to 2D systems, such as the ability to maintain long-term cultures and a microenvironment that can better mimic and preserve the tissue cytoarchitecture and cell-types (Centeno et al. 2018). At 1 month, in *in vitro* 3D co-cultures systems O4+ sorted SON-iOLGs appear to be distributed along the periphery of the culture. At 6 months, the iOLGs develop into MBP+ cells with a highly branched morphology of pre-mOLGs. These results suggest that even after 6 months in culture, iOLGs are not yet fully mature and might need even longer culture times to fully myelinate the neuronal spheroid. Even though not encouraging, this result was not unexpected, after all human cortical myelination is a process that spans several decades, which is likely one of the factors as to why current human cortical myelination protocols, still show inefficient myelin formation, with limited evidence for compaction and axonal domain formation (Marton et al. 2019; Madhavan et al. 2018). Indeed, surprising was the effect of microglia in 3D co-culture systems with iPSC- derived neurons, astrocytes and oligodendrocytes at 1 month. These cultures already show many MBP+ cells and segments that align along K9JA+ neurons, especially when compared to a culture without microglia. This evidence raises interesting questions about the role of microglia during myelinogenesis and requires further investigation. Due to the inconsistency in the directionality of axons in spheroid co-culture systems, it is difficult to quantify myelin wrapping by traditional immunohistochemistry. Future methods need to be developed to better quantify the extent of compact myelination, which together with electron microscopy analysis of myelin compaction would allow us to assess the later stages of oligodendrocyte maturation and myelination.

In summary, we demonstrated that overexpression of transcription factors is a suitable method to rapidly generate human OLGs from iPSCs. However, significant efficiency variations were found between the transcription factors. Overexpression of only SOX10 promotes the expression of both O4 and MBP oligodendrocytes, but these cells show a more immature morphology and low yields. On the other hand, the combination of three transcription factors, SOX10, OLIG2, and NKX6.2, greatly improved the differentiation efficiency. Suggesting that the OLG differentiation regulatory network might be sensitive to an imbalance between SOX10 and OLIG2 gene expression. Our work highlights that the use of safe harbour strategies can reduce confounding factors when comparing phenotypes between gene edited cells, but it can also introduce some transgene expression mosaicism and low levels of transgene silencing, which can impact the line efficiency. These limitations can be overcome by introducing an antigen purification step to remove any undifferentiated cell and reduce sample heterogeneity. Using the early-stage OPC marker A2B5, we were able to culture iOLG cells with an immature and highly ramified morphology, suggesting that this sorting antigen might be useful for research on OPC biology and earlier stages of oligodendrocyte differentiation. However, as the A2B5 antigen is found in other glial cells and developing neurons and as such the

resulting culture shows high levels of heterogeneity. The early pre-mOLG marker O4, is the preferred purification alternative for research with a focus on more mature iOLGs, as it significantly improved oligodendrocyte differentiation yields and efficiently reduced the population heterogeneity. Further research is needed to fully characterise the nature of iOLGs generated via ectopic expression of transcription factors. A better understanding of these cells could help to establish the best strategies for future genetic and chemical screens, and its suitability for disease modelling. Moreover, continuous improvement of the established protocols will promote and facilitate the utilisation of the iPSC technology to study the mechanisms and pathways of human OLG migration and myelination.

Materials and Methods

Cell Lines and culture. iPSC experiments were performed in accordance with all relevant guidelines and regulations. The female human episomal iPSC line A18944 used in this study was purchased from ThermoFisher Scientific (A18945). iPSCs were maintained on vitronectin-coated (ThermoFisher Scientific, A14700) cell culture plates and grown in StemFlex Medium (ThermoFisher Scientific, A3349401) at 37°C with 5% CO2. The master cell line and RMCE cell lines were kept under constant selection pressure by adding 50 µg/mL Hygromycin B (Merck, H3274) and 300 ng/mL of puromycin dihydrochloride (Merck, P8833), respectively.

Generation of the Master Cell Lines and RMCE Lines. For the generation of the master cell line, the pZ:F3-CAGGS GPHTK-F gene targeting vector was previously described in Ordovás et al. 2015 and kindly provided by Catherine Verfaillie, Lueven, Belgium. Two million A18944 iPSCs were transfected with 32 µg of the gene targeting vector and 4 µg of AAVS1 locus specific Transcription activator-like effector nucleases (TALEN) plasmids, pTALEN-TD_hAAVS1-1L and pTALEN-TG_hAAVS1-1R (kindly provided by Dominik Paquet) in Mirus Ingenio electroporation solution (Mirus, MIR50111) using the Gemini X2 Electroporation System (BTX) with 2 pulses at 65 mV for 20 ms in a 1 mm cuvette (Fisher Scientific, 15437270). Cells expressing GFP-2A-HYGTK were selected by sorting for GFP and with 50 µg/mL Hygromycin B (Merck, H3274) starting 3 days after electroporation. Single-cell clone colonies were picked and genotyped by PCR and qPCR assays.

For the generation of the RMCE cell lines, the SOX10-GFP RMCE vector, pZ_M2rTA_CAGG_TetON-Sox10_2A_eGFP, was previously described in García-León et al. 2018 (kindly provided by Catherine Verfaillie, Lueven, Belgium). The construction of the polycistronic SF-SON-IRES-Tomato plasmid has also been described by Ehrlich et al. 2017 and was kindly provided by Tanja Kuhlmann, Muenster, Germany. The SON-RFP RMCE vector was generated by replacing the Sox10-2A-GFP fragment in the backbone pZ_M2rTA_CAGG_TetON-Sox10_2A_eGFP, with the SON-IRES-Tomato fragment from the SF-SON-IRES-Tomato plasmid, using Gibson Assembly with oligo stitching, listed in Table S1. The master cell line containing the FRT-flanked cassette, together with a FLP recombinase plasmid CAG_FLP_GFP (Addgene, #13788), were used to recombine the SOX10-GFP and SON-RFP containing plasmids into the AAVS1 locus. The cassette exchange was performed by electroporating 14 µg of RMCE vectors and 4 µg of FLP plasmid as described above. Selection was started 4 days after transfection with 300 ng/mL of puromycin dihydrochloride (Merck, P8833) for seven days. Negative selection was initiated by adding 0.5 µM of Fialuridine (FIAU) (Merck, SML0632) for 3 days. Single-cell colonies resistant to Puro and FIAU were manually picked and expanded for further characterization.

Cell line characterization: genotyping PCR and qPCR. For the characterization of the cell lines, genomic DNA (gDNA) was isolated with a NucleoSpin Tissue Kit (Macherey-Nagel, 740952) according to manufacturer's instructions. PCR genotyping was done using 50 ng of gDNA with OneTaq Master Mix (New England BioLabs, M0482) in 10 µL reactions. PCR products were analysed by agarose gel electrophoresis with a 1 kb Plus DNA ladder (New England BioLabs, N3232). Primer sequences of PCRs carried out on Fig Sup1 and 2 are listed in Table Sup1.

Single cell clones can develop partial Trisomy 20 at the *Bcl-XL* locus (*BCL2L1* gene) as it provides the

cells a growth and survival advantage. *BCL2L1* gene copy number was determined by qPCR genotyping, as previously described by Weisheit et al. 2020. Freshly isolated gDNA was mixed with 2x PrimeTime Gene Expression Master Mix (IDT, 1055772), 20x human TERT TaqMan Copy Number Reference Assay (ThermoFisher Scientific, 4403316) as internal reference control, *BCL2L1* target primers (0.5 pmol/µl) and the designed PrimeTime Eco Probe 5′ 6-FAM/ZEN/3′ IBFQ (0.25 pmol/µl, HPLC-purified, IDT). The qPCR reaction was run for 2 min at 50°C, 10 min at 95°C, followed by 40 cycles of 15 s at 95°C and 1 min at 60°C. Allele copy numbers were determined by ddCt method relative to internal TERT reference and the previously karyotyped wild type control. In similar manner, proper cassette integration for the MCL line was corroborated by genotyping qPCR analysing of the relative GFP-HYG-TK cassette copy number. Assays primers and probes were designed using the IDT PrimerQuest design tool, by inputting a region spanning the GFP and HYG sequences and setting the amplicon size range to 300-450 bp. Genotyping qPCR primer and probe sequences are listed in Table Sup1.

Oligodendrocyte differentiation protocol. To induce oligodendrocyte differentiation of the SOX10-GFP and SON-RFP iPSC lines, we followed a similar approach previously described by García-León et al. 2018. iPSCs were dissociated into single cells using Accutase (Merck, A6964) and seeded at a density of 20.000 cells/cm2 on GelTrex (ThermoFisher Scientific, A1413302) coated plates in StemFlex medium supplemented with 10 µM rock inhibitor analog (Selleck Chemical, Y27632) (D-2). At day 0 (D0), media was changed to N2B27 medium (Table Sup2) supplemented with the dual SMAD inhibitors: 10 µM SB431542 (SB) and 0.25 µM LDN193189 (LDN); and 100 nM retinoic acid (RA). At D8, 1 µM of smoothened agonist (SAG) was further added to the media. Media was changed daily. On D12, cells were split on culture plates coated for 4 hours with poly-L-ornithine (Merck, P3655) and overnight with laminin (ThermoFisher Scientific, 23017015) diluted 1:100 in 1xPBS. Cells were dissociated using Accutase and seeded at 75.000 cell/cm2 for standard differentiation and at 150.000 cell/cm2 for O4 purification in oligodendrocyte differentiation media (Table Sup3) supplemented with 2 µg/mL of doxycycline. Cells were maintained in oligodendrocyte differentiation media with doxycycline for up to an additional 20 days (D32), changing the medium every 2-3 days. Doxycycline response experiments were performed to assess the purity and dose response of the cell lines. In a similar manner, the effect of cell seeding density at D12 in iOLG maturation efficiency was evaluated in both cell lines.

O4 purification. After the low density split at day 12 (D12), cells maintained for 6-8 days in oligodendrocyte differentiation media (D18-D20). Early pre-myelinating oligodendrocytes were purified using O4 microbeads (Miltenyi Biotec, 130-094-543) as described by the manufacturer. Purified cells were seeded at 25.000 cell/cm2 in poly-L-ornithine/laminin coated coverslips in oligodendrocyte differentiation media supplemented with 2 µg/mL of doxycycline. Purified O4+ cells were used for transcriptome analysis by RT-qPCR or in co-culture systems.

Immunocytochemistry. Cells were fixed using 4% paraformaldehyde (PFA) for 10 min and carefully washed in 1x phosphate buffer saline (PBS). The cells were permeabilized on ice for 10 minutes in 0.1% Triton X100 (Merck, X100) and 0.1% Sodium citrate (Merck, 25114) in 1xPBS. The cells were further incubated with blocking solution (2.5% fetal calf serum (FCS), 2.5% bovine serum albumin (BSA), 2.5% fish gelatine in 1xPBS) for 30 min at RT. Primary antibodies diluted in 10% blocking solution were incubated overnight at 4°C, washed carefully 3x with PBS, followed by incubation with secondary antibodies (1:500) diluted in 1% blocking solution for 1-2h at RT. Nuclei were stained with Hoechst 33342 (1:1000, ThermoFisher Scientific, H3570) for 10 min at room temperature. The stained cells attached to coverslips were mounted onto a glass slide using ProLong Diamond Mounting Medium (ThermoFisher Scientific, P36961) and dried overnight in the dark prior to imaging. The primary antibodies used were the following: anti-GFP rabbit (1:2000, Thermofisher Scientific, A-6455); anti-RFP rabbit (1:1000, Thermofisher Scientific, R10367); anti-OCT4 rabbit (1:500, Stemgent, S090023); anti-Tra160 mouse (1:500, Millipore, MAB4360); anti-SOX10 mouse (1:150, Invitrogen, 14-5923-80); anti-OLIG2 goat (1:200, R&D Systems, AF2418); anti-PAX6 rabbit (1:500, Covance, PRB-278P); anti-

NKX2.2 mouse (1:5, DSHB, 74.5A5); anti-MBP rat (1:500, Abcam, ab7349); anti-O4 IgM mouse (1:200, Sigma-Aldrich, O7139); anti-TUB3 mouse (1:200, Promega, G712A) and anti-K9JA (1:500, Dako, A0024). Fluorescent secondary antibodies include: Alexa Fluor 488, Alexa Fluor 555 and Alexa Fluor 647 raised in both goat and donkey, together with goat anti-mouse IgM Alexa Fluor 488 (A-21042) and goat anti-mouse IgM Alexa Fluor 647 (A-21238) were purchased from ThermoFisher Scientific and used depending on the experimental instructions.

Immunohistochemistry of 3D culture systems. To prepare the 3D co-culture samples for immunohistochemistry, the cultures were transferred and fixed in 4% PFA at RT for 30 min to 1h and washed with PBS and cryoprotected in 30% sucrose in 1xPBS for 48 to 72h. The cultures were embedded in Tissue-Tek O.C.T, frozen on dry ice and immediately sectioned. Cultures were sectioned using a cryostat (CryoStar NX70, Thermo Scientific) to cut 30-40 µm thick sections and stored at 4°C in 1xPBS with 0.01% sodium azide (Merck, S2002). For staining the sections, they were first placed in Superfrost Plus slides and dried at 37°C for 10 minutes. Mounted samples were then rehydrated with 1xPBS. To prevent non-specific binding, sections were incubated for 1 hour with blocking solution (3% donkey serum (Jackson ImmunoResearch, 017-000-121); 0.1% Triton X-100; 0,01% sodium azide in 1xPBS). Primary antibodies were diluted in blocking solution and incubated overnight at 4 °C. The sections were further washed with 1xPBS and incubated with secondary antibodies (1:500) diluted in blocking solution for 2 hours at RT. After washing with 1xPBS, the sections were then incubated with DAPI (1:10 000) in 1xPBS for 15 minutes and mounted with ProLong Diamond Mounting Medium.

Quantitative RT-qPCR. Total RNA was extracted from cells using the NucleoSpin RNA/Protein kit (Macherey-Nagel, 740933.50) according to the manufacturer's instructions. The RNA was retrotranscribed with SuperScript IV First-Strand Synthesis System (ThermoFisher Scientific, 18091050), using random hexamer primer and 250 ng of total RNA, as determined by NanoDrop absorbance at A260. Quantitative PCR was performed using the PowerUp SYBR Green Master Mix (Applied Biosystems, A25742) on a LightCycler 480 Real-time PCR system (Roche). Specificity of the primers used for RT-PCR reactions was determined beforehand by agarose gel electrophoresis. The melting curve of each sample was determined to ensure the specificity of the products. The quantitative RT-PCR conditions were 2 min at 50 °C, 10 min at 95 °C, 40 cycles of 15 s, at 95 °C, and 1 min at 60 °C. Relative expression levels were calculated using the ddCt method and GAPDH as the housekeeping gene. Samples were further normalised to the starting sample (D2 for standard differentiation, Fig 4A and D18 for Ab purification, Fig 4B). All qPCR reactions were run in duplicate. The primer sequences used in this study are listed in Table Sup4.

***In vitro* myelination assays.** To assess the *in vitro* functionality of SON-RFP iOLGs, O4+ cells were purified at differentiation day 18 by magnetic cell sorting. Purified O4+ iOLGs were added to iPSC-derived neuronal and astrocytic cultures previously plated in 2D co-culture systems and 3D co-culture systems with and without microglia.

Cortical neurons were differentiated based on dual-SMAD inhibition protocol. Briefly, iPSCs were cultured until 70-80% confluent. Media was changed daily with increasing percentages of neural maintenance medium supplemented with 10 µM SB and 0.25 µM LDN (NI, Table Sup5). On D0 media was changed to 2/3 Essential 6 media (E6, Table Sup6) mixed with 1/3 of NI medium; and on D1 it was changed to 1/3 E6 media mixed with 2/3 NI medium. On D2, cells were split into single cells using Accutase, resuspended in NI medium supplemented with 10 µM rock inhibitor (RI) and plated on GelTrex coated 12-well plates at 1 million cells per well. Media was changed daily until D8/9. Subsequently, cells were split in high-density 'spots' on dried 6-well poly-L-ornithine/laminin coated plates. Before cell dissociation, the laminin solution was aspirated, and the plates were left open to dry. Cells were then split with Accutase and resuspended in NI medium supplemented with RI at 30 million cells/mL. 250-350 µl of the cell suspension were carefully added to each well to form spots. After one hour, 2 ml NI medium supplemented with RI were carefully added to each well. On D11 medium was changed to NM medium supplemented with 20 ng/mL of bFGF (Stemcell Technologies, 78003.2) for two consecutive days.

Cells were then maintained in NM until neural rosettes accumulated around D20-23. At this point, cells were incubated with 1 ml StemDiff Neural Rosette Selection Reagent (NRSR, StemCell Technologies, 5832) for 1h at 37°C. Rosettes from the center of the spot were manually isolated using a pipette tip, centrifuged and resuspended in NM medium supplemented with 20 ng/mL bFGF and plated on poly-L-ornithine/laminin coated 6-well plates. The following day, cells were fed with NM medium supplemented with bFGF and then maintained in NM until rosettes became almost confluent by D28-31. Cells were dissociated with Accutase and the rosettes were plated on poly-L-ornithine/laminin coated 6-well plates in NM medium supplemented with bFGF for two days. Rosettes were maintained in NM medium until D35-38 and then split for 2D or 3D cultures.

iPSCs differentiation into astrocytes was performed following the protocol by Perriot et al. 2018 with minor modifications. IPSCs were differentiated as in the cortical neuron differentiation protocol until rosettes were first visible on D14-15. Media was changed to glial precursor expansion medium (GPE, Table Sup7) and exchanged daily. At D17-18, rosettes were split using the NRSR method described above and plated into poly-L-ornithine/laminin coated 6-well plates with GPE medium. Cells were cultured until confluent and then split using Accutase, resuspended in GPE medium and plated on GelTrex coated 12-well plates at 1 million cells per well. Once the cells were confluent, they were split using Accutase, seeded at 0,5 million cells per well and cultured in astrocyte induction medium (AIM, Table S8) to induce neural to glial precursor cell transition. Media was changed every other day for 14 days and split when confluent using Accutase and plated in GelTrex coated 6-well plates at 0.5 million cells/ml. At D31-32, media was changed to astrocyte medium (AM, Table Sup9) supplemented with 20 ng/ml CNTF (Peprotech, 450-13) to induce astrocyte maturation. Cells were split as needed for 28 days and the media was then changed to AM medium, until they split for 2D or 3D cultures.

Differentiation of iPSCs to microglia was performed following the protocol by McQuade et al. 2018 with minor modifications. 70-90% confluent cells were split using 0.5 mM EDTA (ThermoFisher Scientific 15575020) in 1xPBS. Cells were plated at low density (1:100-1:200 split to get around 40 colonies per well) on GelTrex coated 6-well plates in Essential 8 medium (E8, ThermoFisher Scientific, A1517001). The next day (D0) the media was changed to Medium A of the StemDif Hematopoietic kit (StemCell Technologies, 05310). On D2, half of the media was changed with fresh media and on D3, media was completely changed to Medium B of the StemDif Hematopoietic kit. On D5 and 7, half of the medium was replaced and on D10, 1 ml of medium was added on top. On D12 the floating hematopoietic precursor cells (HPCs) were harvested and plated on GelTrex coated 6-well plates at 160.000 cells/well in microglia differentiation medium (DM1, Table Sup10). On D14 and D16, 1 ml of DM1 was added on top. On D18 cells were washed off the plate and 50% of the medium was transferred to new GelTrex coated 6-well plates and 1 ml DM1 was added on top. On D20 and D22 again 1 ml DM1 was added on top. On D24 cells were collected and resuspended in NB+/B27+ medium (Table Sup11) with the microglial specific growth factors and added on 3D cultures.

For the neuron, astrocyte and oligodendrocyte 2D co-culture experiments, neurons and astrocytes were generated as described above and plated at densities of 0.5M per well and 0.3M, respectively, in 24-well plates containing poly-L-ornithine/laminin coated glass coverslips and NB+/B27+ medium supplemented with 10 µM DAPT (Selleck Chemical, S2215). After three days, the media was replaced with NB+/B27+ supplemented with 10µM DAPT, 5 µM 5-Fluorouracil (Merck, F6627). Afterwards, half the medium was replaced 2-3x per week. DAPT was added for a total of 7 days while 5-Fluorouracil and uridine were added for a total of 10 days. O4+ iOLGs were then added to the 2D co-culture system at a density of 25.000 cells/well in NB+/B27+ medium supplemented with oligodendrocyte factors described in the oligodendrocyte differentiation media (Table Sup2).

For the 3D culture experiments, neurons and astrocytes were generated as described above and transferred to ultra-low attachment 96-well round-bottom plates (Merck, CLS7007-24EA) at 250.000 cells/well (3x neurons: 1x astrocyte ratio), in NB+/B27+ medium supplemented with 10 µM DAPT and spun down at 250g for 4 min. 3D co-culture systems were then treated as described above with DAPT added to the medium for a total of 7 days, and 5-Fluorouracil for a total of 10 days. O4+ iOLGS were then added to the 3D co-culture system

at a density of 13.000 cells/well in NB+/B27+ medium supplemented with oligodendrocyte factors. The oligodendrocytes were allowed to migrate and incorporate into the 3D co-culture for 7 days. Afterwards, the 3D co-cultures systems were transferred to 12-well wells coated with anti-adherence rinsing solution (StemCell Technologies, 07010) for long-term culture.

In 3D co-culture systems with microglia, neurons, astrocyte, oligodendrocyte co-culture systems were prepared as above until the incorporation of oligodendrocytes, at which point D24 microglia was added to the culture at a density of 40.000 microglia/well in NB+/B27+ medium supplemented with oligodendrocyte factors and microglia factors described in DM1 (Table S10). Microglia were allowed to migrate into the cultures for 7 days, cultures were transferred back to 12-well plates coated with anti-adherence rinsing solution for long-term culture.

Image acquisition and analysis. Optical sections were acquired with a confocal laser-scanning microscope (Leica TCS SP5, Leica Microsystems) using the 20×Air/0.75 NA and the 63×Oil/1.40 NA objectives. The different fluorophores were stimulated sequentially using the following laser lines: 405 nm for DAPI, 488 nm for Alexa Fluor 488, 561 nm for Alexa Fluor 555 and 633 nm for Alexa Fluor 647.

Statistical Analysis. Statistical analysis was performed with GraphPad Prism 7 v7.04 software (GraphPad Software). Data are represented as mean ± SD. The number of cell cultures used for each experiment are indicated in the figure legends. Each biological replicate represents an average of 9 fields of view to account for variability within the biological sample. To compare two groups, an unpaired multiple t-test corrected for multiple comparisons with Holm-Sidak method was applied using the GraphPad Prism software. A p value of ≤0.05 was considered significant in all cases.

Data availability

The raw data that support the findings of this study are available from the corresponding author upon reasonable request.

References

Bradl, M., & Lassmann, H. (2010). Oligodendrocytes: biology and pathology. *Acta Neuropathologica*, 119(1), 37–53.

Centeno, E. G. Z., Cimarosti, H., & Bithell, A. (2018). 2D versus 3D human induced pluripotent stem cell-derived cultures for neurodegenerative disease modelling. *Molecular Neurodegeneration*, 13(1), 27.

Chambers, S. M., Fasano, C. A., Papapetrou, E. P., Tomishima, M., Sadelain, M., & Studer, L. (2009). Highly efficient neural conversion of human ES and iPS cells by dual inhibition of SMAD signaling. *Nature Biotechnology*, 27(3), 275–280.

Chanoumidou, K., Mozafari, S., Baron-Van Evercooren, A., & Kuhlmann, T. (2020). Stem cell derived oligodendrocytes to study myelin diseases. *Glia*, 68(4), 705–720.

Chan, H. Y., V, S., Xing, X., Kraus, P., Yap, S. P., Ng, P., Lim, S. L., et al. (2011). Comparison of IRES and F2A-based locus-specific multicistronic expression in stable mouse lines. *Plos One*, 6(12), e28885.

Czepiel, M., Boddeke, E., & Copray, S. (2015). Human oligodendrocytes in remyelination research. *Glia*, 63(4), 513–530.

Douvaras, P., Wang, J., Zimmer, M., Hanchuk, S., O'Bara, M. A., Sadiq, S., Sim, F. J., et al. (2014). Efficient generation of myelinating oligodendrocytes from primary progressive multiple sclerosis patients by induced pluripotent stem cells. *Stem cell reports*, 3(2), 250–259.

Ehrlich, M., Mozafari, S., Glatza, M., Starost, L., Velychko, S., Hallmann, A.-L., Cui, Q.-L., et al. (2017). Rapid and efficient generation of oligodendrocytes from human induced pluripotent stem cells using transcription factors. *Proceedings of the National Academy of Sciences of the United States of America*, 114(11), E2243–E2252.

Emery, B., Agalliu, D., Cahoy, J. D., Watkins, T. A., Dugas, J. C., Mulinyawe, S. B., Ibrahim, A., et al. (2009). Myelin gene regulatory factor is a critical transcriptional regulator required for CNS myelination. *Cell*, 138(1), 172–185.

Emery, B. (2010). Regulation of oligodendrocyte differentiation and myelination. *Science*, 330(6005), 779–782.

Franklin, R. J. M., Frisén, J., & Lyons, D. A. (2021). Revisiting remyelination: Towards a consensus on the regeneration of CNS myelin. *Seminars in Cell & Developmental Biology*, 116, 3–9.

García-León, J. A., García-Díaz, B., Eggermont, K., Cáceres-Palomo, L., Neyrinck, K., Madeiro da Costa, R., Dávila, J. C., et al. (2020). Generation of oligodendrocytes and establishment of an all-human myelinating platform from human pluripotent stem cells. *Nature Protocols*, 15(11), 3716–3744.

García-León, J. A., Kumar, M., Boon, R., Chau, D., One, J., Wolfs, E., Eggermont, K., et al. (2018). SOX10 Single Transcription Factor-Based Fast and Efficient Generation of Oligodendrocytes from Human Pluripotent Stem Cells. *Stem cell reports*, 10(2), 655–672.

Goldman, S. A., & Kuypers, N. J. (2015). How to make an oligodendrocyte. *Development*, 142(23), 3983–3995.

Huang, W., Bhaduri, A., Velmeshev, D., Wang, S., Wang, L., Rottkamp, C. A., Alvarez-Buylla, A., et al. (2020). Origins and proliferative states of human oligodendrocyte precursor cells. *Cell*, 182(3), 594-608.e11.

Jakovcevski, I., Filipovic, R., Mo, Z., Rakic, S., & Zecevic, N. (2009). Oligodendrocyte development and the onset of myelination in the human fetal brain. *Frontiers in Neuroanatomy*, 3, 5.

James, O. G., Selvaraj, B. T., Magnani, D., Burr, K., Connick, P., Barton, S. K., Vasistha, N. A., et al. (2021). iPSC-derived myelinoids to study myelin biology of humans. *Developmental Cell*, 56(9), 1346-1358.e6.

Kuhn, S., Gritti, L., Crooks, D., & Dombrowski, Y. (2019). Oligodendrocytes in development, myelin generation and beyond. *Cells*, 8(11).

Lee, J. S., Kildegaard, H. F., Lewis, N. E., & Lee, G. M. (2019). Mitigating clonal variation in recombinant mammalian cell lines. *Trends in Biotechnology*, 37(9), 931–942.

Liu, Z., Hu, X., Cai, J., Liu, B., Peng, X., Wegner, M., & Qiu, M. (2007). Induction of oligodendrocyte differentiation by Olig2 and Sox10: evidence for reciprocal interactions and dosage-dependent mechanisms. *Developmental Biology*, 302(2), 683–693.

Madhavan, M., Nevin, Z. S., Shick, H. E., Garrison, E., Clarkson-Paredes, C., Karl, M., Clayton, B. L. L., et al. (2018). Induction of myelinating oligodendrocytes in human cortical spheroids. *Nature Methods*, 15(9), 700–706.

Marton, R. M., Miura, Y., Sloan, S. A., Li, Q., Revah, O., Levy, R. J., Huguenard, J. R., et al. (2019). Differentiation and maturation of oligodendrocytes in human three-dimensional neural cultures. *Nature Neuroscience*, 22(3), 484–491.

Mitew, S., Hay, C. M., Peckham, H., Xiao, J., Koenning, M., & Emery, B. (2014). Mechanisms regulating the development of oligodendrocytes and central nervous system myelin. *Neuroscience*, 276, 29–47.

Moore, S., Meschkat, M., Ruhwedel, T., Trevisiol, A., Tzvetanova, I. D., Battefeld, A., Kusch, K., et al. (2020). A role of oligodendrocytes in information processing. *Nature Communications*, 11(1), 5497.

Naruse, M., Ishizaki, Y., Ikenaka, K., Tanaka, A., & Hitoshi, S. (2017). Origin of oligodendrocytes in mammalian forebrains: a revised perspective. *The Journal of Physiological Sciences*, 67(1), 63–70.

Nave, K.-A. (2010). Myelination and the trophic support of long axons. Nature Reviews. *Neuroscience*, 11(4), 275–283.

Ordovás, L., Boon, R., Pistoni, M., Chen, Y., Wolfs, E., Guo, W., Sambathkumar, R., et al. (2015). Efficient Recombinase-Mediated Cassette Exchange in hPSCs to Study the Hepatocyte Lineage Reveals AAVS1 Locus-Mediated Transgene Inhibition. *Stem cell reports*, 5(5), 918–931.

Pawlowski, M., Ortmann, D., Bertero, A., Tavares, J. M., Pedersen, R. A., Vallier, L., & Kotter, M. R. N. (2017). Inducible and Deterministic Forward Programming of Human Pluripotent Stem Cells into Neurons, Skeletal Myocytes, and Oligodendrocytes. *Stem cell reports*, 8(4), 803–812.

Saab, A. S., Tzvetanova, I. D., & Nave, K.-A. (2013). The role of myelin and oligodendrocytes in axonal energy metabolism. *Current Opinion in Neurobiology*, 23(6), 1065–1072.

Scolding, N. J., Rayner, P. J., & Compston, D. A. (1999). Identification of A2B5-positive putative oligodendrocyte progenitor cells and A2B5-positive astrocytes in adult human white matter. *Neuroscience*, 89(1), 1–4.

Stacpoole, S. R. L., Spitzer, S., Bilican, B., Compston, A., Karadottir, R., Chandran, S., & Franklin, R. J. M. (2013). High yields of oligodendrocyte lineage cells from human embryonic stem cells at physiological oxygen tensions for evaluation of translational biology. *Stem cell reports*, 1(5), 437–450.

Stadelmann, C., Timmler, S., Barrantes-Freer, A., & Simons, M. (2019). Myelin in the central nervous system: structure, function, and pathology. *Physiological Reviews*, 99(3), 1381–1431.

Stassart, R. M., Möbius, W., Nave, K.-A., & Edgar, J. M. (2018). The Axon-Myelin Unit in Development and Degenerative Disease. *Frontiers in Neuroscience*, 12, 467.

van Tilborg, E., de Theije, C. G. M., van Hal, M., Wagenaar, N., de Vries, L. S., Benders, M. J., Rowitch, D. H., et al. (2018). Origin and dynamics of oligodendrocytes in the developing brain: Implications for perinatal white matter injury. *Glia*, 66(2), 221–238.

Trotter, J., & Schachner, M. (1989). Cells positive for the O4 surface antigen isolated by cell sorting are able to differentiate into astrocytes or oligodendrocytes. Brain research. *Developmental brain research*, 46(1), 115–122.

Volpato, V., & Webber, C. (2020). Addressing variability in iPSC-derived models of human disease: guidelines to promote reproducibility. *Disease Models & Mechanisms*, 13(1).

Wang, S., Bates, J., Li, X., Schanz, S., Chandler-Militello, D., Levine, C., Maherali, N., et al. (2013). Human iPSC-derived oligodendrocyte progenitor cells can myelinate and rescue a mouse model of congenital hypomyelination. *Cell Stem Cell*, 12(2), 252–264.

Yang, Y., Lewis, R., & Miller, R. H. (2011). Interactions between oligodendrocyte precursors control the onset of CNS myelination. *Developmental Biology*, 350(1), 127–138.

Zhou, H., He, Y., Yang, Y., Wang, Z., Wang, Q., Hu, C., Wang, X., et al. (2020). Identifying the functions of two biomarkers in human oligodendrocyte progenitor cell development. *BioRxiv*.

Supplementary information

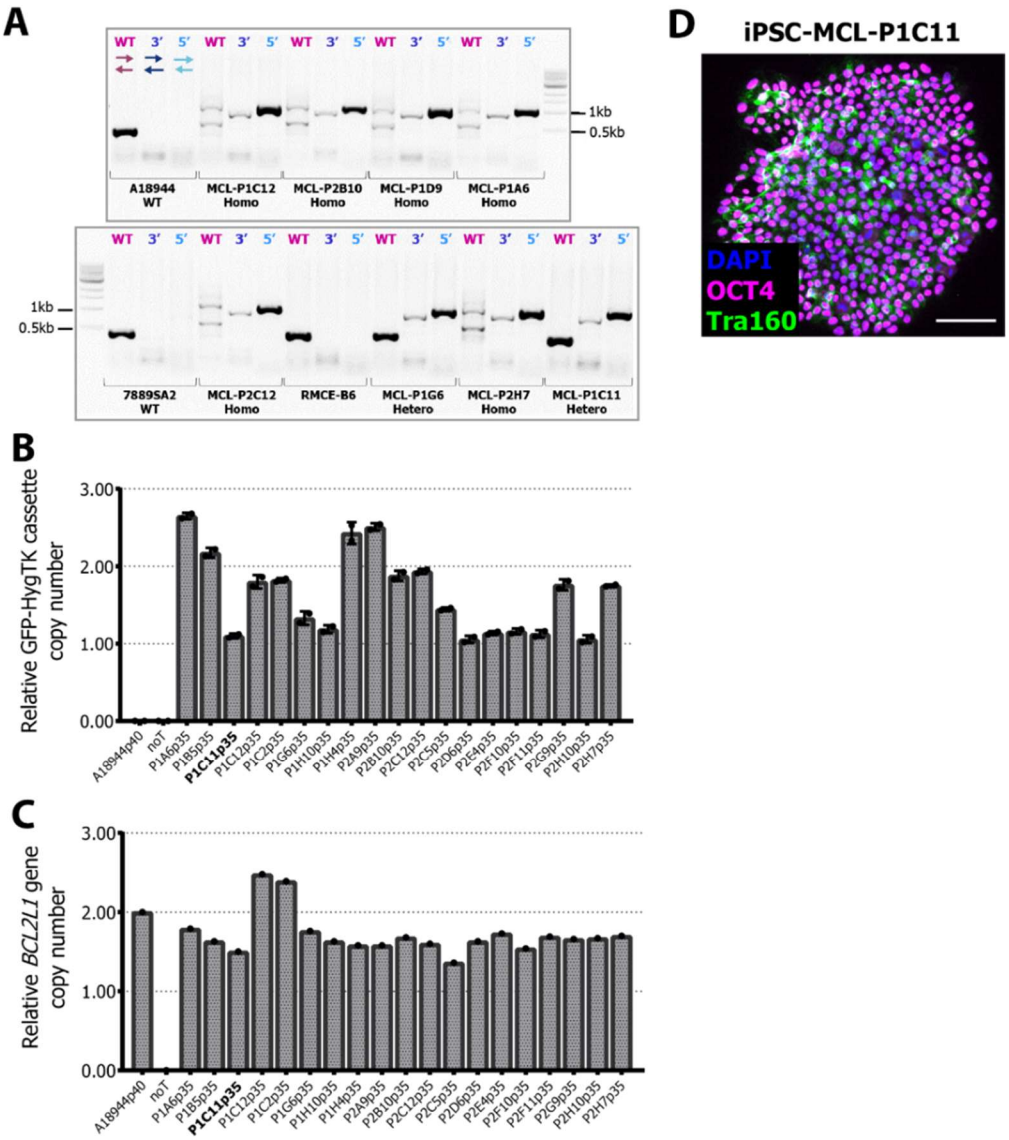

Fig Sup1 - Characterization of the iPSC master cell line (MCL). (A) PCR genotyping of correct integration of the MCL cassette in the *AAVS1* locus in the selected cell clones. The primers localizations is depicted in Fig 1A for the 3' and 5' integration and the wild type allele (WT). The RMCE-B6 cell line was used as a control for primer specificity to the MCL cassette. MCLs were characterised as homozygous (Homo) or heterozygous (Hetero) based on the presence of a WT band, which was further confirmed by **(B)** the relative GFP-HYG-TK cassette copy number. Data are represented as mean ± SD of 2 independent experiments. **(C)** Clones were screened for genetic alterations in the anti-apoptotic gene *BCL2L1* that frequently arise during repeated in vitro culture of iPSCs. A value close to 2 indicates normal copy number at BCL2L1. Data are represented as the mean of 2 technical replicates. **(D)** Representative immunohistochemistry image of a MCL clone expressing the pluripotency markers OCT4 (nuclear) and Tra-1-60 (cytoplasmic). Scale bar 100 µm.

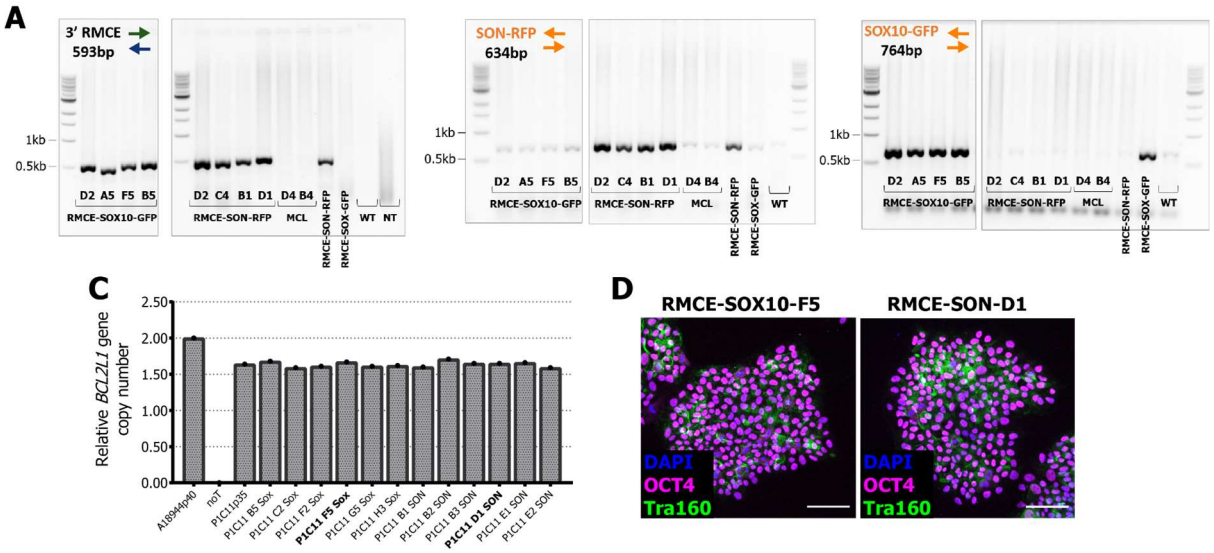

Fig Sup2 - Characterization of iPSC after the recombinase-mediated cassette exchange (RMCE). (A) PCR genotyping of correct exchange of the RMCE cassette in the AAVS1 locus. The primers localizations is depicted in Fig 1A for the 3' integration and the presence of the transcription factors sequences of interest (SON-RFP and SOX10-GFP). The MCL-D4 and B4 cell lines were used as a control for the primer's specificity to the RMCE cassette. **(C)** Clones were screened for genetic alterations in the anti-apoptotic gene *BCL2L1* that frequently arise during repeated in vitro culture of iPSCs. Data are represented as the mean of 2 technical replicates. **(D)** Representative immunohistochemistry image of two RMCE clones expressing the pluripotency markers OCT4 (nuclear) and Tra-1-60 (cytoplasmic). Scale bar 100 µm.

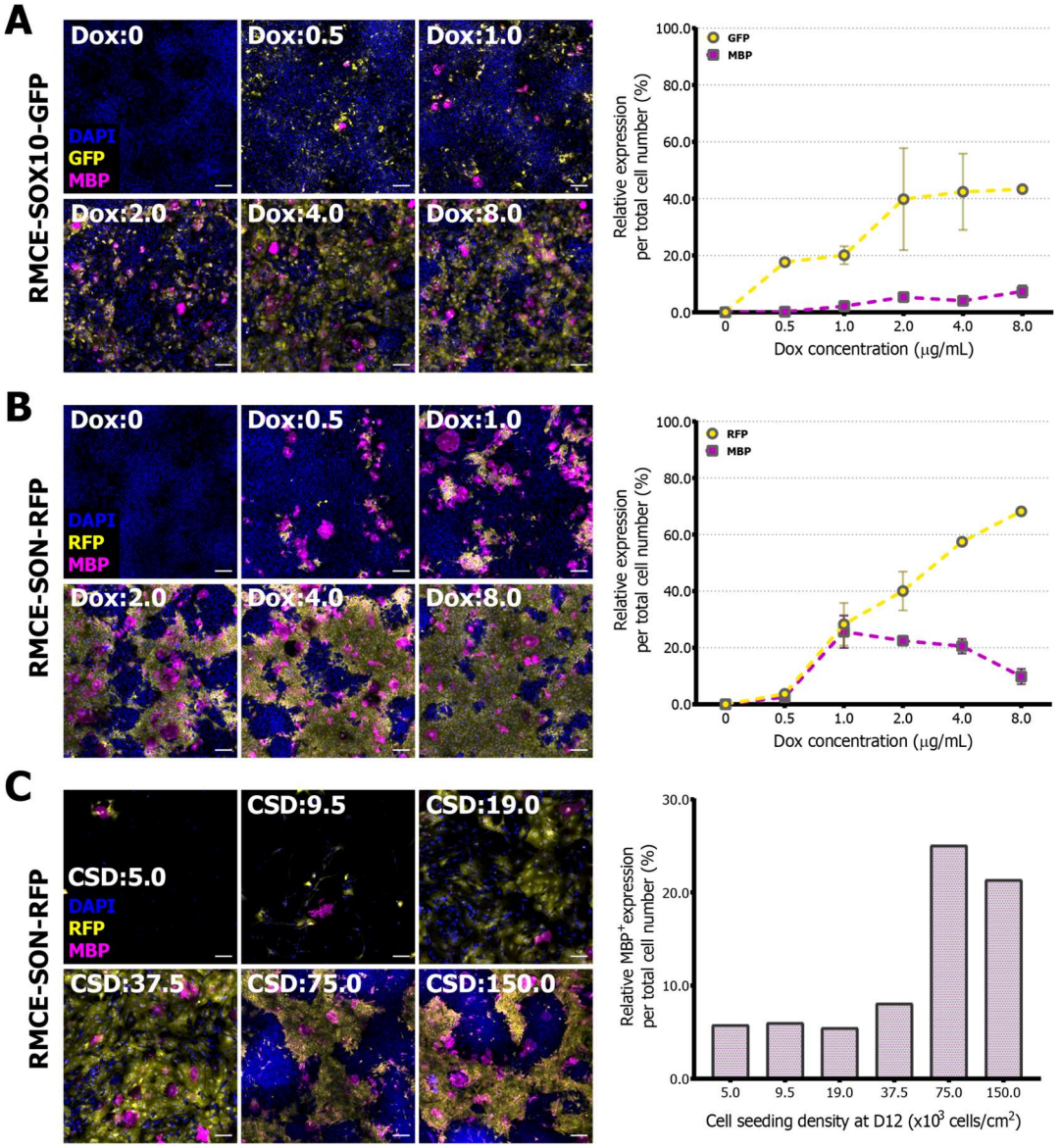

Fig Sup3 - Variations within cell seeding densities and Dox concentrations can accumulate and generate significantly different outcomes. (A and B) Representative immunostaining and quantification of the expression of the fluorescent marker (GFP and RFP, yellow) and MBP (pink) expression in cells treated with increasingly higher concentrations of Dox in µg/mL. No leaky transgene expression was observed in the absence of Dox, and the percentage of GFP and RFP cells increased in a dose-dependent manner. Cells treated with Dox concentrations above 4 µg/mL showed smaller myelin sheaths and increased overall cell death (data not shown). Data are represented as mean ± SD of 2 independent experiments. Scale bar 100 µm. **(C)** Representative immunostaining of the expression of the fluorescent marker (GFP and RFP, yellow) and MBP (pink) expression in cells seeded at increasingly higher densities at day 12. Quantification of the percentage MBP+ cells showed an increase towards higher cell seeding densities (CSD). Optimal cell seeding densities were established at 75K cells/cm2 for the standard differentiation protocol and 150K cells/cm2 for cells to be O4 sorted due to the shorter culture time. Data are represented as the mean of 2 technical replicates. Scale bar 100 µm.

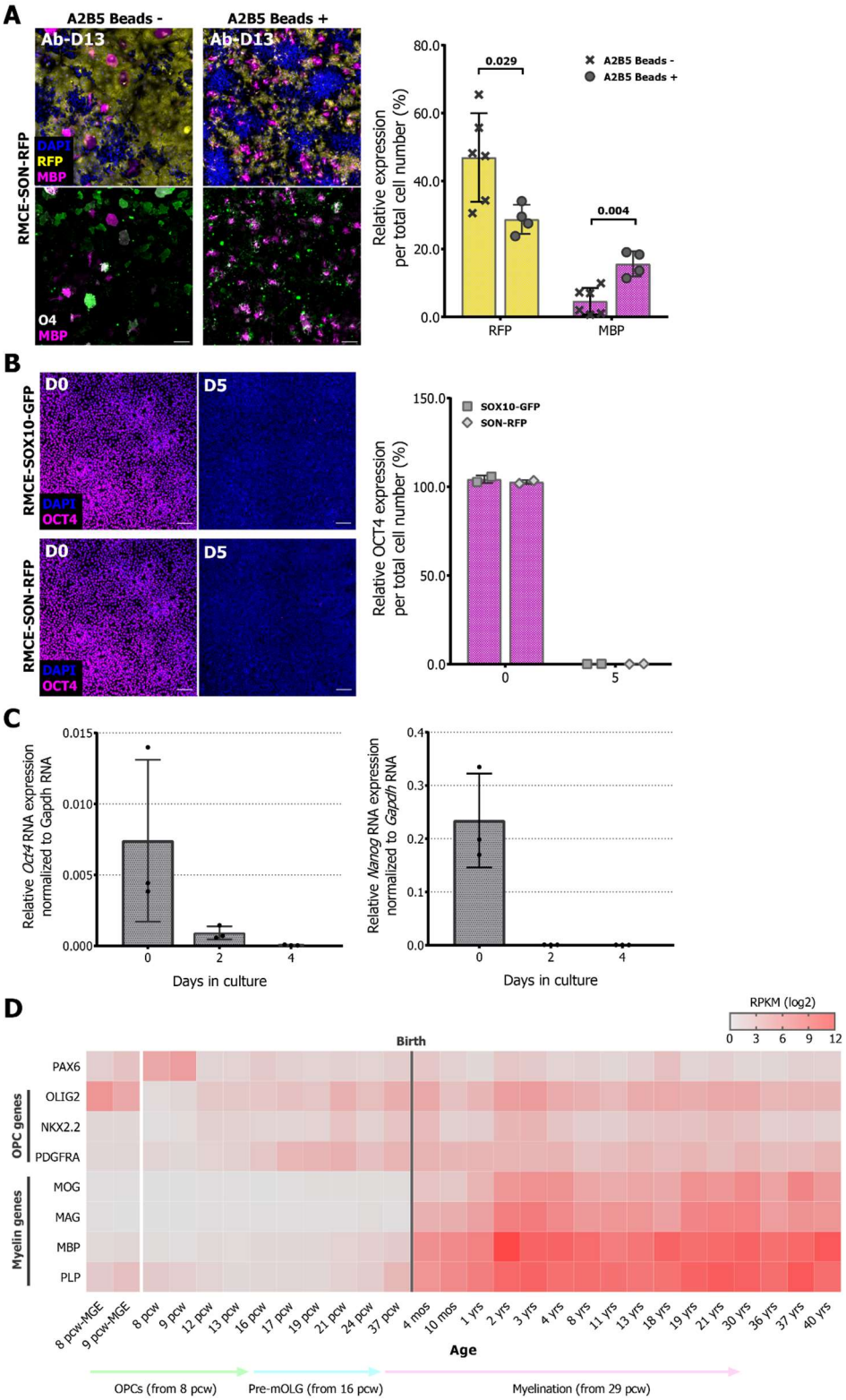

Fig Sup4 - iPCS lose its pluripotency capacity and differentiate into A2B5+ iOLGs. (A) Representative immunostaining and quantification of the A2B5- (left) and A2B5+ (right) SON-RFP cells obtained after sorting. A2B5+ sorting did not decrease sample heterogeneity as shown by the high levels of RFP+ cells (RFP, yellow) in the beads - fraction (cross) compared to the beads + fraction (circle). Even though A2B5+ SON-RFP cells express significantly more MBP+ (pink), the cells show an immature and highly ramified morphology. On the other hand, the A2B5- fraction cells appear more developed with O4+ (green) myelin-like sheaths. Data are represented as mean ± SD of 6 and 4 technical replicates for the A2B5- and A2B5+ fractions, respectively. Multiple t-test statistical analysis between cell lines for each marker and corrected

for multiple comparisons with Holm-Sidak method. Scale bar 100 µm. **(B)** Representative immunostaining and quantification of the expression of the pluripotency marker OCT4 (pink) in SOX10-GFP and SON-RFP cells cultured at day 0 and day 5. Data are represented as the mean ± SD of 2 independent experiments. Multiple t-test statistical analysis between cell lines for each marker and corrected for multiple comparisons with Holm-Sidak method. Scale bar 100 µm. **(C)** OCT4 (left) and NANOG (right) RT-qPCR analysis at day 0, 2 and 4 of the SON-iOLG differentiation protocol. As expected, the pluripotency markers are quickly downregulated after initiating neuronal lineage induction. Expression levels are normalised to GAPDH, with a cut-off of 33 cycles. Data are represented as the mean of 3 independent experiments. **(D)** Heatmap representing the normalised gene level RNA-Seq expression data in RPKM (Reads Per Kilobase of exon model per Million mapped reads) of the marker genes on the medial ganglionic eminences (MGE) and the dorsolateral prefrontal cortex throughout human development. Values were colour coded as shown on top. Data source: https://www.brainspan.org/.

Table Sup1 - Genotyping primer and probe sequences.

Assay	Primer	Sequence	Conditions
Gibson Assembly Oligo stitching	SON-TetON-GA-F	CAG AGC TCG TTT AGT GAA CCG TCA GAT CGC TGC CAC CAT GGC GGA GGA GCA GGA CCT ATC	
Gibson Assembly Oligo stitching	SON-TetON-GA-R	CTC CTT CCG TGT TTC AGT TAG CCT CCC CCA TTA CTT GTA CAG CTC GTC CAT GCC GTA CAG GAA CAG GTG G	
MCL genotype 5' end	5JA-MCL-F-LOrdovas 5JA-MCL-R-LOrdovas	CAC TTT GAG CTC TAC TGG CTT C CGT TAC TAT GGG AAC ATA CGT CA	Tm = 58.3^{o}C Size = 1.130bp
MCL genotype 3' end	AAVS1-3'-F1 DP AAVS1-3'-R3 LP	CGA ATA AAG ACC GAC CAA GC CCA AGG ACT CAA ACC CAG AA	Tm = 58.3^{o}C Size = 939bp
MCL genotype WT locus	WT-AAVS1-F-LOrdovas WT-AAVS1-R-LOrdovas	TTC GGG TCA CCT CTC ACT CC GGC TCC ATC GTA AGC AAA CC	Tm = 57^{o}C Size = 470bp
RMCE genotype 3' end	3JA-TetON-F-JGLeon WT-AAVS1-R-LOrdovas	ACCTTGATATGCTGCCTGCT GGC TCC ATC GTA AGC AAA CC	Tm = 66.7^{o}C Size = 593bp
RMCE genotype SON-RFP	Son plasmid_sox10-2_F Son plasmid_2833_R	ATC AGC CCT CAG GAC CCT AT CGA TGT TGA GGT CGT GCA T	Tm = 65.9^{o}C Size = 634bp
RMCE genotype SOX10-GFP	Son plasmid_sox10-2_F Sox plasmid_2514_R	ATC AGC CCT CAG GAC CCT AT GGT CTT GTA GTT GCC GTC GT	Tm = 65.9^{o}C Size = 764bp
GFP-HygTK: Genotyping qPCR	pZ-F3-CAGGS-GPHT FW pZ-F3-CAGGS-GPHT RE	GAG CTG TAC AAG GGT GGT G CAT ACG CGT GAA TCC TGG T	
GFP-HygTK: Genotyping qPCR probe	pZ-F3-CAGGS-GPHT PR	56-FAM/AAG CTG GTG/ZEN/ACG TTG AGG/3IABkFQ	

BCL2L1: Genotyping qPCR	BCL2L1 CNV assay F BCL2L1 CNV assay R	GGT GGT TGA CTT TCT CTC CTA C TCT CCG ATT CAG TCC CTT CT	
BCL2L1: Genotyping qPCR probe	BCL2L1 CNV assay P	56-FAM/TGT GGA AG A/ZEN/GAA CAG GAC TGA GGC/3IABkFQ	

Table Sup2 - N2B27 Media composition for iPSC-derived OLGs.

Reagent	Company	Cat. No	Concentration
DMEM F12	ThermoFischer Scientific	11320-074	
N2 supplement	ThermoFischer Scientific	17502048	1:100
B27 without Vit A	ThermoFischer Scientific	12587-010	1:50
Penicillin-streptomycin	ThermoFischer Scientific	15140-122	1:100
Glutamax	ThermoFischer Scientific	35050	1:100
Non-essential aminoacids	ThermoFischer Scientific	11140-050	1:100
2-Mercaptoethanol	ThermoFischer Scientific	21985-023	1:1000
Insulin	Merck	10516	25 µg/mL
Supplements:			
SB431542	Selleck Chemical	S1067	10 µM
LDN193189	Selleck Chemical	S2618	0.25 µM
Retinoic acid	Merck	R2625	100 nM
Smoothened Agonist	Selleck Chemical	S7779	1 µM

Table Sup3 - Oligodendrocyte differentiation medium.

Reagent	Company	Cat. No	Concentration
N2B27 medium	-	-	
Oligodendrocyte factors:			
cAMP	Merck	A9501	1 µM
NT3	Peprotech	450-03	10 ng/mL
IGF-1	Peprotech	100-11	10 ng/mL
PDGFAA	Peprotech	100-13A	10 ng/mL
HGF	Prepotech	100-39H	5 ng/mL
Biotin	Merck	B4639	100 ng/mL
T3	Merck	T6397	60 ng/mL
Doxycycline	Merck	D9891	2 µg/mL

Table Sup4 - Primers for RT-qPCR.

Gene	Primers	Sequence
GAPDH	LP-GAPDH-GL-F1 LP-GAPDH-GL-R1	TCA AGA AGG TGG TGA AGC AGG ACC AGG AAA TGA GCT TGA CAA A
GFAP	LP-GFAP-MR-F1 LP-GFAP-MR-R1	GGC AAA AGC ACC AAA GAC GG GGC GGC GTT CCA TTT ACA AT
MAG	LP-MAG-PM-F1	CAG AAG ACG TCC CCA ACT CA

	LP-MAG-PM-R1	CCT CGG GAG GCT GAA ATC ATA A
MBP	LP-MBP-PM-F1 LP-MBP-PM-R1	TGG TGA TGG AGA TGT CAA GCA GGT GCT GTG GTT TGG AAA CGA GGT TGT
MKI67	LP-MKI67-MR-F1 LP-MKI67-MR-R1	TCC TTT GGT GGG CAC CTA AGA CCT G TGA TGG TTG AGG CTG TTC CTT GAT G
MOG	LP-MOG-PM-F1 LP-MOG-PM-R1	AGA GAT AGA GAA TCT CCA CCG GA TGA TCA AGG CAA CCA AGG GTC
NANOG	LP-NANOG-PM-F1 LP-NANOG-PM-R1	AGC AGA TGC AAG AAC TCT CCA A TGA GGC CTT CTG CGT CAC AC
NKX2.2	LP-Nkx2.2-PM-F1 LP-Nkx2.2-PM-R1	GCT TCC TGC GTC CAT TTC CG GAA AGA AAC TGG GGA TGG GGA G
OCT4	LP-OCT4-RG-F1 LP-OCT4-RG-R1	GTG TTC AGC CAA AAG ACC ATC T GGC CTG CAT GAG GGT TTC T
OLIG2	LP-Olig2-PM-F1 LP-Olig2-PM-R1	ATC GCA TCC AGA TTT TCG G CCC CAG GGG AAG ATA GTC GT
PAX6	LP-Pax6-PM-F1 LP-Pax6-PM-R1	CGA GAT TTC AGA GCC CCA TA AAG ACA CCA CCG AGC TGA TT
PDGFRA	LP-PDGFa-PM-F1 LP-PDGFa-PM-R1	AGG GAT AGC TTC CTG AGC CA AGC TCC GTG TGC TTT CAT CA
PLP1	LP-PLP-PM-F1 LP-PLP-PM-R1	AAC AGC TGA GTT CCA AAT GAC C ACG GCA AAG TTG TAA GTG GC
SOX10	LP-Sox10-RG-F1 LP-Sox10-RG-R1	CCT CAC AGA TCG CCT ACA CC CAT ATA GGA GAA GGC CGA GTA GA
SYP	LP-SYP-PM-F1 LP-SYP-PM-R1	ACC TCG GGA CTC AAC ACC TCG G GAA CCA CAG GTT GCC GAC CCA G

Table Sup5 - Neural maintenance medium (NM)

Reagent	Company	Cat. No	Concentration
Neurobasal	ThermoFischer Scientific	21103-049	50%
DMEM/F-12	ThermoFischer Scientific	11320-074	50%
N2	ThermoFischer Scientific	17502048	1:200
B27	ThermoFischer Scientific	17504044	1:50
Penicillin-streptomycin	ThermoFischer Scientific	15140-122	1:100
Glutamax	ThermoFischer Scientific	35050	1:100
Non-essential aminoacids	ThermoFischer Scientific	11140-050	1:100
2-Mercaptoethanol	ThermoFischer Scientific	21985-023	1:1000
Insulin	Merck	10516	2.5 µg/mL
Supplements (NI medium):			
SB431542	Selleck Chemical	S1067	10 µM
LDN193189	Selleck Chemical	S2618	0.25 µM

Table Sup6 - Essential 6 media (E6)

Reagent	Company	Cat. No	Concentration
DMEM F12	ThermoFischer Scientific	11320-074	
Insulin-Transferrin-Selenium	ThermoFischer Scientific	17502048	1:100
L-ascorbic-acid-2-phosphate	Merck	A8960	64 µg/ml
HEPES	Merck	H3375	15 mM

Table Sup7 - Glial precursor expansion medium (GPE)

Reagent	Company	Cat. No	Concentration
DMEM F12	ThermoFischer Scientific	11320-074	
N2	ThermoFischer Scientific	17502048	1:100
B27 without Vit A	ThermoFischer Scientific	12587-010	1:50
Penicillin-streptomycin	ThermoFischer Scientific	15140-122	1:100
Glutamax	ThermoFischer Scientific	35050	1:100
bFGF	StemCell Technologies	78003.2	10 ng/ml
Recombinant Human EGFR	Peprotech	100-15	10 ng/ml

Table Sup8 - Astrocyte induction medium (AIM)

Reagent	Company	Cat. No	Concentration
DMEM F12	ThermoFischer Scientific	11320-074	
N2	ThermoFischer Scientific	17502048	1:100
B27 without Vit A	ThermoFischer Scientific	12587-010	1:50
Penicillin-streptomycin	ThermoFischer Scientific	15140-122	1:100
Glutamax	ThermoFischer Scientific	35050	1:100
Recombinant Human LIF	Peprotech	300-05	10 ng/ml
Recombinant Human EGFR	Peprotech	100-15	10 ng/ml

Table Sup9 - Astrocyte medium (AM)

Reagent	Company	Cat. No	Concentration
DMEM F12	ThermoFischer Scientific	11320-074	
B27	ThermoFischer Scientific	17504044	1:50
Penicillin-streptomycin	ThermoFischer Scientific	15140-122	1:100
Glutamax	ThermoFischer Scientific	35050	1:100

Table Sup10 - Microglia differentiation medium (DM1)

Reagent	Company	Cat. No	Concentration
DMEM F12	ThermoFischer Scientific	11320-074	
N2	ThermoFischer Scientific	17502048	1:100
B27 without Vit A	ThermoFischer Scientific	12587-010	1:50
Penicillin-streptomycin	ThermoFischer Scientific	15140-122	1:100
Glutamax	ThermoFischer Scientific	35050	1:100
Non-essential aminoacids	ThermoFischer Scientific	11140-050	1:100
2-Mercaptoethanol	ThermoFischer Scientific	21985-023	1:1000

Insulin	Merck	10516	5 µg/mL
Insulin-Transferrin-Selenium	ThermoFischer Scientific	17502048	1:100
Monothioglycerol	Merck	M1753	
Microglia factors:			
Recombinant Human IL-34	Peprotech	200-34	100 ng/ml
Animal-Free Recombinant Human TGF-β1	Peprotech	AF-100-21C	50 ng/ml
Recombinant Human M-CSF	Peprotech	300-25	25 ng/ml

Table Sup11 - NB+/B27+ medium.

Reagent	Company	Cat. No	Concentration
Neurobasal Plus	ThermoFischer Scientific	A3582901	
B27 Plus	ThermoFischer Scientific	A3582801	1:50
Penicillin-streptomycin	ThermoFischer Scientific	15140-122	1:100
Glutamax	ThermoFischer Scientific	35050	1:100

Project 2: Characterisation of *Fth1* mRNA granules in oligodendrocytes

The current chapter includes the research article "Characterisation of Fth1 mRNA granules in oligodendrocytes". This article reports a characterization study of the *Fth1* mRNA dynamics in oligodendrocytes.

Contributions:
Liliana D. Pedro, Stephan A. Müller, Dominik Paquet, Stefan F. Lichtenthaler and Mikael Simons

The author of this thesis is the first author of this manuscript. LDP and MS designed the approach. SAM and SFL analysed the proteomic profile of selected mRNAs by mass spectrometry and performed the subsequent bioinformatic analysis. DP provided essential technical support for the development of human oligodendrocytes from induced pluripotent stem cells. LP collected the data, analysed the data and performed statistical analysis and data visualization. LP wrote the manuscript.

Characterisation of *Fth1* mRNA granules in oligodendrocytes

Liliana D. Pedro[1,2,3], Stephan A. Müller[2,4], Dominik Paquet[5,6], Stefan F. Lichtenthaler[2,4,5] and Mikael Simons[*1,2,5,7]

[1]Institute of Neuronal Cell Biology, Technical University Munich, 80802 Munich, Germany
[2]German Center for Neurodegenerative Diseases (DZNE), 81377 Munich, Germany
[3]Graduate School of Systemic Neuroscience (GSN), 82152 Planegg, Germany
[4]Neuroproteomics, Klinikum Rechts der Isar Technical University of Munich, 81675 Munich, Germany
[5]Munich Cluster of Systems Neurology (SyNergy), 81377 Munich, Germany
[6]Institute for Stroke and Dementia Research (ISD), 81377 Munich, Germany
[7]Max Planck Institute of Experimental Medicine (MPI-EM), 37075 Goettingen, Germany
*Correspondence: mikael.simons@dzne.de (MS)

Dysregulation of iron homeostasis can lead to the production of lethal reactive oxygen species, lipid peroxidation and ultimately cell death. Upon neuronal iron-mediated cytotoxicity, oligodendrocytes secrete ferritin heavy chain protein (FTH1), which can potentially be internalised by neighbouring neurons. The FTH1 protein will then protect the neurons by storing and detoxifying excess intracellular iron. Given the importance of FTH1 protein for neuronal protection against iron-mediated cytotoxicity it is reasonable to expect that targeted transport and local translation of *Fth1* mRNA could effectively provide a way for oligodendrocytes to rapidly respond to external stimuli. Here, we show that *Fth1* mRNA content increased throughout oligodendrocyte differentiation in both mouse and human oligodendrocytes. Similar to other locally repressed mRNAs, such as *Mbp* and *Mobp, Fth1* mRNA showed a granular cytoplasmic expression pattern associated with RNA granules *in vitro* and *in vivo*. Moreover, *Fth1* mRNA is not associated with P-bodies or stress granules markers in mature oligodendrocytes, suggesting a unique mechanism of translational repression for the *Fth1* mRNA at the distal processes. We further developed a proteomics approach to selectively isolate native RNA-protein complexes, and identify potential interacting proteins involved in the transport and translational repression of *Fth1* mRNA in mature oligodendrocytes. Using this approach, we identified 19 potential protein candidates that could be associated with *Fth1* mRNA translocation and/or translation repression in oligodendrocytes. Our study provides the foundation for additional insights into the function of *Fth1* mRNA granules and associated proteins in oligodendrocytes

Introduction

Oligodendrocytes (OLGs) are well known as the myelin producing cells of the central nervous system (CNS). OLGs promote fast saltatory nerve conduction by electrically insulating axons and establishing axonal domains (Stadelmann et al. 2019). Iron has been implicated in oligodendrocyte development and myelination, as iron is a necessary co-factor for several enzymes involved not only in oligodendrocyte proliferation and differentiation, but also myelin lipid synthesis. In fact, conditional knockout in mouse oligodendrocytes of ferritin heavy chain (FTH1), an iron storage protein, during early postnatal development leads to hypomyelination. However, depletion of FTH1 protein after postnatal day 60 (when

developmental myelination is complete) had no effect on oligodendrocyte numbers or myelin thickness, but it led to axonal degeneration and a significant reduction of neuronal cells (Wan et al. 2020; Mukherjee et al. 2020). Suggesting that FTH1 protein may have a role not only in oligodendrocyte development, but also in axonal support and long-term integrity. Indeed, FTH1 protein is secreted from oligodendrocytes and was shown to protect neurons against iron-mediated cytotoxicity (Mukherjee et al. 2020).

Fth1 mRNA in oligodendrocytes is among the three most abundant transcripts (*Mbp*, *Mopb*, and *Fth1*) found in purified myelin, when compared to total brain lysates and myelinating oligodendrocytes (mOLGs) (Thakurela et al. 2016; Gould et al. 2000). Moreover, *Fth1* mRNA levels are increased in the myelin fractions of adult mice (P75 vs juvenile P20). Conversely, relatively small amounts of FTH1 protein can be found in myelin when compared to brain lysates of adult mice (Mukherjee et al. 2020). Interestingly, a longer *Fth1* mRNA isoform associated with the presence of a 3' untranslated region (UTR) is enriched in myelin (Gould et al. 2000). The cytoplasmic regulation of translation by 3'UTR is of increasing interest as these sequences can not only affect message stability, but also message localization and translation (Moujaber and Stochaj 2018). This particular transcript also shows high expression levels in non-neuronal cells of the adult hippocampus when compared to the fetal brain (Percy et al. 1998), suggesting that different *Fth1* RNA isoforms might have different functional roles and as such different regulatory pathways. The presence of high levels of *Fth1* mRNA with an extended 3'UTR region in the myelin sheath may suggest a mechanism for the active transport of this transcript. Targeted transport and local translation of *Fth1* mRNA could effectively provide a way to for OLGs to rapidly respond to external stimuli, as a single mRNA can give rise to multiple copies of a protein, which is particularly effective for cells with distinct membrane domains separated by large distances.

Despite recent research efforts, many aspects governing the RNA dynamics of localising mRNAs in the brain remain unknown. In oligodendrocytes, most research has centred on *Mbp* and *Mobp* mRNAs and little is known about the potential for active transport or local translation of *Fth1* mRNA in myelin. In this study, we present data showing that *Fth1* mRNA has a granular cytoplasmic expression pattern, similar to *Mbp* and *Mobp* mRNA. The subcellular localization of *Fth1* mRNA and the lack of association with other known cytoplasmic RNA granule markers could indicate a new mechanism of translational repression for the *Fth1* mRNA at the distal OLG processes. We further developed a proteomics approach to selectively isolate native RNA-protein complexes, and identify potential *Fth1* mRNA interacting proteins. Future studies are required to characterize the RNA binding proteins and associated RNA binding sequences involved in the transport and translational repression of *Fth1* mRNA in mature oligodendrocytes.

Results

***Mbp* mRNA and *Fth1* mRNA show a granular distribution in oligodendrocyte processes.** Previous work has shown that *Fth1* mRNA is highly expressed in purified myelin fractions when compared to brain lysates. In order to better understand the translational regulation of FTH1 protein, we analysed *Fth1* mRNA and protein levels in differentiating mouse primary OLGs and human iPSC-derived oligodendrocytes (OLG and iOLG, respectively). We isolated and further cultured mouse oligodendrocyte precursors cells (OPCs) expressing PDGFRA, from postnatal day 7 (P7) mice, and early human pre-myelinating iOLGs expressing the O4 antigen. Cells were staged based on cellular morphology and MBP expression.

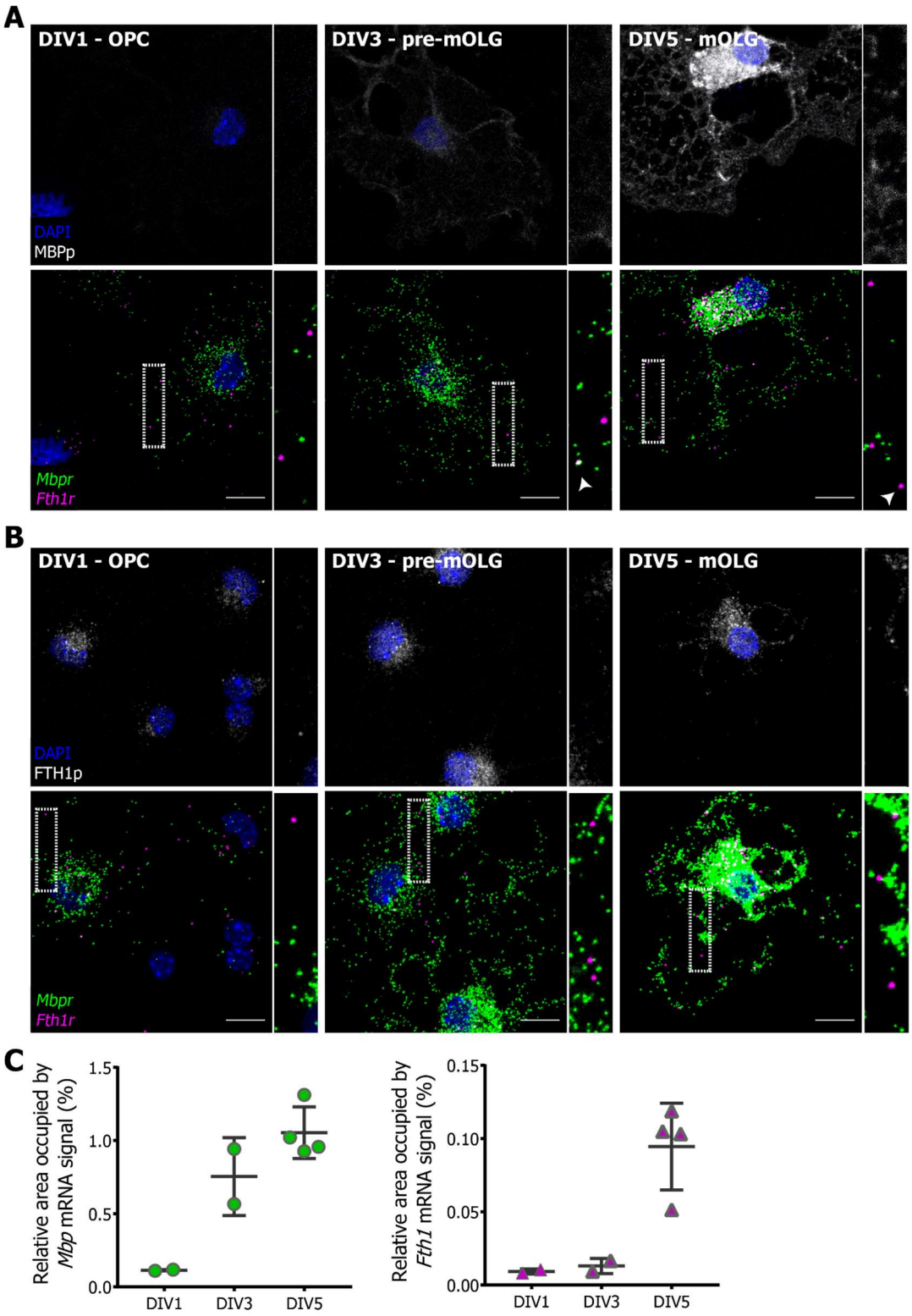

Fig 1 - *Fth1* mRNA is expressed as cytoplasmic puncta, similar to *Mbp* mRNA, in primary mouse oligodendrocytes. (A and B) Representative images of the *in situ* hybridization of *Mbp* (green) and *Fth1* (pink) mRNA coupled with MBP (A) or FTH1 (B) protein (white) staining in primary mouse oligodendrocytes at the 3 main stages of development: OPCs at day *in vitro* (DIV) 1, pre-myelinating oligodendrocytes (pre-mOLGs) at DIV3 and mOLGs at DIV5. Throughout differentiation the cells exhibit an increasing amount of cytoplasmic RNA granules along the cell processes and myelin membranes. Boxes in white represent high-magnification insets. White arrowheads (A) call attention to Fth1 RNA granules at the edge of the myelin membrane. Scale bar 10 μm. **(C)** Quantification of the relative area occupied by the signal

of the fluorescent probes against *Mbp* (left) and *Fth1* (right) mRNA in the processes and myelin of primary mouse oligodendrocyte throughout differentiation. Data are represented as mean ± SD of 2 to 4 biological replicates as a minimum average of 8 fields of view.

The distribution of endogenous *Fth1* mRNA was analysed by *in situ* hybridization (ISH) coupled with protein immunostaining. *Mbp* mRNA and *Plp1* mRNA were used as controls for the validation of the *in situ* hybridization method. Similar to previous reports, *Mbp* mRNA is highly expressed in the soma and processes of differentiated oligodendrocytes (Fig 1A, OLG DIV5 and Fig 2A, iOLG DIV24) (Barbarese et al. 1995), while *Plp1* mRNA is restricted to the cell body (Fig Sup1C) (Baron et al. 1993), illustrating the specificity of the mRNA probes signal and the lack of cross-reactivity between these probes. We confirmed that the antigenicity of the high expressing MBP protein was not considerably affected by the *in situ* hybridization procedure, as judged by the similar signal abundance and distribution of MBP protein immunostaining in DIV3 and 5 oligodendrocytes treated with and without *in situ* hybridization procedure (Fig 1A vs Fig Sup1A). Unfortunately, proteins expressed at low amounts, such as FTH1, were somewhat affected by the *in situ* hybridization procedure as observed by the reduced staining within the OLG main processes after *in situ* hybridization.

As expected, the levels of *Mbp* mRNA and MBP protein increased throughout oligodendrocyte differentiation in both mouse and human oligodendrocytes (Fig 1C and Fig2A). *Mbp* mRNA showed the characteristic granular distribution along the distal processes, associated with ribonucleoprotein (RNP) cytosolic transport. Moreover, low levels of *Mbp* mRNA cytosolic puncta are detected at the OPC stage (DIV1), even though no MBP protein is observed (Fig 1A and Fig2A), suggesting that *Mbp* mRNA is translationally repressed during the initial phase of OLG differentiation (Schäfer et al. 2016). Interestingly, while FTH1 protein signal was mainly found in the cell body and main processes, *Fth1* mRNA showed a granular pattern in both the oligodendrocyte cytoplasm and myelin edge, similar to *Mbp* mRNA, albeit at lower amounts (Fig 1B, C and Fig2B). The limited co-occurrence between *Fth1* mRNA and FTH1 protein in oligodendrocyte myelin could result from a reduction in the antibody sensitivity (Fig Sup1A) or some level of local translation repression. In contrast to the *Mbp* mRNA expression levels, that gradually increase in the OLG processes as the cells mature, *Fth1* mRNA shows the highest expression once the cells have terminally differentiated into myelinating cells (Fig 1C), further supporting previous observations that FTH1 protein may have a role after myelination is complete. Similar patterns between *Mbp* and *Fth1* mRNA puncta were observed in mice primary cultures and human myelinating oligodendrocytes. Suggesting that human OLGs derived from iPSCs could provide a scalable, renewable and easier to gene edit source of cells that can facilitate RNA granules research. Taken together, the data shows that *Fth1* mRNA has a granular distribution along the processes of mature oligodendrocytes reminiscent of other locally repressed mRNAs.

***Mbp* mRNA and *Fth1* mRNA do not colocalize in the same RNP granule.** We further analysed the spatial relationships of *Mbp*, *Mobp* and *Fth1* mRNAs in myelinating oligodendrocytes *in vitro* and *in vivo*.

Pearson's correlation coefficient (PCC) and Mander's correlation coefficient (MCC) were used to quantify the degree of colocalization between fluorophores. Differences between MCC and PCC values are associated with the image elements used to calculate both metrics. MCC strictly measures co-occurrence independent of signal proportionality, but it is affected by signal intensities; while PCC measures the overall association of two

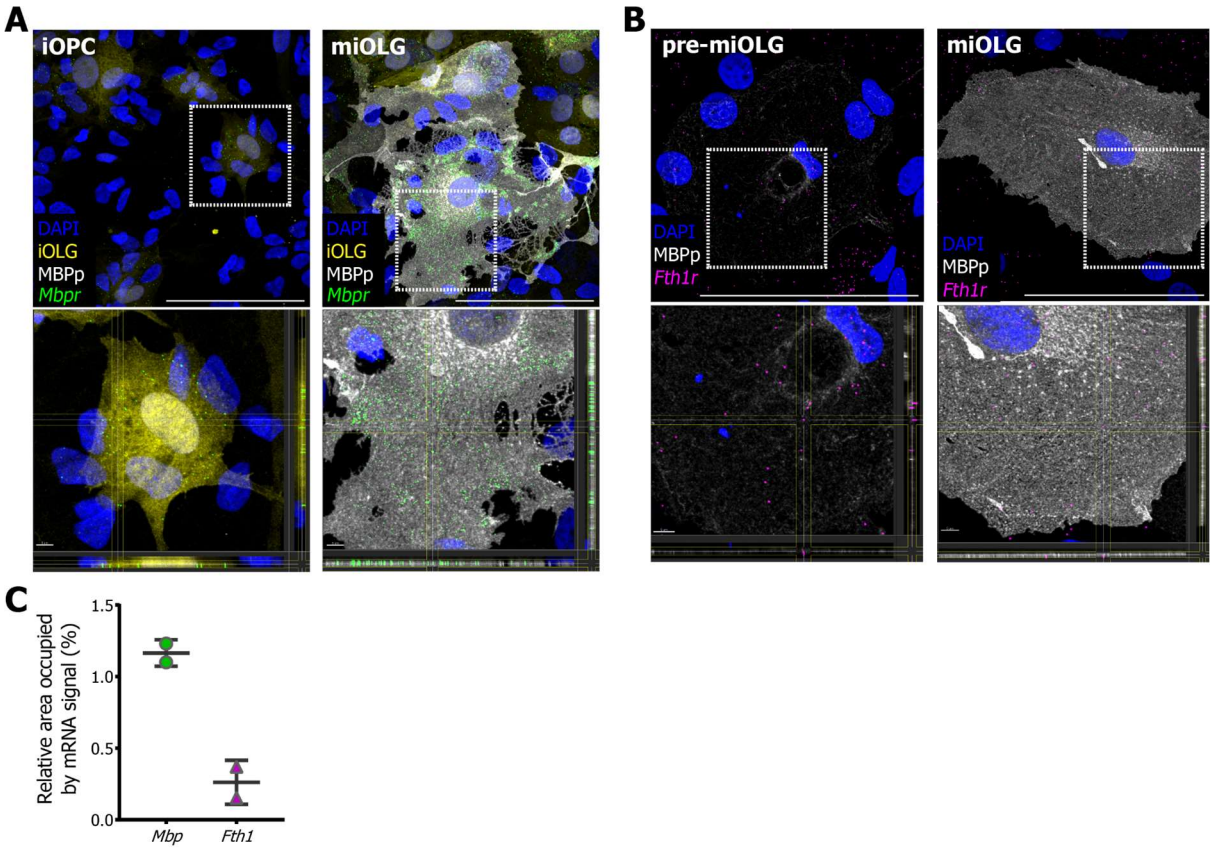

Fig 2 - *Mbp* and *Fth1* mRNA is expressed as cytoplasmic puncta in human iPSC derived oligodendrocytes (iOLG). (A and B) Representative images of the *in situ* hybridization of *Mbp* (A, green) and *Fth1* (B, pink) mRNA coupled with MBP protein (white) staining in human iPSC derived oligodendrocytes at the 3 main stages of development: OPCs, pre-mOLGs and mOLGs. iOLGs express an RFP cytosolic marker (A, iOLG, yellow). Throughout differentiation the cells exhibit cytoplasmic RNA granules along the cell cytoplasm and myelin membranes. Boxes in white represent high-magnification insets with orthogonal projections of cytoplasmic puncta, revealing that the RNA is within the RFP+ or MBP+ cell. Scale bar 10 µm. **(C)** Quantification of the relative area occupied by the signal of the fluorescent probes against *Mbp* (green) and *Fth1* (pink) mRNA in mOLG. Data are represented as mean ± SD of 2 biological replicates as a minimum average of 4 fields of view.

probes, but it can be impacted if they co-occur in different proportions (Dunn et al. 2011). In our experimental setting intensity differences were observed between probes associated with different fluorophores, and *Mbp* mRNA and *Fth1* mRNA showed a ±10-fold expression level difference (Fig 1C). Meaning that both these approaches have disadvantages when applied to our system, as such we used a combination of both measures, together with linescans and pixel scatter plots to validate our findings.

To determine the inherent colocalization error associated with dual-fluorophore *in situ* hybridization labelling in the same granule, we targeted the same *Mbp* mRNA transcript region with two distinct fluorescent mRNA probes (Mbpr-488, Mbpr-546). Our results show that spatially associated RNAs display an estimated co-localization of ±19% (0.19±0.03) and ±32% (0.32±0.06) (Fig Sup1B). Previous data showed co-localization rates between 11% to 29% when using mRNA probes targeting the same transcript regions, and between 35% to 56% co-localization rates in non-overlapping probes (Mikl et al. 2011). Suggesting that the lack of 100% colocalization does not result from low hybridization efficiency, but from mRNA probe binding competition due to the low mRNA molecule copy number per granule.

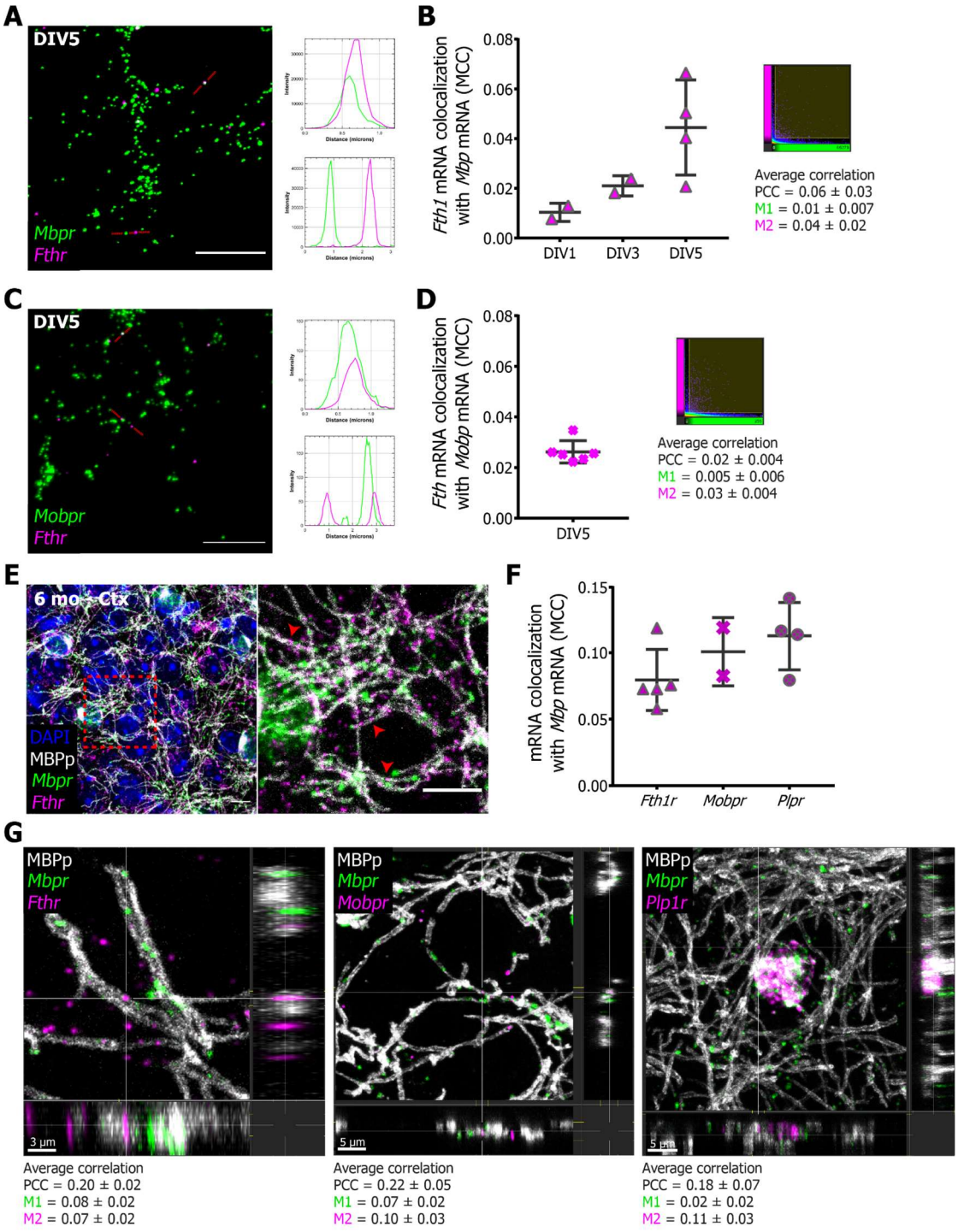

Fig 3 - *Mbp*, *Fth1* and *Mobp* mRNAs localise in distinct cytoplasmic ribonucleoprotein (RNP) granules in *in vitro* and *in vivo* mouse myelinating oligodendrocytes. (A and C) Representative images of the *in situ* hybridization of *Mbp* (A, green) or *Mobp* (C, green) mRNA and *Fth1* (pink) mRNA in the processes and myelin of primary mouse oligodendrocytes at DIV5. In rare instances did we observe signal overlap between the two RNA probes. Red dotted lines represent linescans showing the fluorescent intensity (y values) of each probe signal along the oligodendrocyte process (x values are distance in microns). Scale bar 10 µm. **(B)** Left: Graphical representation of the MCC measuring the fraction of total *Fth1* RNA probe (pink) fluorescence that colocalizes with the fluorescence of the *Mbp* RNA probe (green) in mouse oligodendrocytes at the 3 main differentiation stages. Right, top: Representative frequency scatter plot of the fluorescence intensity in the green (*Mbp*, green, x values) and pink (*Fth1*, pink, y values) channels at DIV5. Individual dots in the scatter plot correspond to single pixels of the original picture. The colour code

highlights the frequency of dots present in a certain region of the scatter plot (from blue to yellow and red with increasing frequencies). Right, bottom: Average values of the colocalization analysis based on PCC and MCC values at DIV5. The value for PCC ranges from +1 (total positive correlation), 0 (no correlation) and −1 (total negative correlation). The values for MCC occurrence are represented by M1 (green) the fraction of *Mbp* RNA puncta in areas containing *Fth1* RNA and M2 (pink) the fraction of *Fth1* RNA puncta in areas containing *Mbp* RNA. Data are represented as mean ± SD of 2 to 4 biological replicates as a minimum average of 8 fields of view. **(D)** Left: Graphical representation of the MCC measuring the fraction of total *Fth1* RNA probe (pink) fluorescence that colocalizes with *Mobp* RNA probe (green) in myelinating oligodendrocytes at DIV5. Right, top: Representative frequency scatter plot of the fluorescence intensity in the green (*Mobp*, green, x values) and pink (*Fth1*, pink, y values) channels. Right, bottom: Average values of the co-localization analysis based on the PCC and MCC values. The values for MCC occurrence are represented by M1 (green) the fraction of *Mobp* RNA puncta in areas containing *Fth1* RNA and M2 (pink) the fraction of *Fth1* RNA puncta in areas containing *Mobp* RNA. Data are represented as mean ± SD of 2 to 6 biological replicates as a minimum average of 5 fields of view. **(E)** Representative images of the *in situ* hybridization of *Mbp* (green) and *Fth1* (pink) mRNA coupled with MBP protein (white) staining in 6 month old mouse cortex (6mo-Ctx). Similar to *in vitro* data, *Fth1* RNA expression co-localizes with the myelin tracts, showing a cytoplasmic puncta pattern associated with RNP granules. Boxes in red represent high-magnification inset on the left. Red arrowheads call attention to *Fth1* RNA granules co-localizing within the myelin tracts. Scale bar 10 µm. **(F)** Graphical representation of the MCC measuring the fraction of total *Fth1*, *Mobp* and *Plp1* RNA probe (pink) fluorescence that colocalizes with *Mbp* RNA (green) probe in the 6-month-old mouse cortex. Data are represented as mean ± SD of 2 to 5 biological replicates as a minimum average of 3 fields of view. **(G)** Representative images of orthogonal projections of cytoplasmic RNA puncta within MBP+ myelin tracts. RNA is detected by the *in situ* hybridization of *Mbp* RNA (green) with *Fth1* (left, pink), *Mobp* (middle, pink) or *Plp1* (right, pink) RNA coupled with MBP protein (white) staining. Localising *Mbp* and *Mobp* mRNA puncta appear to not co-localize. Similarly, *Fth1* RNA shows the characteristics of RNP granules within myelin tracts. *Plp1* RNA is not a locasing mRNA and shows a distribution mainly restricted to the cell body (as detected by nuclear staining, DAPI). The values for MCC occurrence are represented by M1 (green) the fraction of *Mbp* RNA puncta in areas containing *Fth1*, *Mobp* or *Plp1* RNA and M2 (pink) the fraction of *Fth1*, *Mobp* or *Plp1* RNA puncta in areas containing *Mbp* RNA. Scale bars 3 µm and 5 µm.

In *in vitro* myelinating oligodendrocytes, neither *Fth1* and *Mbp* mRNA, nor *Fth1* and *Mobp* mRNA puncta co-localize (Fig 3A-D, Fth1-Mbp: 0.04±0.02, Fth1-Mobp: 0.026±0.004) suggesting that, in oligodendrocytes granules *Mbp*, *Mobp* and *Fth1* mRNAs are not present in multi complexes containing different RNA molecules. Likewise, in the cortex of adult mice (6 months) *Mbp* and *Mobp*, which share A2RE localising sequences, were present in distinct populations (Fig 3G, Mbp-Mobp: 0.10±0.03). Similarly, *Mbp* and *Fth1* mRNA signals do not overlap (Fig 3E and G, Fth1-Mbp: 0.07±0.02). As observed for the primary cell cultures *Mbp*, *Mobp* and *Fth1* mRNA show a granular pattern within the cortical myelin tracts, while *Plp1* mRNA is restricted to the perinuclear region (Fig 3G). Our data indicate that oligodendrocyte mRNAs *in vitro* and *in vivo* do not colocalize in the same RNP granule, which might allow for their differential regulation and selective delivery, thus contributing to signal specific modifications and plasticity at the RNA level.

***Fth1* mRNA is not part of stress granules or P-bodies, suggesting a new type of RNP.** The presence of cytosolic RNA puncta can be associated with different types of RNP complexes that support the preservation of cell homeostasis under normal and stress conditions. Cytoplasmic RNA granules differ markedly in size and composition and are mainly involved in RNA quality control and metabolism (Tian et al. 2020). Some granules, such as processing bodies (P-bodies) and stress granules (SGs) can be found in many cell types. Other RNA granules are cell-type-

specific, such as *Mbp* mRNA or neuronal RNA granules showing a dynamic distribution that often relies on interactions with the cytoskeleton. To further investigate the nature of *Fth1* mRNA granules in oligodendrocytes we analysed the distribution of *Fth1* mRNA in relation to known markers for P-bodies and SGs in mature oligodendrocytes.

P-bodies are characterised by a lack of ribosomal proteins and the presence of translational repressors, as well as enzymes and co-factors associated with mRNA decay, such as the mRNA-decapping enzyme 1A (DCP1A) (Hubstenberger et al. 2017). The co-localization between endogenous *Fth1* mRNA and DCP1A protein was analysed in comparison to *Mbp*, an mRNA known to not be associated with P-bodies. Comparable to the *Mbp* mRNA control, approximately ±2% of *Fth1* mRNA puncta were found to co-occur with DCP1A protein signal (0.018±0.005) (Fig 4A and B). As ribosomes are generally not present in P-bodies we next determined the colocalization between *Fth1* mRNA and the ribosomal protein S6, a component of the 40S ribosomal subunit. Both *Fth1* and *Mbp* mRNA show some level of co-localization with the ribosomal protein, ±9% (0.09±0.03) and ±16% (0.16±0.03), respectively (Fig 4C and D). Even if not significant, *Mbp* mRNA appears to co-occur more frequently with ribosomes than *Fth1* mRNA. Overall, the data suggests that *Fth1* mRNA is not associated with P-bodies in mature oligodendrocytes, which is in line with a study in HEK293 cells where a significant *Fth1* RNA depletion was detected in P-bodies sorted fractions (p=0.00001) (Hubstenberger et al. 2017).

Stress granules support cell survival during stress conditions and are characterised by quickly assembling upon stress and then rapidly dispersing after the stress source is no longer present. We analysed the *Fth1* mRNA distribution upon induction of oxidative stress by sodium arsenite (NaAs, 0.5 mM), a known SG-inducing factor. On exposure to sodium arsenite, the G3BP1 (Ras-GAP SH3 binding protein 1) protein is recruited into varying size aggregates (~0.1 to 4 μm) at the perinuclear region (Fig 4E) (Mahboubi and Stochaj 2017). If *Fth1* mRNA was associated with stress granules, upon exposure to arsenite, we would observe a depletion of the mRNA from the oligodendrocyte processes and an increase in the co-localization between the G3BP1 protein and *Fth1* mRNA in the cell body. Conversely, we observe a decreasing trend in the stochastic co-localization between *Fth1* mRNA and G3BP1, as G3BP1 assembles into SGs (Fig 4F, Ctr: 0.11±0.05; NaAs: 0.08±0.02). As expected, a similar effect was observed for *Mbp* mRNA, a known non-SG mRNA (Fig 3F, Ctr: 0.038±0.001; NaAs: 0.029±0.012). Similar to *Mbp* mRNA, *Fth1* mRNA puncta appear to be a unique type of RNA granule that is distinct from stress granules and processing bodies in oligodendrocytes.

Development of a new experimental approach to identify protein regulators of *Fth1* mRNA. Localising mRNAs transport and translation are regulated in the context of specific ribonucleoprotein complexes, determined by a combination of cis-regulatory motifs within the mRNA sequence and trans-acting proteins. In oligodendrocytes *Mbp* mRNA is well described as containing an A2RE sequence that is recognized by the HNRNPA2 protein, which is both necessary and sufficient to direct the transcript towards oligodendrocyte processes. However, the cis-acting localization elements can be very heterogenous in size and structure, and often fold into higher-order secondary structures. Because of the complexity and variability of the motifs identified to date, it is not possible to unambiguously identify cis-acting localization elements by computational prediction based on the mRNA sequence (Doyle and Kiebler 2011) (Table Sup1 and 2).

To identify interacting proteins of the *Fth1* mRNA in oligodendrocytes, we combined and optimised different RNA isolation methods for the recovery of endogenously formed

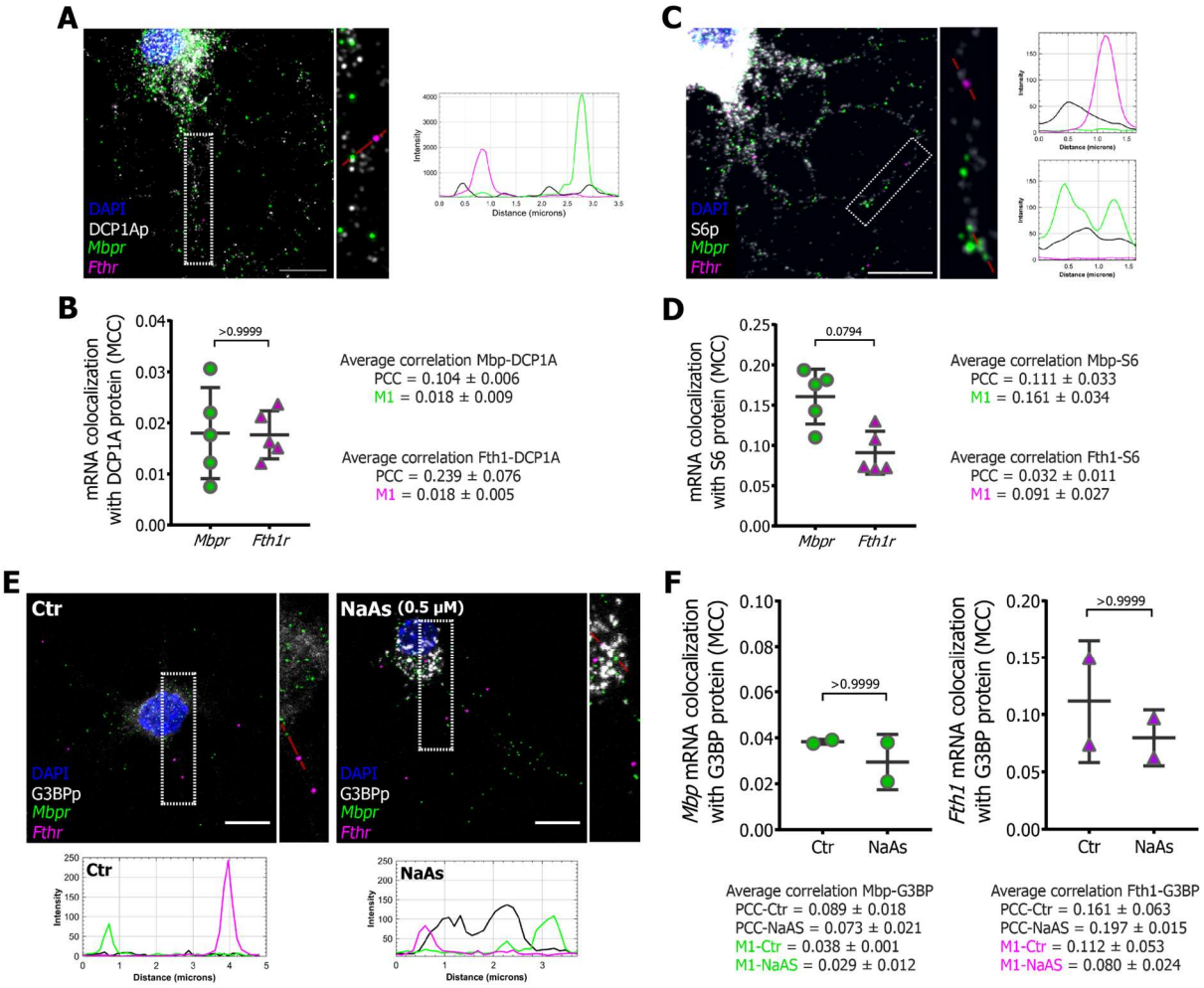

Fig 4 - *Mbp* mRNA and *Fth1* mRNA puncta are distinct from processing bodies and stress granules in primary mouse myelinating oligodendrocytes. (A) Representative images of the *in situ* hybridization of *Mbp* (green) and *Fth1* (pink) mRNA coupled with DCP1A protein (white) staining in the processes and myelin of primary mouse oligodendrocytes at DIV5. *Mbp* and *Fth1* RNA do not co-occur with the P-bodies protein marker DCP1A. Boxes in white represent high-magnification insets. Red dotted lines represent linescans (right) showing the fluorescent intensity (y values) of each probe signal along the oligodendrocyte process (x values are distance in microns). Scale bar 10 µm. **(B)** Left: Graphical representation of the MCC measuring the fraction of *Mbp* RNA puncta (green) and *Fth1* RNA puncta (pink) in compartments containing DCP1A protein at DIV5. Right: Average values of the co-localization analysis based on the PCC and MCC at DIV5. Nonparametric unpaired t-test statistical analysis between *Mbp* and *Fth1* MCC values with Kolmogorov-Smirnov method. Data are represented as mean ± SD of 5 biological replicates as a minimum average of 4 fields of view. **(C)** Representative images of the *in situ* hybridization of *Mbp* (green) and *Fth1* (pink) mRNA coupled with S6 protein (white) staining in the processes and myelin of primary mouse oligodendrocytes at DIV5. *Mbp* and *Fth1* RNA do not significantly co-occur with the ribosomal protein marker S6. However, *Fth1* RNA appears to co-occur less frequently than *Mbp* RNA. Boxes in white represent high-magnification insets. Red dotted lines represent linescans (right) showing the fluorescent intensity (y values) of each probe signal along the oligodendrocyte process (x values are distance in microns). Scale bar 10 µm. **(D)** Left: Graphical representation of the MCC measuring the fraction of *Mbp* RNA puncta (green) and *Fth1* RNA puncta (pink) in compartments containing S6 protein. Right: Average values of the colocalization analysis based on the PCC and MCC at DIV5. Nonparametric unpaired t-test statistical analysis between *Mbp* and *Fth1* MCC values with Kolmogorov-Smirnov method. Data are represented as mean ± SD of 5 biological replicates as a minimum average of 5 fields of view. **(E)** Representative images of the *in situ* hybridization of *Mbp* (green) and *Fth1* (pink) mRNA coupled with G3BP protein (white) staining in the processes and myelin of primary mouse oligodendrocytes at DIV5. *Mbp* and

Fth1 RNA do not co-occur in G3BP+ stress granules induced by oxidative stress upon NaAs treatment. Boxes in white represent high-magnification insets. Red dotted lines represent linescans (right) showing the fluorescent intensity (y values) of each probe signal along the oligodendrocyte process (x values are distance in microns). Scale bar 10 μm. **(F)** Left: Graphical representation of the MCC measuring the fraction of *Mbp* RNA puncta (green) in compartments containing G3BP protein in control and NaAs treated primary oligodendrocytes at DIV5. Average values of the colocalization analysis based on the PCC and MCC. Right: graphical representation of the MCC measuring the fraction of *Fth1* RNA puncta (pink) in compartments containing G3BP protein in control and NaAs treated oligodendrocytes at DIV5. Average values of the colocalization analysis based on the PCC and MCC. Nonparametric unpaired t-test statistical analysis between MCC values of control and NaAs treated samples with the Kolmogorov-Smirnov method. Data are represented as mean ± SD of 2 biological replicates as a minimum average of 3 fields of view.

mRNA-protein complexes (Iadevaia et al. 2018; Theil et al. 2019). Specifically, direct RNA-protein interactions are UV crosslinked in the oligodendrocyte precursor cell line, Oli-neu. The RNA of interest is subsequently isolated from the cell lysate with an array of modified RNA antisense oligonucleotides (ASO). Proteins bound to the target mRNA are identified by mass spectrometry analysis (Fig 5A). *Mbp* mRNA and its protein interactors are the best described RNP complexes in oligodendrocytes and thus used as control. To account for non-specific protein background resulting from direct binding to the RNA antisense oligonucleotides or beads, we devised several no-target controls. For each sample we collected and analysed the flowthrough and eluate of the cell lysate samples and a cell lysis buffer control, with and without the respective targeted ASO (Fig Sup 2A and B).

To assess pulldown efficiency and specificity, we measured *Fth1* and *Mbp* RNA levels in the flowthrough and elution of the cell lysate by RT-qPCR. Compared to the flowthrough fractions, the *Fth1* and *Mbp* transcript were enriched ±2-fold and ±10-fold in the respective elution fractions (Fig Sup2A, (4) and (8)), indicating the successful *Fth1* and *Mbp* pulldown from cell extracts. Enrichment differences might be due to differences in the accessibility of the native mRNA secondary structures to the RNA antisense oligonucleotides.

In our pilot experiment we subjected all flowthrough and eluate samples, together with non-target controls, to mass spectrometry analysis. We employed label-free quantification (LFQ) to accurately determine peptide intensities and disregarded all proteins identified in the beads only fraction (Fig Sup2C). The fold changes in the LFQ intensities were comparable between the *Fth1* and *Mbp* lysates and further reproduced in the flowthrough samples after pulldown (Fig Sup2B). The high correlation coefficient between sample lysates and the flowthrough material is indicative that the flowthrough retains many of the non-specific cell proteins and impurities from the pulldown method, which are then excluded from the eluate fraction.

We analysed the gene ontology (GO) terms of the candidates using all detected proteins. Significant molecular functions were determined (significance cut-off: p-value < 0.05; moderate t-test, Benjamini-Hochberg correction) when comparing RNA flowthrough and eluate samples and *Fth1* and *Mbp* eluate samples. GO terms related to RNA metabolism were highly represented and enriched in the eluate fractions (Fig 5B). Among the top ten enriched molecular functions related to RNA metabolism and localising RNAs, gene terms of nucleic acid binding (namely RNA binding, mRNA binding, mRNA 3'UTR and 5'UTR binding), translation regulator activity (including translation initiation factor activity and translation elongation factor activity) and ribonucleoprotein complex binding were implicated in both eluate samples (Fig 5B).

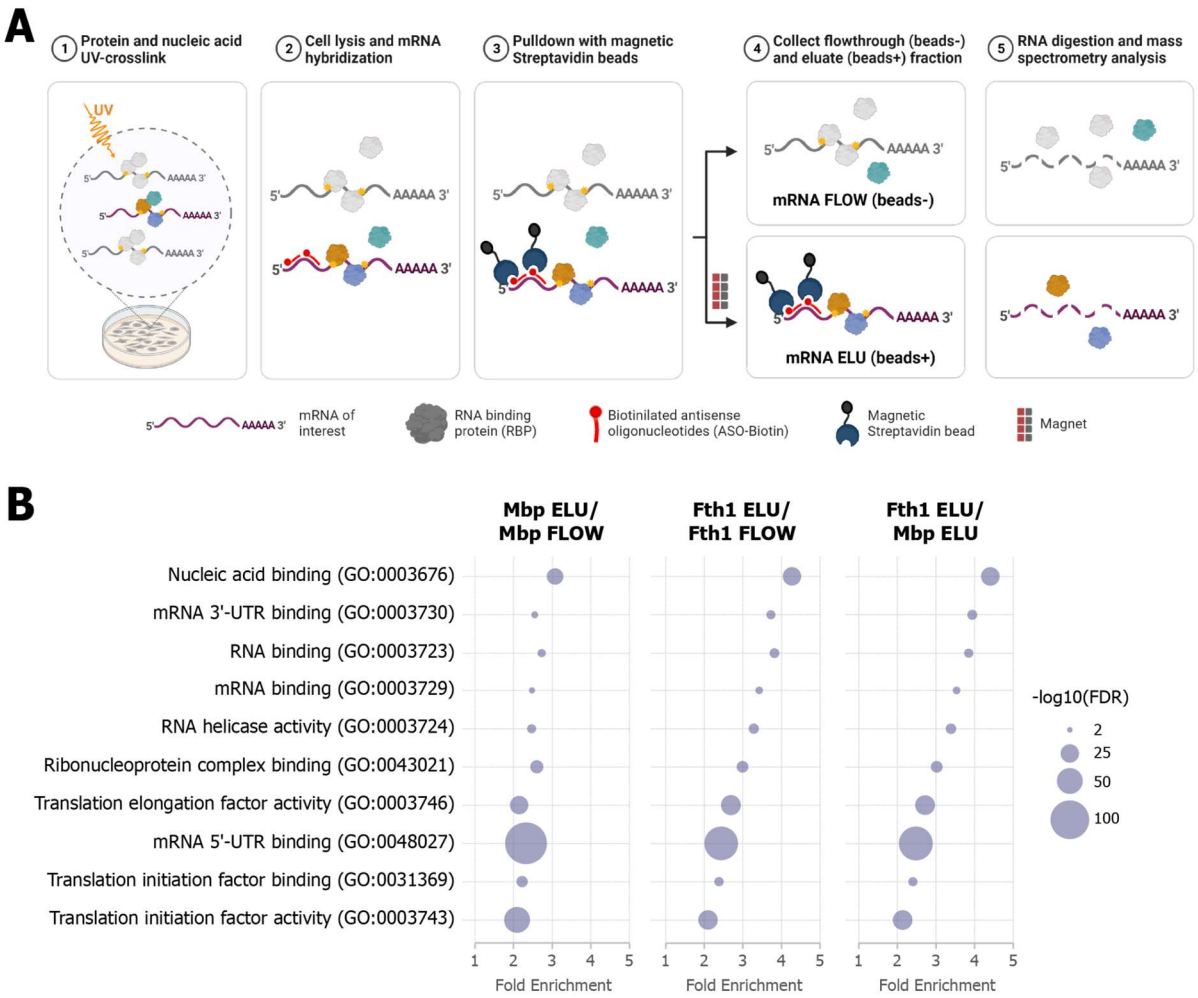

Fig 5 - Development of an *in vitro* RNA-protein crosslinking and pulldown approach that specifically enriches for the RNAs of interest. (A) Diagram of RNA-protein crosslinking and pulldown strategy: 1) differentiated oligodendrocyte precursor cells (Oli-neu cell line) are irradiated with UV light to crosslink proteins that are directly binding to nucleic acids; 2) after cell lysis, biotinylated antisense oligonucleotides (ASO) hybridise to the RNA of interest; 3) the target ASO-RNA-Protein complexes are captured by streptavidin-coated magnetic beads; 4) the magnetically labelled RNA (mRNA ELU, beads+) is retained within the column, while any other unlabelled material flows through the column (mRNA FLOW, beads-); 3) after selective elution the samples were subjected to mass spectrometry (LC–MS/MS) for protein identification. **(B)** Bubble plot representing the significantly enriched molecular functions (p-value < 0.05; moderate t-test, Benjamini-Hochberg correction) of the proteins identified in the *Mbp* (left) and *Fth1* (middle) eluate fractions and in the *Fth1* eluate compared with the *Mbp* eluate fractions (right). In all conditions the highly enriched molecular functions associated with the target RNA were related to nucleic acid binding, RNA and mRNA binding. Showing that indeed our pulldown strategy purifies RNA related proteins and more specifically the class of RNA binding proteins. y-axis: gene ontology (GO) terms for the molecular functions; x-axis: molecular function fold enrichment; bubble size: the negative logarithm of the adjusted p value for the false discovery rate (FDR), an important indicator of the reliability to identify differentially expressed proteins.

There is an overall abundance of RNP proteins in relation to localising mRNAs (Müller et al. 2015). As such it is unlikely that the pulldown of a RNA-protein complex will completely deplete the binding RNP from the flowthrough fraction when compared to the eluate. This is further shown by plotting the fold change in the LFQ intensities between *Fth1* flowthrough and eluate and *Mbp* flowthrough and eluate samples (Fig 6A).

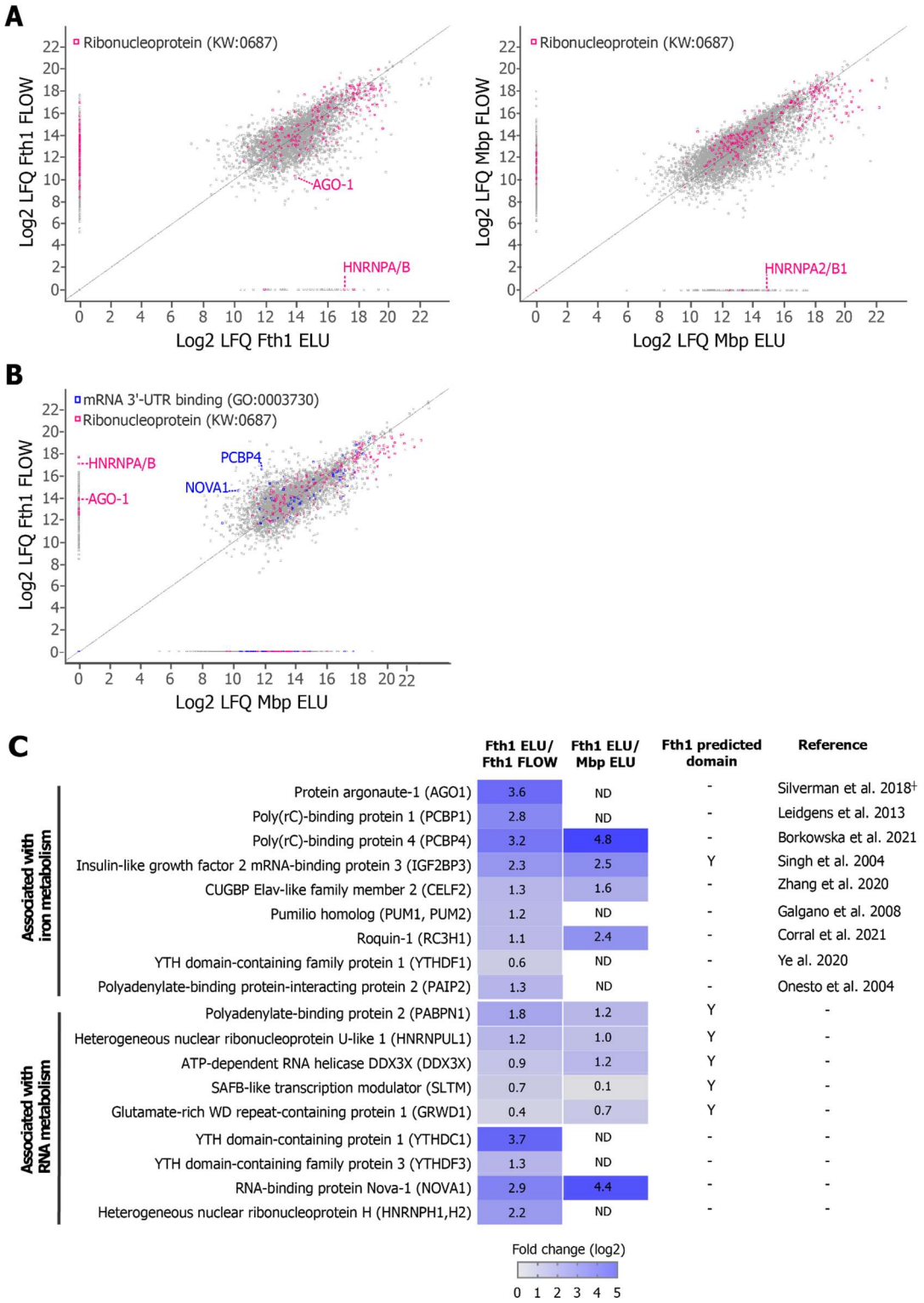

Fig 6 - *Fth1* and *Mbp* eluate fractions show an enrichment for ribonucleoproteins. (A) Scatter plot of the quantified proteins in the *Fth1* (left) and *Mbp* (right) fractions. The data is expressed as the log2 transformed protein abundances (log2 LFQ) of all proteins in eluate and flowthrough fractions, and plotted against one another in the x- and y-axes, respectively. Pink-coded dots represent annotated ribonucleoproteins according to UniprotKB Keywords (KW). Enriched proteins in the eluate fraction, such as AGO-1 in the *Fth1* eluate, are represented below the plotted linear regression line. The contrasting numbers of ribonucleoproteins found only in the eluate or flowthrough fractions compared to the number of RNPs identified in both fractions, suggest that some RNPs might not be as promiscuous as previously thought. So far, HNRNPA2/B1 is the only RNP suggested to behave in this manner, and indeed we found

this protein exclusively in the *Mbp* eluate fraction. **(B)** Scatter plot of the quantified proteins in the *Mbp* and *Fth1* eluate fractions. The data is expressed as the log2 LFQ of all proteins in both eluate fractions, and plotted against one another in the x- and y-axes, respectively. Pink-coded dots represent annotated ribonucleoproteins according to UniprotKB Keywords (KW). Blue-coded dots represent annotated mRNA 3'UTR binding proteins according to gene oncology terms (GO). Proteins more enriched in the *Fth1* eluate fraction are represented above the plotted linear regression line. Some proteins such as NOVA1 and PCBP4 are highly enriched in the *Fth1* fraction when compared to the *Mbp* fraction, suggesting a potential higher affinity for the *Fth1* mRNA. Other proteins show some RNA specificity and can only be found in the *Fth1* fraction, such as AGO-1. **(C)** Heatmap illustrating potential RNP binding candidates of the *Fth1* mRNA. Columns indicate (from left to right): the protein name; fold change of the specific protein between the *Fth1* eluate and flowthrough fractions; fold change of the specific protein between the *Fth1* and *Mbp* eluate fractions; if *Fth1* mRNA sequence is predicted to have a binding domain that was previously shown to bind to the specific protein as identified in Table Sup2; reference to the publication suggesting a role for the protein in iron metabolism. Data are represented as the log2 LFQ of the protein abundance between the indicated fractions. Values were colour coded as shown below. ND: not detected in the *Mbp* eluate fraction. †bioRxiv preprint publication, not peer-reviewed. Y: *Fth1* mRNA is predicted to have a RNA domain shown to be bound by the RNP.

Most ribonucleoproteins, as annotated by UniProt keywords (KW), can be found in both fractions; very few RNPs are found exclusively on the eluate fraction. Proteins found in the *Mbp* eluate fraction only, include the characteristic example of the HNRNPA2B1 protein, one of the few RNPs known to specifically recognize A2RE within the *Mbp* mRNA 3'UTR (Munro et al. 1999) (Table S1). For our transcript of interest, we found that the HNRNPA/B protein is detected only in the *Fth1* eluate fraction. HNRNPA/B protein binds to CArG box motifs in single-stranded and double-stranded DNA and RNA. However, CArG box is not a predicted motif of the *Fth1* transcript (Table Sup2), and little is known about the role and functional characteristics of this RNP. Further studies will help resolve whether HNRNPA/B is an *Fth1* mRNA binding partner and identify its binding sequence or structure.

To narrow down potential proteins associated with *Fth1* mRNA we compared enriched proteins within the *Fth1* eluate to the *Fth1* flowthrough and the *Fth1* eluate to the *Mbp* eluate (ratio > 1). Subsequently, we selected all proteins annotated as ribonucleoproteins (KW:0687, 31 proteins), mRNA 3'-UTR binding (GO:0003730, 19 proteins) or mRNA binding (GO:0003729, 53 proteins) proteins. Out of the resulting protein list, we further identified proteins associated with iron metabolism or for which *Fth1* mRNA is predicted to have binding motifs (Table Sup2), together yielding a dataset of 14 protein candidates. In the candidate list we further took note of 4 additional proteins (YTHDC1, YTHDF3, NOVA1 and HNRNPH1) that were shown to be highly enriched, specifically in *Fth1* eluate fraction (Fig 6B). Some candidates such as IGF2BP3 and CELF2 have been shown to be upregulated in human hepatic cells exposed to erastin, showing that these RNPs are sensitive to ferroptosis and iron metabolism (Zhang et al. 2020). For candidates such as the Pumilio proteins (PUM) (Galgano et al. 2008) and Argonaute-1 (AGO1) (Silverman et al. 2018) *Fth1* mRNA was found to be specifically associated with these ribonucleoproteins in targeted microarray and RNA sequencing analysis. On the other hand, the PCBP protein family is well described as iron chaperones for the FTH1 protein, but no information is available on its potential role as a regulator of *Fth1* mRNA (Leidgens et al. 2013; Borkowska et al. 2021). Proteins such as HNRNPUL1, DDX3X and GRWD1 showed some enrichment in the *Fth1* eluate fraction and were suggested as potential binding partners for *Fth1* mRNA due to the presence of the corresponding RNA-binding motif (Table

Sup2). Further experiments are needed to validate the identified proteins as *Fth1* mRNA binding partners in mature oligodendrocytes.

Discussion

The processes of mRNA localization and regulated translation are the mechanism by which gene expression is spatially and temporally restricted to specific sites. Transport and localization of specific mRNAs, rather than the protein, is particularly important for proteins such as MBP, which can alter the cell morphology and thus be harmful if expressed in parts of the cell other than myelin sheaths. It is also more efficient, especially for large cells such as oligodendrocytes, to reuse a given transcript for multiple translations instead of transporting each protein individually from the cell body. Despite recent research efforts, many aspects governing the mRNA dynamics of localising mRNAs in the brain remain unknown. In oligodendrocytes, research has centered on *Mbp* and *Mobp* mRNAs and little is known about the potential for active transport or local translation of other myelin mRNAs. *Fth1* mRNA is the third most abundant transcript (after *Mbp* and *Mopb*) found in purified myelin when compared to brain lysates and myelinating oligodendrocytes (Thakurela et al. 2016; Gould et al. 2000). Conversely, relatively small amounts of FTH1 protein can be found in myelin when compared to brain lysates of adult mice and other myelin proteins (Mukherjee et al. 2020). Interestingly, a longer *Fth1* mRNA isoform, associated with the presence of a 3'UTR region, is enriched in myelin (Gould et al. 2000). The concurrent expression of high levels of *Fth1* mRNA with a 3'UTR region, together with low protein levels, in the myelin sheath could suggest a mechanism for the active transport and silencing of this transcript.

We started by characterising *Fth1* mRNA expression in oligodendrocytes using *in situ* hybridization coupled with protein staining. In both mouse and human oligodendrocytes, *Fth1* mRNA and FTH protein levels gradually increase throughout differentiation. *Fth1* mRNA shows the highest expression in myelinated cells. Similar to *Mbp* mRNA, the *Fth1* transcript shows a characteristic granular distribution along the distal processes, associated with cytosolic transport and localising mRNAs *in vitro*. Moreover, *Fth1* and *Mbp* transcripts did not co-localize within the same RNA granules. *Fth1* and *Mbp* mRNA expression pattern as separate cytoplasmic foci in oligodendrocytes was further validated in 6-month-old mice cortex, where it again showed a non-colocalising granular pattern within the cortical myelin tracts.

The presence of cytosolic RNA puncta can be associated with different types of RNA granules that support the preservation of cell homeostasis under normal and stress conditions (Tian et al. 2020). All RNA granules harbour translationally silenced mRNAs, some are cell specific, and others are ubiquitous to many cell types. Germ cell granules, neuronal granules and *Mbp* mRNA granules are examples of cell specific granules that require a highly specific mRNA cargo. Whereas stress granules and P-bodies are found in many cell types and are less cargo discriminating. SGs form in response to cellular stress to store mRNAs that have exited the translational pool and completely dissolve after removing the stress stimuli. P-bodies temporarily hold mRNAs not engaged with ribosomes until their degradation or translation (Anderson and Kedersha 2006; Moujaber and Stochaj 2018; Thomas et al. 2011). Although the content of each type of RNA granule is distinct, many proteins are found in more than one type of granule and different RNA granules can contain or exclude ribosomes. *Mbp* mRNA granules appear to contain ribosomal RNA and ribosomal subunits, packaged in an inert fashion that prevents translation (Barbarese et al. 1995; Colman et al. 1982). SGs contain only small ribosomal subunits derived from disassembled polysomes, while P-bodies lack ribosomal subunits altogether (Hubstenberger

et al. 2017). In myelinating oligodendrocytes, *Fth1* mRNA appears to not co-colocalize with either SG (G3BP1) or P-bodies (DCP1A) protein markers. We also analysed *Fth1* and *Mbp* mRNA expression in relation to the 40S ribosomal component (anti-S6). *Fth1* mRNA appears to co-occur less frequently with the ribosomal marker than *Mbp* mRNA containing granules. Together the data would suggest that *Fth1* mRNA are cytoplasmic foci distinct from the ubiquitous RNA granules, SGs and P-bodies, and distinct from the *Mbp* mRNA granules.

RNA granule transport and translation are regulated in the context of specific ribonucleoprotein complexes to control the timing and location of protein synthesis. The composition of RNP complexes is determined by a combination of *cis*-regulatory motifs within the mRNA sequence and *trans*-acting proteins. The *cis*-acting localization elements can be very heterogenous in size and structure and are often, but not exclusively, located within the mRNA 3′ UTR (Doyle and Kiebler 2011). Some RNPs bind single-stranded RNA and recognize a primary sequence motif (HNRNPA2) (Munro et al. 1999), others recognize a secondary structure in the RNA (Staufen proteins) or they can recognize both a primary sequence and a secondary structure (ZBP1) (Stefl et al. 2005). Due to the complexity of RNA secondary structure, it is challenging to characterise these binding sequence motifs both at the level of sequence and structure. Moreover, it is likely that localising mRNAs contain more than one copy of a localisation element as well as combinations of different *cis*-acting motifs mediating distinct steps in localization (Chabanon et al. 2004). Taking together all the different complexity elements associated with these localization sequences, it is not surprising that identification of these elements based on RNA and protein sequences, structural motifs and even by computational prediction, is not reliable and always has to be validated in its physiological context. To this end, we optimised an RNA-centric approach that allows the pulldown of a specific RNA of interest and its associated proteins that can be further identified by mass-spectrometry analysis. Using this approach, we identified the HNRNPA/B protein, which was found to be specifically enriched in the *Fth1* mRNA binding fraction, and an additional 18 potential RNPs candidates that could be associated with *Fth1* mRNA translocation and/or translation repression in oligodendrocytes. Further experiments are needed to validate the identified proteins as *Fth1* mRNA binding partners in mature oligodendrocytes. Loss-of-function as well as gain-of-function experiments that selectively interfere with the binding RNP or the localising motifs in the RNA, could provide insights into the interacting nature between RNA and RNP candidates. Additionally, *in vitro* RNA tracking, using coupling systems such as MS2-fluorescence complementation RNA labelling (Wu et al. 2014; Park et al. 2020), will help resolve whether the RNA localization or translation is selectively impaired, when we interfere with the RNP function. Identification of *Fth1* mRNA interacting proteins, can uncover the impact of neuronal cues in the regulation of FTH1 protein expression and secretion by oligodendrocytes.

In summary, organising transcripts into RNA granules allows for a highly flexible system that supports rapid adaptive responses to changes in cell physiology or signalling events. Given the importance of FTH1 protein for neuronal protection against iron-mediated cytotoxicity it is reasonable to expect that targeted transport and local translation of *Fth1* mRNA could effectively provide a way for oligodendrocytes to rapidly respond to external stimuli. Our data indicate that in oligodendrocytes *Mbp*, *Mobp* and *Fth1* mRNAs show an expression pattern associated with cytoplasmic RNA granules *in vitro* and *in vivo.* These cytoplasmic foci do not co-localize in the same RNP granule. Packing of the RNA in distinct RNA granules would allow for selective translation regulation and delivery, thus

contributing to signal specific modifications and high plasticity at the RNA level. Together, the distinct subcellular localization between *Fth1* mRNA and other known cytoplasmic RNA granule markers (stress granules and P-bodies) could indicate a new mechanism of translational repression for the *Fth1* mRNA at the distal OLG processes. We further developed a proteomics approach to selectively isolate native RNA-protein complexes, and identify potential interacting RNPs involved in the transport and translational repression of *Fth1* mRNA in mature oligodendrocytes. The development of new experimental approaches that allow high-resolution imaging of mRNA localization in living cells will undoubtedly yield new mechanistic insight in the underlying process of *Fth1* mRNA localization and translation control.

Materials and Methods

Oligodendroglial cell culture. Primary oligodendrocyte cultures were established from P7-P8 C57BL/6J wild-type mice brains. Oligodendrocyte precursor cells were isolated via immunopaning with anti-PDGFRA antibody (anti-mouse CD140a, Biozol, 135902) (Emery and Dugas 2013). Briefly, brain tissue was dissociated in a papain buffer (20/mL units, Cell systems, LS003126) at 37°C for 90 min. Brain lysate was sequentially incubated in negative selection BSL1 (Vector Laboratories, L1100) coated cell culture dishes and finally in anti-mouse PDGFRA coated tissue culture dishes for the positive selection of OPCs. Cells were cultured in poly-L-lysine (Merck, P6282) coated coverslips in DMEM-SATO base growth media supplemented with Forskolin (4.2 mg/mL, Merck, F6886) and CNTF (10µg/mL, Prepotech, 450-13), together with PDGFAA (10µg/mL, Prepotech, 100-13A) and NT3 (1µg/mL, Prepotech, 450-03) to promote cell proliferation or T3 (4µg/mL, Merck, T6397) to induce OPC differentiation. Cells were cultured for the indicated time periods and fixed in 4% paraformaldehyde for 10 min at room temperature.

Oli-neu cells (kindly provided by Jacqueline Trotter, University of Mainz, Germany) were cultured in DMEM supplemented with N1 (Merck, N6530) and 3% horse serum (ThermoFisher Scientific, 26050088) on poly-L-Lysine coated tissue culture plates. Oli-neu differentiation was induced by culturing these cells in serum-free DMEM-N1 media supplemented with 2 mM 8Br-cAMP (Merck, B7880) for 48 hrs (de Faria et al. 2019).

IPSC-derived oligodendrocytes cell culture. iPSC experiments were performed in accordance with all relevant guidelines and regulations. SON-RFP iPSC line was maintained on vitronectin-coated (ThermoFisher Scientific, A14700) cell culture plates and grown in StemFlex Medium (ThermoFisher Scientific, A3349401) supplemented with 300 ng/mL of puromycin dihydrochloride (Merck, P8833), at 37°C with 5% CO2. To induce oligodendroglial differentiation, the SON-RFP iPSCs were dissociated into single cells using Accutase (Merck, A6964) and seeded at a density of 20.000 cells/cm2 on GelTrex (ThermoFisher Scientific, A1413302) coated plates in StemFlex medium supplemented with 10 µM rock inhibitor analog (Selleck Chemical, Y27632) and puromycin for two days (day in vitro -2). At day 0, media was changed to N2B27 medium supplemented with the dual SMAD inhibitors: 10 µM SB431542 (Selleck Chemical, S1067) and 0.25 µM LDN193189 (Selleck Chemical, S2618); together with 100 nM retinoic acid (Merck, R2625) and puromycin. On day 8, 1 µM of smoothened agonist (Selleck Chemical, S7779) was further added to the media. Media was changed daily. At day 12, cells were dissociated using Accutase and seeded at 75.000 cell/cm2 on poly-L-ornithine (Merck, P3655)/laminin (ThermoFisher Scientific, 23017015) coated coverslips. Cells were cultured in oligodendrocyte differentiation media supplemented (N2B27 medium supplemented with 1 µM cAMP (Merck, A9501), 10 ng/mL NT3 (Peprotech, 450-03), 10 ng/mL IGF-1 (Peprotech 100-11), 10 ng/mL PDGFAA (Peprotech, 100-13A), 5 ng/mL HGF (Prepotech, 100-39H), 100 ng/mL Biotin (Merck, B4639), 60 ng/mL T3 (Merck, T6397) and 2 µg/mL doxycycline (Merck, D9891) for 16 days, changing the medium every 2-3 days.

Fluorescent *in situ* hybridization and immunocytochemistry. The ViewRNA Cell Plus Assay (ThermoFisher Scientific, 88-19000-99) was used for *in situ* hybridisation analysis of primary mouse oligodendrocytes and human iPSC-derived

oligodendrocytes. Cells were fixed in 4% paraformaldehyde for 10 min at room temperature and carefully washed with 1x phosphate buffer saline (PBS) and RNase inhibitor. Cells were kept at 4°C until further processing for a maximum of 5 days. The cells were further permeabilized with a 1xPBS solution with 0.1% Triton X100 (Merck, X100) and 0.1% Sodium citrate (Merck, 25114) in ice for 10 min. After permeabilization, the assay was performed according to the manufacturer's instructions in the ViewRNA® Cell Plus Assay protocol, with the primary and secondary antibody protein stainings followed by the target probe hybridisation and signal amplification steps. The following antibodies were used: anti-MBP rat (1:500, Abcam, ab7349); anti-FTH1 rabbit (1:300, Abcam, ab65080); anti-G3BP rabbit (1:500, Abcam, ab181150); anti-DCP1A mouse (1:200, Abnova, H00055802-M06) and anti-S6 rabbit (1:500, Cell Signalling, 2217). Fluorescent secondary antibodies were used in a 1:500 dilution, Alexa Fluor 488, Alexa Fluor 555 and Alexa Fluor 647 (ThermoFisher Scientific). The following RNA hybridization probe sets for primary mouse oligodendrocytes were used: mouse *Mbp* 488 (ThermoFisher Scientific, VB4-3112254-VCP, type 4); mouse *Mbp* 546 (ThermoFisher Scientific, VB1-13861-VCP, type 1); mouse *Fth1* 546 (ThermoFisher Scientific, VB1-14586-VCP, type 1); mouse *Mobp* 647 (ThermoFisher Scientific, VB6-3197382-VCP, type 6) and mouse *Plp1* 647 (ThermoFisher Scientific, VB6-18891-VCP, type 6). To detect RNA in the human iPSC-derived oligodendrocytes we used the following probes: human *Fth1* 647 (ThermoFisher Scientific, VA6-3171748-VC, type 6) and human *Mbp* 488 (ThermoFisher Scientific, VA4-12730-VC, type 4). Nuclei were stained with Hoechst 33342 (1:1000, ThermoFisher Scientific, H3570) for 10 min at room temperature. Stained cells were mounted using ProLong Diamond Mounting Medium (ThermoFisher Scientific, P36961).

Fluorescent *in situ* hybridization and immunohistochemistry. The RNAscope Multiplex Fluorescent v2 Assay (Advanced Cell Diagnostics, 323100) was used for in situ hybridisation analysis of mouse cortical sections. To prepare mouse tissue samples for *in situ* hybridization and immunohistochemistry, C57BL/6J wild-type mice were anaesthetized with an intraperitoneal injection of 10% ketamine/2% xylazine and perfused intracardially with 4% paraformaldehyde with a peristaltic pump (Peri-Star PRO, World Precision Instruments). The brain was removed and postfixed in 4% paraformaldehyde overnight and cryoprotected in 30% sucrose in 1xPBS. The tissue was embedded in Tissue-Tek O.C.T, frozen on dry ice and kept at −80 °C until sectioning. For sectioning, a cryostat (Fisher Scientific, CryoStar NX70) was used to cut 14-16 µm thick coronal sections, which were directly mounted on Superfrost Plus slides (ThermoFisher Scientific). All sections were kept at −20 °C until further processing. The RNAscope Multiplex Fluorescent v2 Assay was performed according to the manufacturer's instructions for fixed frozen tissue. First, 16-µm-thick brain sections were hybridised with the respective RNA probes: RNAscope Probe-Mm-*Fth1*, (Advanced Cell Diagnostics, 511561, channel 1); RNAscope Probe-Mm-*Mbp*, (Advanced Cell Diagnostics, 451491, channel 3); RNAscope Probe-Mm-*Mbop*, (Advanced Cell Diagnostics, 431721, channel 2) and RNAscope Probe-Mm-*Plp1* (Advanced Cell Diagnostics, 428181, channel 2). Additionally, the negative control probe (RNAscope 3-Plex Negative Control Probe, 320871) and the positive control probe (RNAscope 3-plex Positive Control Probe_Mm, 320881) were used in some sections, to assure the specificity and the sensitivity of the signal. Different fluorophores were assigned to each probe channel: Channel 1 and 2 - Opal 520 Reagent Pack (Akoya Biosciences, FP1487001KT) and Channel 3 - Opal 690 Reagent Pack (Akoya Biosciences, FP1497001KT). The target probes were also combined with immunofluorescence with anti-MBP rat (1:500, Abcam, ab7349) and Alexa 488 (1:500, TermoFisher Scientific, A-21210) in order to identify myelin segments. Nuclei were stained with Hoechst 33342 (1:1000, ThermoFisher Scientific, H3570) for 15 min at room temperature. Sections were mounted using ProLong Diamond Mounting Medium (ThermoFisher Scientific, P36961).

Oxidative stress induction for SG. To induce the formation of stress granules through oxidative stress, primary mouse oligodendrocytes were treated with 0.5 mM Sodium Arsenite (NaAs) (Merck, S7400) for 1 hour at 37 °C and 10% CO2. Control samples were treated with the same volume of MiliQ water, the NaAs resuspending

solution. Cells were fixed with 4% paraformaldehyde for 10 min at room temperature and carefully washed with 1xPBS and RNase inhibitor. Samples were kept at 4°C until further processing for a maximum of 5 days.

Design and synthesis of RNA specific biotinylated antisense oligonucleotides (ASO probes). Each target mRNA sequence reference was obtained from the NCBI-Gene database for *Mus musculus* (https://www.ncbi.nlm.nih.gov/gene/). ASO probes were designed using the ChIRP Probe Designer version 4.2 from Biosearch Technologies (https://www.biosearchtech.com/chirp-designer) with the following parameters: organism *Mus musculus*, oligo length 20-24 bp, minimum spacing length 60 and masking level 5. Suggested ASO sequences with a GC ratio of 50% were assessed for RNA specificity through NCBI Standard Nucleotide BLAST software (https://blast.ncbi.nlm.nih.gov/). Subsequently, we selected all probes showing less than 60% sequence homology with other RNAs. 5 sequences tiling the 3'and 5'UTR region of the target transcripts were synthesised with 2'-methoxy modified RNA bases and a biotin moiety at the 3' (3BioTEG) (Integrated DNA technologies). ASO probes were reconstituted with TE buffer solution to a final concentration of 100 µM. ASO sequences (in 5′-3′ orientation) of target transcripts as follow, *Fth1* mRNA: RNAFth1-5 AGA AAA GAU GAA GGC AGC CUG; RNAFth1-6 AAG CAG AUG UUU UGG UGC AAC; RNAFth1-7 AAG CAC UGU UGA AGC AGG AAA C; RNAFth1-9 CAG UGA CCA GUA AAG UCA CGU G; RNAFth1-10 UAG AAA AGA UGA AGG CAG CCU G; and *Mbp* mRNA: RNAMbp-15 GGC AGU UAU AUU AAG AAG CCG; RNAMbp-18 AAU AGU UUU AAC CAG UCG GGG; RNAMbp-19 CCC GAG AAA ACU CAA UCU UCA; RNAMbp-24 UUU CUU AAA AGC ACC AGC UCU G; RNAMbp-26 CGA GGU UAG UGU GUA CCA AUG.

RNA pulldown. Oli-neu cells were cultured in standard 150 mm tissue culture dishes, until ≈70% confluent and further differentiated for 48h. Experiments were typically performed with ≈10 dishes per condition. Cells were washed 3 times in 1x PBS, placed in ice and transferred to a CL-1000 Ultraviolet crosslinker (UVP) at a wavelength of 254 nm at 120 mJ cm-2 (≈2 min). Crosslinked cells were scraped, pelleted and flash frozen in liquid nitrogen. Pellets were kept at −80 °C until further processing.

Frozen pellets (≈50 mg) were resuspended in 1mL of pre-chilled lysis buffer (50 mM Tris–HCl, pH 7.5 (ThermoFisher Scientific, 15567027); 10 mM EDTA, pH8 (ThermoFisher Scientific 15575020); 1% LiDS (Merck, L9781); 500 mM LiCl (Merck, L9650); 1 mM DTT (ThermoFisher Scientific, 707265ML); 1x tablet Complete EDTA-free Protease Inhibitor (Merck, 11836170001); 100 U/mL RNasin Plus Ribonuclease Inhibitor (Promega, N2615); 20 U/mL RQ1 RNase-Free DNase (Promega, M6101)) by pipetting up and down for 5-6 times, while keeping the tube on ice. Samples were forced through a 21 gauge needle 3–5 times using a 1–2 mL syringe to shear the DNA. Lysates were cleared by centrifugation (14,000 × g, 4 °C, 10 min), pellets were discarded. Supernatant protein concentration was determined using NanoDrop Protein absorbance at A280 (Fisher Scientific) and diluted to a final protein concentration of 2 - 4 mg/mL by adding at least 3x volume of pulldown hybridization buffer (50 mM Tris–HCl, pH 7.5; 10 mM EDTA, pH8; 1% LiDS; 750 mM LiCl; 15% Formamide (ThermoFisher Scientific, 17899); 1x tablet Complete EDTA-free Protease Inhibitor; 100 U/mL RNasin Plus Ribonuclease Inhibitor; 20 U/mL RQ1 RNase-free DNase). Input samples were taken for RNA and protein analysis. The pulldown procedure was adapted from Theil et al. 2019 with modifications.

DYNAL Dynabeads M-280 Streptavidin magnetic beads (100 µL per 1 mL lysate with protein concentration 2 mg/mL, Thermo Fisher Scientific, 11206D) were washed 2 times with 1 mL of binding and washing buffer (10 mM Tris–HCl, pH 7.5; 0.5 mM EDTA, pH8; 150 mM NaCl (Merck, S9888)). To ensure complete removal of beads from the solution, tubes were placed on a DynaMag-2 magnet rack (Thermo Fisher Scientific, 12321D). Magnetic beads were resuspended in 10 mg/mL of tRNA from E. coli MRE 600 (Merck, 10109541001) in the binding and washing buffer and incubated at room temperature for 1 hour under constant rotation. Pre-treated beads were further washed 3 times with binding and washing buffer, resuspended in pulldown hybridization buffer and kept in ice until use.

For hybridization of the ASO probes to sample mRNA, each transcript specific ASO was pooled at 100 pmol per ASO, added to the lysate sample and incubated at 37°C for 2-2.5 hours under constant rotation. For probe capture, pre-treated DYNAL

Dynabeads M-280 Streptavidin magnetic beads were added to the samples and incubated for an additional hour at 37°C. Beads-mRNA complexes were separated from the supernatant and the flowthrough (beads -) was collected. Beads-mRNA complexes were slowly and carefully washed at least 5 times with 1 mL of wash buffer (0.3 M NaCl, 0.03 Sodium citrate, 0.5% LiDS, 0.1M DTT). Finally, beads were resuspended in 1 mL wash buffer and transferred to Protein LoBind tubes (Thermo Fisher Scientific, 88380). Wash buffer was removed via magnet and beads resuspended in Benzonase elution buffer (10 mM Tris–Cl, pH 7.5; 1 mM MgCl2; 1 mM DTT; 0.625 U/µL Benzonase Nuclease HC (Merck, 71205-3)) for protein elution or Proteinase K buffer (10 mM Tris–Cl, pH 7.5; 1 mM EDTA, pH 8.0; 0.5% LiDS; 100 mM NaCl; 1 mg/mL Proteinase K (Merck, 3115879001)) for RNA isolation, respectively.

For protein elution, beads were resuspended in 100 µL of Benzonase elution buffer. Crosslinked proteins were eluted by incubation at 37°C for 3 h, shaking at 1300 rpm. Beads were separated from elutate via magnet and transferred to new Protein LoBind tubes. Samples were snap-frozen in liquid nitrogen and kept at −80 °C until further processed. For RNA isolation, beads-RNA complex, and 100 µL of input and supernatant samples were resuspended in 100 µL Proteinase K buffer, and incubated at 50°C for 45 min, shaking at 1300 rpm, followed by Proteinase K inactivation at 95 °C for 10 min. RNA cleaned up and concentrated using the RNeasy Micro kit from Qiagen (74004) and following the RNA Cleanup and Concentration protocol as described by the manufacturer.

RT-PCR. Total RNA was isolated from RNA pulldown input, eluate and flowthrough samples. The RNA was retrotranscribed with SuperScript IV First-Strand Synthesis System (ThermoFisher Scientific, 18091050), using random hexamer primers and 20 ng of total RNA, as determined by NanoDrop absorbance A260. Quantitative PCR was performed using the PowerUp SYBR Green Master Mix (Applied Biosystems, A25742) on a LightCycler 480 Real-time PCR system (Roche). All qPCR reactions were run in duplicate. Primer sequences (in 5′-3′ orientation) of target genes are as follows: *Fth1* forward TCT CAT GAG GAG AGG GAG CAT; reverse TCA TCA CGG TCT GGT TTC TTT A; *Mbp* forward TGT GCC ACA TGT ACA AGG ACT; reverse GTT TTCA TCT TGG GTC CGG C. The melting curve was included at the end of the run to ensure specificity of the primers. The comparative dCt method was used to measure the amplification of mRNAs relative to the input sample.

Sample Preparation. The protein concentrations of the samples were estimated using the Pierce 660 nm assay (ThermoFisher Scientific). A protein amount of 10 µg per sample was subjected to tryptic digestion using a modified single-pot, solid-phase-enhanced sample preparation as previously described (Sielaff et al. 2017). Proteins were reduced at 37°C for 30 min with 15 mM dithiothreitol (DTT) followed by cysteine alkylation with 60 mM iodoacetamide (IAA) for 30 min at 20°C. Excess of IAA was removed by adding DTT. Detergent removal and subsequent digestion with 125 ng LysC and 125 ng trypsin (Promega) were performed according to the previously published protocol (Sielaff et al. 2017). Afterwards, the peptide solution was filtered through 0.2 µm Costar Spin-X filters (Corning). After vacuum centrifugation, peptides were dissolved in 20 µL 0.1% formic acid (Sigma Aldrich). Peptide concentrations after tryptic digestion were estimated using the Qubit protein assay (ThermoFisher Scientific).

LC-MS/MS analysis. 300 ng of peptides were separated on a nanoElute nanoHPLC system (Bruker), an in-house packed C18 analytical column (15 cm × 75 µm ID, ReproSil-Pur 120 C18-AQ, 1.9 µm, Dr. Maisch GmbH). Peptides were separated with a binary gradient of water and acetonitrile (B) containing 0.1% formic acid at flow rate of 300 nL/min (2% B 0 min; 5% B 3.5 min; 24% B 48 min; 35% B 59 min; 60% 64 min; and 85% B 65 min) and a column temperature of 50°C.

The nanoHPLC was online coupled to a TimsTOF pro mass spectrometer (Bruker) with a CaptiveSpray ion source (Bruker). For relative protein quantification, a Data Independent Acquisition (DIA) – Parallel Accumulation Serial Fragmentation (PASEF) method was used (Meier et al. 2020). Each scan cycle included one full MS scan followed by 26 windows of 27 m/z width (2 m/z overlap) covering an m/z range of 350-1000 using 2 windows per PASEF ramp of 100 ms, this resulted in a cycle time of 1.4 s.

Data Analysis. The MS raw data was analysed with the Software DIA-NN (Version 1.8) (Demichev et al. 2020) using a library free search against a canonical one protein per gene protein database of *Mus musculus* from UniProt (download: 2021-04-09, 21998 entries, https://www.uniprot.org). Trypsin was defined as protease and 2 missed cleavages were allowed. The data was searched. Oxidation of methionines and acetylation of protein N-termini were defined as variable modifications, whereas carbamidomethylation of cysteines was defined as fixed modification. The precursor and fragment ion m/z ranges were limited from 350 to 1000 and 200 to 1700, respectively. Peptide and peptide fragment mass tolerances were optimised by DIA-NN. The match between runs option was enabled. A FDR threshold of 1% was applied for peptide and protein identifications. UniProt subcellular location annotations were added based on the protein group accession numbers (download: 2019-06-18). The LFQ intensities were used to calculate abundance ratios between the different conditions.

Protein annotation and analysis. Perseus software suite (https://maxquant.net/perseus, version 2.0.3.1) (Tyanova et al. 2016) was employed to carry out data visualisation. Log2-transformed LFQ intensities were reported as multi scatter plots to obtain the R-square as measure of the correlation between samples. All identified proteins were considered for log2 LFQ entries. A zero value was given to the log2 LFQ of proteins in samples for which the protein was not possible to quantify (NaN). Perseus was further employed to obtain profile plots for data visualisation. GO enrichment analyses were performed using the Database for Annotation, Visualisation and Integrated Discovery (DAVID) v2021 (https://david.ncifcrf.gov) (Huang et al. 2009; Sherman et al. 2022) against a background of the *Mus musculus* proteome to calculate Benjamini-Hochberg corrected p-values and false discovery rates (FDR). Enrichment of GO Molecular Function terms was considered statistically significant when p-values < 0.05 for multiple t-test with Benjamini-Hochberg correction. A list of all manually annotated and reviewed ribonucleoproteins (KW:0687) in *Mus musculus* was retrieved from UniProt (download: 2022-03-24, 265 entries). Lists of mRNA 3'-UTR binding (GO:0003730, download: 2022-03-24, 195 entries) and mRNA binding (GO:0003729, download: 2022-03-24, 656 entries) annotated proteins in *Mus musculus* were collected from AmiGO2 web-based tool v2.5.17 (http://amigo.geneontology.org/amigo) (Carbon et al. 2009). To identify potential proteins associated with mRNA, proteins were considered if the abundance protein ratio between samples ≥ 1 and the protein is annotated as ribonucleoprotein (KW:0687), mRNA 3'-UTR binding (GO:0003730) or mRNA binding (GO:0003729) protein. Results were visualised by heatmap.

RNA sequence and structure motif scan. The identification of sequence and structure RNA-binding motifs in the target mRNA was conducted using BRIO (BEAM RNA Interaction mOtifs) at http://brio.bio.uniroma2.it (Guarracino et al. 2021). Motif search was performed using the RNA primary sequence of interest as input and comparing the RNA molecule to the whole dataset of motifs identified for *Homo sapiens* and *Mus musculus*, in all experiments (PAR-CLIP, eCLIP or HITS).

Microscopy. Optical sections were acquired with a confocal laser-scanning microscope (Leica TCS SP5, Leica Microsystems) using the 63×Oil/1.40 NA objectives. The different fluorophores were stimulated sequentially using the following laser lines: 405 nm for Hoechst 33342, 488 nm for Alexa Fluor 488 and Opal 520, 561 nm for Alexa Fluor 555 and 633 nm for Alexa Fluor 647 and Opal 690.

Image analysis. The regions of interest in oligodendrocytes, the cell processes, were determined by using the IMARIS v9.2.0 software (Oxford Instruments) 3D freehand selection tool to exclude all pixels associated with the oligodendroglial cell body, as defined by protein and nuclear markers. Relative area occupied by mRNA signal in oligodendrocyte cell processes was quantified using the Fiji software v1.53r (Schindelin et al. 2012). All samples were analysed at the same threshold values after applying the Fiji despeckling tool to reduce the number of false positive mRNA signal. Within each pre-defined ROI, the area occupied by the mRNA signal was measured using the Analyse particles plugin and expressed as area fraction (%) per cell.

The extent of colocalization between mRNAs or between mRNA and protein were measured

quantitatively by Pearson's correlation coefficient (PCC) and Mander's correlation coefficient (MCC) using IMARIS image analysis software.

To measure PCC, Imaris employs the approach developed by Costes et al. 2004. The degrees of co-localization from the Pearson's values vary between +1 and -1, where values near 1 indicate a direct correlation and values near 0 indicate no correlation. Since PCC values depend upon a simple linear relationship, they will be underrepresented if measured in cells with heterogeneous expression of the target molecules, thus under-representing the degree of correlation. Hence, it is important to analyse both PCC and MCC values in co-localization studies. MCC strictly measures co-occurrence independent of signal proportionality, but it is affected by signal intensities (Dunn et al. 2011). First the mRNA and protein puncta were selected using the maximum intensity value as a threshold. Using this same threshold intensity value, a colocalization channel and two-dimensional intensity histogram of the selected channels was built. Two different MCC values are given (M1 and M2), which describe the independent contributions of two selected channels to the colocalization channel. MCC values range from 0 to 1 while 0 means no colocalization (0%) and 1 perfect colocalization (100%). Co-localization was also qualitatively assessed by linescans. Intensity linescans were produced using the multichannel plot profile tool of the BAR collection v1.5.2 in Fiji software.

Statistical analysis. Statistical analysis was performed with GraphPad Prism 7 v7.04 software (GraphPad Software). Data are represented as mean ± SD. The number of cell cultures used for the experiments are indicated as single dots in all graphs or indicated in the figure legends as biological replicates. Each biological replicate represents an average of 3 to 8 random fields of view to account for variability within the biological sample. An exception is the proteomics data in which results are shown for one replicate. To compare two groups, an unpaired nonparametric t-test with the Kolmogorov-Smirnov method was applied using the GraphPad Prism software. A p value of ≤0.05 was considered significant in all cases.

Data availability

The raw data that support the findings of this study are available from the corresponding author upon reasonable request.

References

Anderson, P., & Kedersha, N. (2006). RNA granules. *The Journal of Cell Biology*, 172(6), 803–808.

Barbarese, E., Koppel, D. E., Deutscher, M. P., Smith, C. L., Ainger, K., Morgan, F., & Carson, J. H. (1995). Protein translation components are colocalized in granules in oligodendrocytes. *Journal of Cell Science*, 108 (Pt 8), 2781–2790.

Baron, P., Kamholz, J., Scherer, S., Honda, H., Shy, M., Scarpini, E., Scarlato, G., et al. (1993). Appearance of PLP mRNA in specific regions of the developing rat lumbosacral spinal cord as revealed by in situ hybridization. *Experimental Neurology*, 121(1), 139–147.

Borkowska, A., Tomczyk, M., Żychowska, M., Pilis, W., Zych, M., & Antosiewicz, J. (2021). Effect of 8-Day Fasting on Leukocytes Expression of Genes and Proteins Involved in Iron Metabolism in Healthy Men. *International Journal of Molecular Sciences*, 22(6).

Chabanon, H., Mickleburgh, I., & Hesketh, J. (2004). Zipcodes and postage stamps: mRNA localisation signals and their trans-acting binding proteins. *Briefings in Functional Genomics & Proteomics*, 3(3), 240–256.

Colman, D. R., Kreibich, G., Frey, A. B., & Sabatini, D. D. (1982). Synthesis and incorporation of myelin polypeptides into CNS myelin. *The Journal of Cell Biology*, 95(2 Pt 1), 598–608.

Corral, V. M., Schultz, E. R., Eisenstein, R. S., & Connell, G. J. (2021). Roquin is a major mediator of iron-regulated changes to transferrin receptor-1 mRNA stability. *iScience*, 24(4), 102360.

Doyle, M., & Kiebler, M. A. (2011). Mechanisms of dendritic mRNA transport and its role in synaptic tagging. *The EMBO Journal*, 30(17), 3540–3552.

Dunn, K. W., Kamocka, M. M., & McDonald, J. H. (2011). A practical guide to evaluating colocalization in biological microscopy. American Journal of Physiology. *Cell Physiology*, 300(4), C723-42.

Galgano, A., Forrer, M., Jaskiewicz, L., Kanitz, A., Zavolan, M., & Gerber, A. P. (2008). Comparative

analysis of mRNA targets for human PUF-family proteins suggests extensive interaction with the miRNA regulatory system. *Plos One*, 3(9), e3164.

Gould, R. M., Freund, C. M., Palmer, F., & Feinstein, D. L. (2000). Messenger RNAs located in myelin sheath assembly sites. *Journal of Neurochemistry*, 75(5), 1834–1844.

Guarracino, A., Pepe, G., Ballesio, F., Adinolfi, M., Pietrosanto, M., Sangiovanni, E., Vitale, I., et al. (2021). BRIO: a web server for RNA sequence and structure motif scan. *Nucleic Acids Research*, 49(W1), W67–W71.

Hubstenberger, A., Courel, M., Bénard, M., Souquere, S., Ernoult-Lange, M., Chouaib, R., Yi, Z., et al. (2017). P-Body Purification Reveals the Condensation of Repressed mRNA Regulons. *Molecular Cell*, 68(1), 144-157.e5.

Iadevaia, V., Matia-González, A. M., & Gerber, A. P. (2018). An Oligonucleotide-based Tandem RNA Isolation Procedure to Recover Eukaryotic mRNA-Protein Complexes. *Journal of Visualized Experiments*, (138).

Leidgens, S., Bullough, K. Z., Shi, H., Li, F., Shakoury-Elizeh, M., Yabe, T., Subramanian, P., et al. (2013). Each member of the poly-r(C)-binding protein 1 (PCBP) family exhibits iron chaperone activity toward ferritin. *The Journal of Biological Chemistry*, 288(24), 17791–17802.

Mahboubi, H., & Stochaj, U. (2017). Cytoplasmic stress granules: Dynamic modulators of cell signaling and disease. Biochimica et biophysica acta. *Molecular basis of disease*, 1863(4), 884–895.

Mikl, M., Vendra, G., & Kiebler, M. A. (2011). Independent localization of MAP2, CaMKIIα and β-actin RNAs in low copy numbers. *EMBO Reports*, 12(10), 1077–1084.

Moujaber, O., & Stochaj, U. (2018). Cytoplasmic RNA granules in somatic maintenance. *Gerontology*, 64(5), 485–494.

Mukherjee, C., Kling, T., Russo, B., Miebach, K., Kess, E., Schifferer, M., Pedro, L. D., et al. (2020). Oligodendrocytes provide antioxidant defense function for neurons by secreting ferritin heavy chain. *Cell Metabolism*, 32(2), 259-272.e10.

Müller, C., Schäfer, I., Luhmann, H. J., & White, R. (2015). Oligodendroglial Argonaute protein Ago2 associates with molecules of the Mbp mRNA localization machinery and is a downstream target of Fyn kinase. *Frontiers in Cellular Neuroscience*, 9, 328.

Munro, T. P., Magee, R. J., Kidd, G. J., Carson, J. H., Barbarese, E., Smith, L. M., & Smith, R. (1999). Mutational analysis of a heterogeneous nuclear ribonucleoprotein A2 response element for RNA trafficking. *The Journal of Biological Chemistry*, 274(48), 34389–34395.

Onesto, C., Berra, E., Grépin, R., & Pagès, G. (2004). Poly(A)-binding protein-interacting protein 2, a strong regulator of vascular endothelial growth factor mRNA. *The Journal of Biological Chemistry*, 279(33), 34217–34226.

Park, S. Y., Moon, H. C., & Park, H. Y. (2020). Live-cell imaging of single mRNA dynamics using split superfolder green fluorescent proteins with minimal background. *RNA*, 26(1), 101–109.

Percy, M. E., Wong, S., Bauer, S., Liaghati-Nasseri, N., Perry, M. D., Chauthaiwale, V. M., Dhar, M., et al. (1998). Iron metabolism and human ferritin heavy chain cDNA from adult brain with an elongated untranslated region: new findings and insights. *The Analyst*, 123(1), 41–50.

Schäfer, I., Müller, C., Luhmann, H. J., & White, R. (2016). MOBP levels are regulated by Fyn kinase and affect the morphological differentiation of oligodendrocytes. *Journal of Cell Science*, 129(5), 930–942.

Silverman, I. M., Gosai, S. J., Vrettos, N., Foley, S. W., Berkowitz, N. D., Mourelatos, Z., & Gregory, B. D. (2018). Isolation and sequencing of AGO-bound RNAs reveals characteristics of mammalian stem-loop processing in vivo. *BioRxiv*.

Singh, B., Charkowicz, D., & Mascarenhas, D. (2004). Insulin-like growth factor-independent effects mediated by a C-terminal metal-binding domain of insulin-like growth factor binding protein-3. The *Journal of Biological Chemistry*, 279(1), 477–487.

Stadelmann, C., Timmler, S., Barrantes-Freer, A., & Simons, M. (2019). Myelin in the central nervous system: structure, function, and pathology. *Physiological Reviews*, 99(3), 1381–1431.

Stefl, R., Skrisovska, L., & Allain, F. H.-T. (2005). RNA sequence- and shape-dependent recognition by proteins in the ribonucleoprotein particle. *EMBO Reports*, 6(1), 33–38.

Thakurela, S., Garding, A., Jung, R. B., Müller, C., Goebbels, S., White, R., Werner, H. B., et al. (2016). The transcriptome of mouse central nervous system myelin. *Scientific Reports*, 6, 25828.

Theil, K., Imami, K., & Rajewsky, N. (2019). Identification of proteins and miRNAs that specifically bind an mRNA in vivo. *Nature Communications*, 10(1), 4205.

Thomas, M. G., Loschi, M., Desbats, M. A., & Boccaccio, G. L. (2011). RNA granules: the good, the bad and the ugly. *Cellular Signalling*, 23(2), 324–334.

Tian, S., Curnutte, H. A., & Trcek, T. (2020). RNA Granules: A View from the RNA Perspective. *Molecules*, 25(14).

Wan, R., Cheli, V. T., Santiago-González, D. A., Rosenblum, S. L., Wan, Q., & Paez, P. M. (2020). Impaired postnatal myelination in a conditional knockout mouse for the ferritin heavy chain in oligodendroglial cells. *The Journal of Neuroscience*, 40(40), 7609–7624.

Wu, B., Chen, J., & Singer, R. H. (2014). Background free imaging of single mRNAs in live cells using split fluorescent proteins. *Scientific Reports*, 4, 3615.

Ye, J., Wang, Z., Chen, X., Jiang, X., Dong, Z., Hu, S., Li, W., et al. (2020). YTHDF1-enhanced iron metabolism depends on TFRC m6A methylation. *Theranostics*, 10(26), 12072–12089.

Zhang, Z., Guo, M., Li, Y., Shen, M., Kong, D., Shao, J., Ding, H., et al. (2020). RNA-binding protein ZFP36/TTP protects against ferroptosis by regulating autophagy signaling pathway in hepatic stellate cells. *Autophagy*, 16(8), 1482–1505.

Supplementary Information

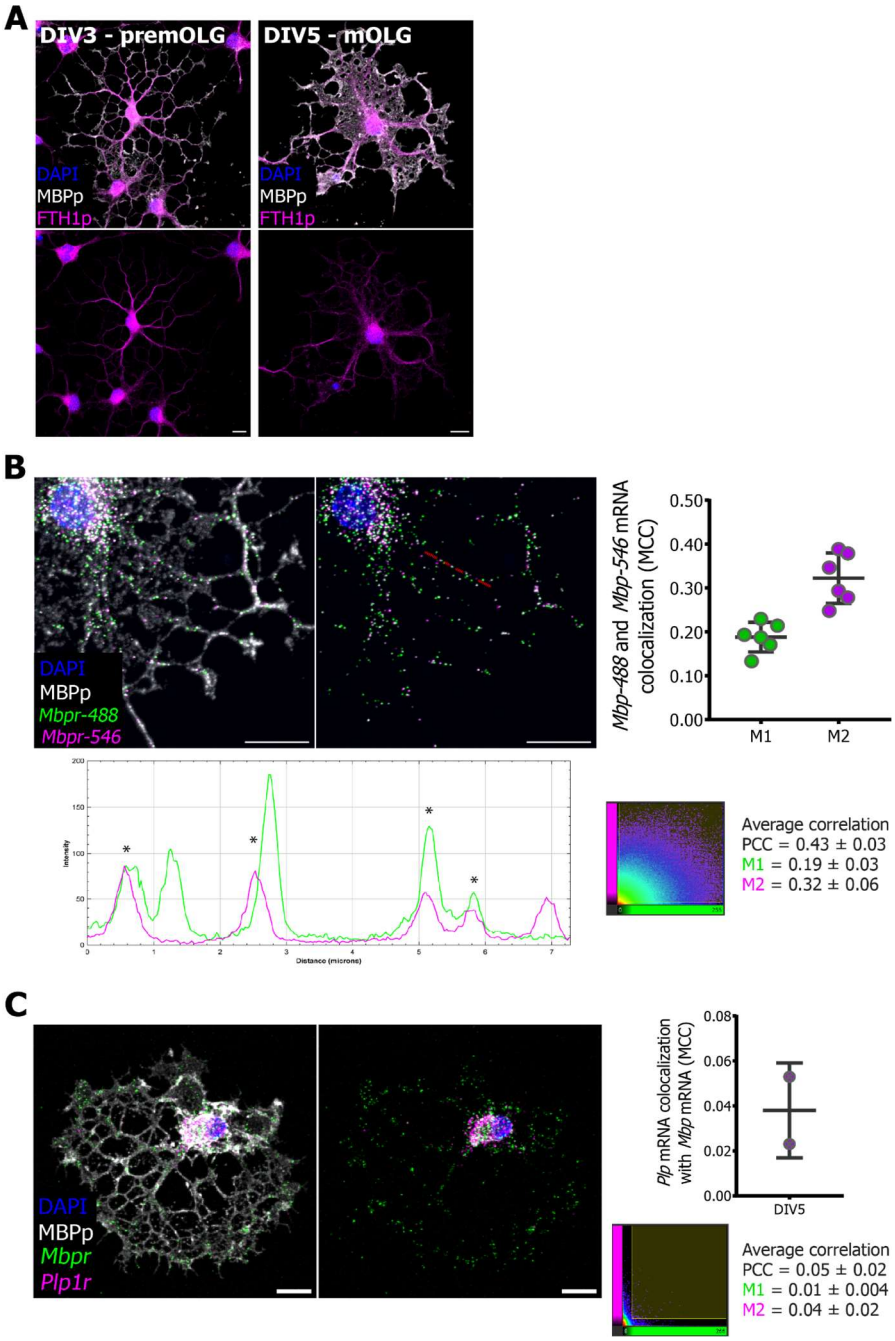

Fig Sup1 - Validation of the *in situ* hybridization (ISH) coupled with protein immunostaining method. (A) Representative images of the antigenicity of MBP (white) and FTH1 (pink) protein in immunocytochemistry of primary mouse oligodendrocytes at the 2 stages of development: pre-mOLGs at DIV3 and mOLGs at DIV5. We confirmed that the antigenicity of the high expressing MBP protein was not considerably affected by the *in situ* hybridization procedure, as judged by the similar signal abundance and distribution of MBP protein in DIV3 and 5 oligodendrocytes with both immunostaining methods (Fig 1A vs Fig Sup1A). Unfortunately, low expressing proteins, such as FTH1 protein, were somewhat affected by the *in situ* hybridization procedure. Which will lead to an overall under representation of RNA-protein colocalization events when using low expressing proteins. Scale bar 10 µm. **(B)** Top: Representative images (left) and MCC co-occurrence quantification (right) of the *in situ* hybridization of two probes targeting the same *Mbp* mRNA transcript region with two distinct fluorophores, Mbpr-488 (green) and Mbpr-546 (pink), together with MBP protein (white) staining at DIV5. Signal overlap between the two RNA probes was

identified in 19 to 32% of puncta. Previous data suggests some level of mRNA probe binding competition due to the low *Mbp* mRNA copy number per granule. Red dotted lines represent the linescan (left bottom) showing the fluorescent intensity (y values) of each probe signal along the oligodendrocyte process (x values are distance in microns). Asterisk shows areas with spatial co-occurrence between the two probes. Bottom right: Representative frequency scatter plot of the fluorescence intensity in the green (Mbp-488, green, x values) and pink (Mbp-546, pink, y values) channels at DIV5. Individual dots in the scatter plot correspond to single pixels of the original picture. The colour code highlights the frequency of dots present in a certain region of the scatter plot (from blue to yellow and red with increasing frequencies). Right, bottom: Average values of the colocalization analysis based on the PCC and MCC at DIV5. The value for PCC ranges from +1 (total positive correlation), 0 (no correlation) and −1 (total negative correlation). The values for MCC occurrence are represented by M1 (green) the fraction of Mbp-488 RNA puncta in areas containing Mbp-546 RNA and M2 (pink) the fraction of Mbp-546 RNA puncta in areas containing Mbp-488 RNA. Data are represented as mean ± SD of 6 biological replicates, as a minimum average of 5 fields of view. Scale bar 10 µm. **(C)** Left: Representative images of the *in situ* hybridization of the *Mbp* (green) and *Plp1* (pink) mRNA probe together with MBP protein (white) staining at DIV5. *Plp1* mRNA was previously described as a non-localising mRNA, thus showing a cell body distribution. On the other hand, *Mbp* mRNA as part of RNP granule, shows a distribution along oligodendrocyte processes and myelin as small puncta. Right: Graphical representation of the MCC measuring the fraction of *Plp1* RNA puncta (pink) in compartments containing *Mbp* RNA puncta (green) at DIV5. Representative frequency scatter plot of the fluorescence intensity in the green (*Mbp*, x values) and pink (*Plp1*, y values) channels at DIV5. Individual dots in the scatter plot correspond to single pixels of the original picture. The colour code highlights the frequency of dots present in a certain region of the scatter plot (from blue to yellow and red with increasing frequencies). Average values of the colocalization analysis based on the PCC and MCC at DIV5. Data are represented as mean ± SD of 2 biological replicates, as a minimum average of 5 fields of view. Scale bar 10 µm.

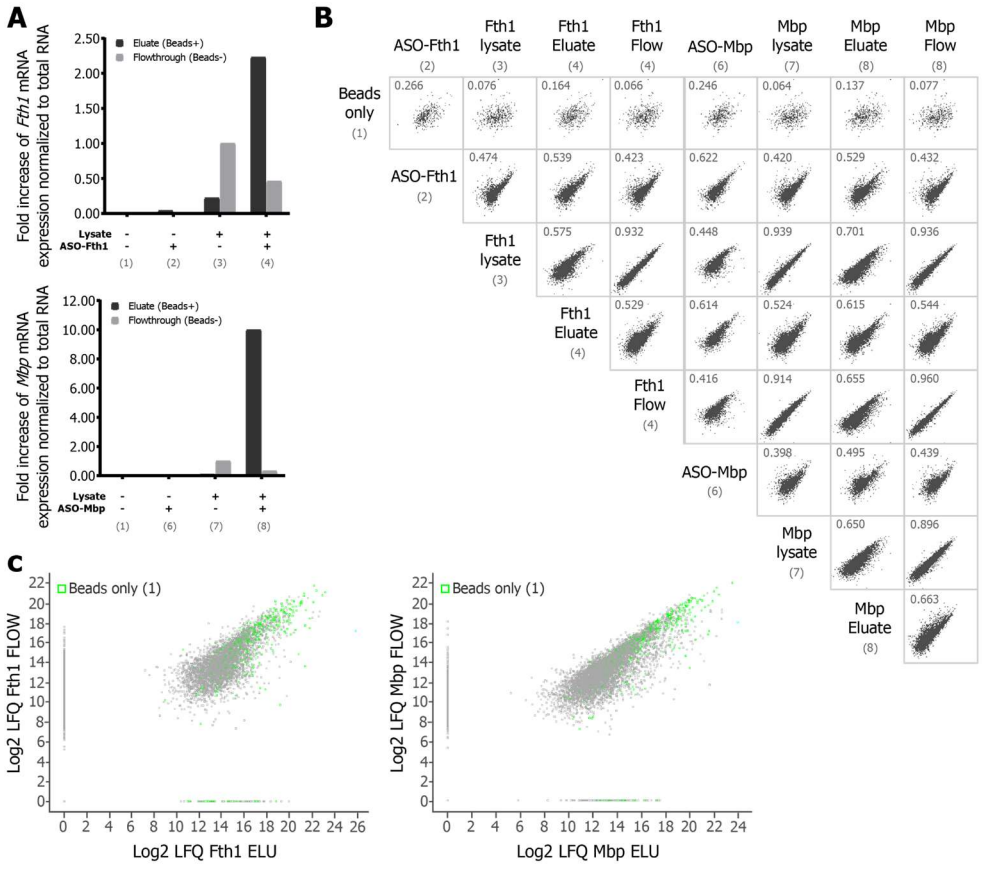

Fig Sup2 - Label-free mass spectrometry-based proteome analysis. (A) Graphical representation of the RNA levels as measured by RT-qPCR in the eluate and flowthrough fractions for all the control and test conditions of the *Fth1* RNA (top) and *Mbp* RNA (bottom) pulldown, normalised to the input total transcript RNA. For every condition beads + (eluate, dark grey) and beads - (flowthrough, light grey) fractions were collected; tested conditions indicate: 1) beads only with no lysate sample and no ASO; 2 and 6) beads and ASO with no lysate sample; 3 and 7) beads with no ASO plus lysate sample, the beads - fraction of this condition is the equivalent to the input; 4 and 8) beads with ASO and lysate, the beads+ fraction of this condition is the targeted sample. RNA-protein crosslinking and targeted mRNA pulldown leads to the capture and enrichment of eluate fractions for the *Fth1* (top) and *Mbp* (bottom) transcripts when using the respective biotinylated antisense oligonucleotides (ASO). Graph bars represent means of 3 technical replicates from the pilot experiment. **(B)** Multi-scatter plot showing correlations between the different samples and controls. Each grey dot represents a single protein in a sample, X-axis and Y-axis represent the log2 transformed protein abundances (log2 LFQ) values for the experimental samples described. R square correlation values (top left corner in grey for each pair of samples) show that the flowthrough and lysate (or input) samples have a high correlation, indicating that most non-specific and contaminant proteins are kept within the flowthrough sample. Similarly, the high correlation values between *Fth1* and *Mbp* lysate samples (2 independent biological samples), show that this pulldown method has a high degree of technical repeatability. **(C)** Scatter plot of the proteins identified in the *Fth1* (left) and *Mbp* (right) fractions. The data is expressed as the log2 LFQ of all proteins in eluate and flowthrough fractions, and plotted against one another in the x- and y-axes, respectively. Green-coded dots represent proteins also identified within the beads only control (1). As expected, many of the beads only, green-coded proteins appear within the eluate fractions, reflecting the nature of the unspecific binding of these proteins to the sepharose beads. Proteins identified within the beads only fraction were then excluded from further analysis.

Table Sup1 - Collection of protein binding motifs identified in the *Mbp* mRNA sequence through the BRIO web server (Guarracino et al. 2021). Columns indicate (from left to right): the protein domain associated to the RNA structure motif; the type of motif structural or sequence based; region or position of the motif in the set of RNA molecules in which the motif was originally identified; p-value determined by Fisher's Test to assess if a motif is enriched in the input RNA molecules with respect to a set of background RNAs; the protein associated to the RNA secondary motif in the CLIP experiment analysed; the experiment type in which the motif was identified eCLIP PAR-CLIP and HITS.

Domains	Type	Region	p-value	Protein	Experiment
RRM	Sequence	CDS	0.034	Rbfox	HITSCLIP
RRM	Sequence	CDS	0.036	SRSF2	HITSCLIP
PAZ; Piwi	Sequence	CDS	0.028	Ago2	HITSCLIP
-	Sequence	CDS	0.037	DGCR8	HITSCLIP
RRMx1; RRMx2; RRMx3	Sequence	CDS	0.018	HuR	PARCLIP
RRM	Sequence	CDS	0.034	C17ORF85	PARCLIP
RRMx1; Znf_RanBP2x1	Sequence	CDS	0.03	TAF15	PARCLIP
RRMx1; RRMx2; RRMx3	Sequence	CDS	0.041	ELAVL1A	PARCLIP
RRMx1; RRMx2; RRMx3	Sequence	CDS	0.034	ELAVL1MNASE	PARCLIP
-	Sequence	CDS	0.031	PUM2	PARCLIP

Znf_CCCHx5	Sequence	CDS	0.042	ZC3H7B	PARCLIP
G-patch; RRMx1; RRMx2	Sequence	CDS	0.017	RBM10	PARCLIP
RRMx1; RRMx2	Sequence	CDS	0.018	NONO	eCLIP
-	Sequence	CDS	0.017	UTP18	eCLIP
RRM; SAP	Sequence	CDS	0.024	SLTM	eCLIP
G-patch	Sequence	CDS	0.034	SUGP2	eCLIP
-	Sequence	CDS	0.034	SRSF1	eCLIP
RRMx1; RRMx2; RRMx3; SPOC	Sequence	CDS	0.0091	RBM15	eCLIP
-	Sequence	CDS	0.048	FXR2	eCLIP
-	Sequence	CDS	0.026	U2AF1	eCLIP
KHx1; KHx2; KHx3	Sequence	CDS	0.0094	PCBP1	eCLIP
-	Sequence	CDS	0.039	UCHL5	eCLIP
DRBM; Helicase|ATP-binding & C-terminal	Sequence	CDS	0.009	DHX30	eCLIP
LisH	Sequence	CDS	0.032	NOLC1	eCLIP
-	Sequence	CDS	0.021	AKAP8L	eCLIP
RRM	Sequence	CDS	0.032	FUS	eCLIP
-	Sequence	CDS	0.04	FXR1	eCLIP
Helicase|ATP-binding; Helicase|C-terminal	Sequence	CDS	0.021	DDX6	eCLIP
AAA_11; AAA_12; ResIII; UPF1-type	Sequence	CDS	0.0068	UPF1	eCLIP
-	Sequence	CDS	0.032	WDR43	eCLIP
-	Sequence	CDS	0.00022	GRWD1	eCLIP
-	Sequence	CDS	0.015	EXOSC5	eCLIP
KHx4	Sequence	CDS	0.043	KHSRP	eCLIP
-	Sequence	CDS	0.0029	QKI	eCLIP
Ribosomal_S3_C	Sequence	CDS	0.041	RPS3	eCLIP
RRM	Sequence	CDS	0.0073	RBFOX2	eCLIP
-	Sequence	CDS	0.0055	FASTKD2	eCLIP
-	Sequence	CDS	0.028	APOBEC3C	eCLIP
-	Sequence	CDS	0.015	TBRG4	eCLIP

RRMx1; RRMx2	Sequence	CDS	0.0089	SRSF9	eCLIP
RRMx1; RRMx2	Sequence	CDS	0.0026	MATR3	eCLIP
RRM	Sequence	CDS	0.0079	NCBP2	eCLIP
-	Sequence	CDS	0.0075	AKAP1	eCLIP
RRMx2	Sequence	CDS	0.02	HNRNPL	eCLIP
-	Sequence	CDS	0.048	PRPF8	eCLIP
KHx1; KHx2; KHx3; KHx4; RRMx1; RRMx2	Sequence	CDS	0.036	IGF2BP2	eCLIP
Znf_CCCHx4	Sequence	transcript	0.01	Mbnl1	HITSCLIP
AAA_11; AAA_12; ResIII; UPF1-type	Sequence	transcript	0.0083	UPF1	eCLIP
MPN	Sequence	transcript	0.047	EIF3H	eCLIP
-	Sequence	transcript	0.014	EFTUD2	eCLIP
Helicase|ATP-binding; Helicase|C-terminal	Sequence	transcript	0.016	DDX42	eCLIP
RRMx1; RRMx2	Sequence	transcript	0.024	SF3B4	eCLIP
CSDx1; Znf_CCHCx2	Sequence	transcript	0.016	LIN28B	eCLIP
KHx1; KHx2; KHx3; KHx4; RRMx1; RRMx2	Sequence	transcript	0.013	IGF2BP2	eCLIP
-	Sequence	transcript	0.0019	PRPF8	eCLIP
-	Sequence	transcript	0.046	DDX55	eCLIP
-	Sequence	transcript	0.025	EIF3D	eCLIP
-	Sequence	transcript	0.013	DGCR8	eCLIP
-	Sequence	transcript	0.0088	TBRG4	eCLIP
RRM	Sequence	transcript	0.025	EIF3G	eCLIP
-	Sequence	transcript	0.013	SMNDC1	eCLIP
RRM; RRMx1	Sequence	transcript	0.0037	CSTF2T	eCLIP
-	Sequence	transcript	0.039	ZNF622	eCLIP
-	Sequence	transcript	0.044	SUPV3L1	eCLIP
RRMx2	Sequence	transcript	0.0015	HNRNPA1	eCLIP
-	Sequence	transcript	0.029	GRWD1	eCLIP
-	Sequence	transcript	0.0097	NOL12	eCLIP
-	Sequence	transcript	0.015	YWHAG	eCLIP

HTH; RRM	Sequence	transcript	0.027	LARP4	eCLIP
RRMx1; RRMx2; RRMx3	Sequence	transcript	0.0064	U2AF2	eCLIP
-	Sequence	transcript	0.033	FXR2	eCLIP
Znf_CCCHx3	Sequence	transcript	0.023	ZC3H11A	eCLIP
Ribosomal_S3_C	Sequence	transcript	0.016	RPS3	eCLIP
Znf_CCCHx4	Sequence	UTR	0.007	Mbnl1	HITSCLIP
Znf_CCCHx4	Sequence	UTR	0.01	Mbnl2	HITSCLIP
CSDx1; Znf_CCHCx2	Sequence	UTR	0.028	LIN28	CLIPSeq
PAZ; Piwi	Sequence	UTR	0.016	AGO2	HITSCLIP
G3BP1-binding	Sequence	UTR	0.044	CAPRIN1	PARCLIP
RRMx1; RRMx2; RRMx3	Sequence	UTR	0.035	ELAVL1MNASE	PARCLIP
Znf_CCCHx5	Sequence	UTR	0.016	ZC3H7B	PARCLIP
-	Sequence	UTR	0.016	LSM11	eCLIP
CSDx1; Znf_CCHCx2	Sequence	UTR	0.017	LIN28B	eCLIP
-	Sequence	UTR	0.0037	EFTUD2	eCLIP
Ribosomal_S3_C	Sequence	UTR	0.025	RPS3	eCLIP
-	Sequence	UTR	0.003	DDX55	eCLIP
-	Sequence	UTR	0.016	PHF6	eCLIP
G-patch; KOWx1; KOWx2	Sequence	UTR	0.016	GPKOW	eCLIP
RRMx1; RRMx2	Sequence	UTR	0.016	SF3B4	eCLIP
-	Sequence	UTR	0.012	NIPBL	eCLIP
Helicase|ATP-binding; Helicase|C-terminal	Sequence	UTR	0.0057	HLTF	eCLIP
RRMx1	Sequence	UTR	0.046	PABPN1	eCLIP
-	Sequence	UTR	0.032	BUD13	eCLIP
-	Sequence	UTR	0.036	CPEB4	eCLIP
-	Sequence	UTR	0.0037	FASTKD2	eCLIP
-	Sequence	UTR	0.011	NOL12	eCLIP
Znf_RanBP2x2	Sequence	UTR	0.033	ZRANB2	eCLIP
KHx1; KHx2; KHx3; KHx4; RRMx1; RRMx2	Sequence	UTR	0.024	IGF2BP2	eCLIP
RRMx1; RRMx2; RRMx3; SPOC	Sequence	UTR	0.038	RBM15	eCLIP

KHx1; KHx2; KHx3; KHx4; RRMx1; RRMx2	Sequence	UTR	0.035	IGF2BP1	eCLIP
-	Sequence	UTR	0.014	AQR	eCLIP
-	Sequence	UTR	0.012	PUM1	eCLIP
-	Sequence	UTR	0.044	FAM120A	eCLIP
-	Sequence	UTR	0.0097	METAP2	eCLIP
-	Sequence	UTR	0.0085	PPIG	eCLIP
-	Sequence	UTR	0.025	CDC40	eCLIP
Helicase|ATP-binding; Helicase|C-terminal	Sequence	UTR	0.036	DDX52	eCLIP
-	Sequence	UTR	0.0079	FXR2	eCLIP
RRMx1; RRMx2; RRMx3	Sequence	UTR	0.0038	U2AF2	eCLIP
RRM	Sequence	UTR	0.049	EIF3G	eCLIP
RRM	Sequence	UTR	0.012	TRA2A	eCLIP
RRMx3	Sequence	UTR	0.033	HNRNPM	eCLIP
KHx1; KHx2; KHx3	Sequence	UTR	0.003	PCBP1	eCLIP
-	Sequence	UTR	0.047	UCHL5	eCLIP
-	Sequence	UTR	0.019	AKAP1	eCLIP
TROVEx1	Sequence	UTR	0.042	TROVE2	eCLIP
-	Sequence	UTR	0.0046	EIF3D	eCLIP
HTH; RRM	Sequence	UTR	0.028	LARP4	eCLIP
-	Sequence	UTR	0.013	WDR43	eCLIP
AAA_11; AAA_12; ResIII; UPF1-type	Sequence	UTR	0.019	UPF1	eCLIP
CXC; SET	Sequence	UTR	0.017	EZH2	PARCLIP
RRMx1; Znf_RanBP2x1	Structure	CDS	0.024	TAF15	PARCLIP
CSDx1; Znf_CCHCx2	Structure	CDS	0.048	LIN28B	PARCLIP
RRMx1; Znf_RanBP2	Structure	CDS	0.014	EWSR1	PARCLIP
RRMx1; RRMx2; RRMx3	Structure	CDS	0.019	HuR	PARCLIP
RRMx1; RRMx2; RRMx3	Structure	CDS	0.0082	U2AF2	eCLIP
-	Structure	CDS	0.03	FASTKD2	eCLIP
-	Structure	CDS	0.03	PRPF4	eCLIP

-	Structure	CDS	0.0068	PCBP2	eCLIP
-	Structure	CDS	0.0052	SMNDC1	eCLIP
RRMx1; RRMx2; RRMx3; RRMx4	Structure	CDS	0.041	PTBP1	eCLIP
AAA_11; AAA_12; ResIII; UPF1-type	Structure	CDS	0.049	UPF1	eCLIP
-	Structure	CDS	0.031	FMR1	eCLIP
RRMx1	Structure	CDS	0.024	HNRNPC	eCLIP
RRMx2	Structure	CDS	0.0041	HNRNPL	eCLIP
Helicase|ATP-binding & C-terminal	Structure	CDS	0.048	DDX3X	eCLIP
-	Structure	CDS	0.0089	QKI	eCLIP
-	Structure	CDS	0.013	SFPQ	eCLIP
RRMx1; RRMx2	Structure	CDS	0.0092	MATR3	eCLIP
-	Structure	CDS	0.037	FTO	eCLIP
KHx1; KHx2; KHx3; KHx4	Structure	CDS	0.048	FUBP3	eCLIP
-	Structure	CDS	0.0036	TBRG4	eCLIP
KHx3	Structure	CDS	0.014	HNRNPK	eCLIP
-	Structure	CDS	0.043	UTP18	eCLIP
-	Structure	transcript	0.011	QKI	eCLIP
KHx3	Structure	transcript	0.012	HNRNPK	eCLIP
TROVEx1	Structure	transcript	0.026	TROVE2	eCLIP
RRMx1; RRMx2	Structure	transcript	0.023	MATR3	eCLIP
-	Structure	transcript	0.041	UTP3	eCLIP
-	Structure	transcript	0.016	WDR3	eCLIP
RRMx2	Structure	transcript	0.0042	HNRNPL	eCLIP
KHx1	Structure	transcript	0.019	KHDRBS1	eCLIP
RRM	Structure	transcript	0.02	NCBP2	eCLIP
FHA; G-patch	Structure	transcript	0.012	AGGF1	eCLIP
-	Structure	transcript	0.031	PRPF8	eCLIP
RRMx1; RRMx2; RRMx3	Structure	transcript	0.014	U2AF2	eCLIP
RRMx1	Structure	transcript	0.032	HNRNPC	eCLIP

G-patch; R3H	Structure	transcript	0.049	NKRF	eCLIP
-	Structure	transcript	0.0084	TBRG4	eCLIP
-	Structure	transcript	0.042	UTP18	eCLIP
RRM	Structure	transcript	0.031	TRA2A	eCLIP
KHx1; KHx2; KHx3; KHx4; RRMx1; RRMx2	Structure	transcript	0.017	IGF2BP1	eCLIP
KHx1; KHx2; KHx3	Structure	UTR	0.016	Nova	HITSCLIP
RRMx1; RRMx2; RRMx3	Structure	UTR	0.017	HuR	PARCLIP
RRM	Structure	UTR	0.042	FUS	PARCLIP
RRMx1; Znf_RanBP2	Structure	UTR	0.036	EWSR1	PARCLIP
PAZ; Piwi	Structure	UTR	0.016	AGO2	PARCLIP
-	Structure	UTR	0.024	FXR2	PARCLIP
RRMx2	Structure	UTR	0.014	HNRNPL	HITSCLIP
RRM; SAP	Structure	UTR	0.043	SLTM	eCLIP
-	Structure	UTR	0.037	HNRNPUL1	eCLIP
RRMx1; RRMx2; RRMx3	Structure	UTR	0.037	U2AF2	eCLIP
KHx1; KHx2; KHx3; KHx4; RRMx1; RRMx2	Structure	UTR	0.018	IGF2BP1	eCLIP
-	Structure	UTR	0.031	SDAD1	eCLIP
-	Structure	UTR	0.005	PCBP2	eCLIP
G-patch; R3H;	Structure	UTR	0.024	NKRF	eCLIP
-	Structure	UTR	0.027	BCCIP	eCLIP
KHx3	Structure	UTR	0.015	HNRNPK	eCLIP
-	Structure	UTR	0.03	WDR43	eCLIP
PPIase|cyclophilin-type; RRM	Structure	UTR	0.024	PPIL4	eCLIP
-	Structure	UTR	0.032	HNRNPU	eCLIP
RRM	Structure	UTR	0.024	NCBP2	eCLIP
-	Structure	UTR	0.024	QKI	eCLIP
RRMx1; RRMx2	Structure	UTR	0.034	MATR3	eCLIP
-	Structure	UTR	0.0089	DDX59	eCLIP
-	Structure	UTR	0.039	SERBP1	eCLIP
DRBM; Helicase|ATP-binding &	Structure	UTR	0.027	DHX30	eCLIP

C-terminal					
KHx1; KHx2; KHx3	Structure	UTR	0.015	PCBP1	eCLIP
RRMx1; RRMx2; RRMx3; RRMx4	Structure	UTR	0.018	PTBP1	eCLIP
DRBMx1; DRBMx2; DZF	Structure	UTR	0.016	ILF3	eCLIP

Table Sup2 - Collection of protein binding motifs identified in the *Fth1* mRNA sequence through the BRIO web server (Guarracino et al. 2021). Columns indicate (from left to right): the protein domain associated to the RNA structure motif; the type of motif structural or sequence based; region or position of the motif in the set of RNA molecules in which the motif was originally identified; p-value determined by Fisher's Test to assess if a motif is enriched in the input RNA molecules with respect to a set of background RNAs; the protein associated to the RNA secondary motif in the CLIP experiment analysed; the experiment type in which the motif was identified eCLIP PAR-CLIP and HITS.

Domains	Type	Region	p-value	Protein	Experiment
RRM	Sequence	CDS	0.034	Rbfox	HITSCLIP
Znf_CCCHx4	Sequence	CDS	0.041	Mbnl1	HITSCLIP
-	Sequence	CDS	0.034	SRSF1	eCLIP
RRMx1; RRMx2; RRMx3; SPOC	Sequence	CDS	0.0098	RBM15	eCLIP
-	Sequence	CDS	0.032	WDR43	eCLIP
KHx4	Sequence	CDS	0.043	KHSRP	eCLIP
-	Sequence	CDS	0.019	NIPBL	eCLIP
Ribosomal_S3_C	Sequence	CDS	0.041	RPS3	eCLIP
TROVEx1	Sequence	CDS	0.024	TROVE2	eCLIP
-	Sequence	CDS	0.0055	FASTKD2	eCLIP
AAA_11; AAA_12; ResIII; UPF1-type	Sequence	CDS	0.03	UPF1	eCLIP
-	Sequence	CDS	0.033	AKAP1	eCLIP
RRMx1; RRMx2; RRMx3	Sequence	CDS	0.045	U2AF2	eCLIP
RRM	Sequence	CDS	0.0079	NCBP2	eCLIP
Helicase|ATP-binding; Helicase|C-terminal	Sequence	CDS	0.016	HLTF	eCLIP
RRMx2	Sequence	CDS	0.02	HNRNPL	eCLIP
-	Sequence	transcript	0.046	DDX55	eCLIP

-	Sequence	transcript	0.0088	TBRG4	eCLIP
RRM	Sequence	transcript	0.025	EIF3G	eCLIP
-	Sequence	transcript	0.012	SUPV3L1	eCLIP
-	Sequence	transcript	0.029	GRWD1	eCLIP
HTH; RRM	Sequence	transcript	0.029	LARP4	eCLIP
-	Sequence	transcript	0.046	NOL12	eCLIP
Znf_CCCHx3	Sequence	transcript	0.023	ZC3H11A	eCLIP
CSDx1; Znf_CCHCx2	Sequence	UTR	0.028	LIN28	CLIPSeq
Znf_CCCHx4;	Sequence	UTR	0.016	Mbnl1	HITSCLIP
-	Sequence	UTR	0.039	DGCR8	HITSCLIP
PAZ; Piwi	Sequence	UTR	0.027	Ago2MNase	PARCLIP
G3BP1-binding;	Sequence	UTR	0.044	CAPRIN1	PARCLIP
RRMx1; RRMx2; RRMx3	Sequence	UTR	0.045	HuR	PARCLIP
-	Sequence	UTR	0.013	RBM22	eCLIP
KHx1; KHx2; KHx3; KHx4; RRMx1; RRMx2	Sequence	UTR	0.0076	IGF2BP2	eCLIP
KHx1;KHx2;KHx3;KHx4;RRMx1;RRMx2;	Sequence	UTR	0.031	IGF2BP3	eCLIP
-	Sequence	UTR	0.038	BUD13	eCLIP
HTH; RRM	Sequence	UTR	0.034	LARP4	eCLIP
-	Sequence	UTR	0.032	BUD13	eCLIP
RRM	Sequence	UTR	0.0051	NCBP2	eCLIP
RRMx1	Sequence	UTR	0.0081	PABPN1	eCLIP
RRMx1; RRMx2; RRMx3	Sequence	UTR	0.047	TIA1	eCLIP
-	Sequence	UTR	0.011	METAP2	eCLIP
RRMx1; RRMx2; RRMx3; SPOC	Sequence	UTR	0.038	RBM15	eCLIP

KHx1; KHx2; KHx3; KHx4; RRMx1; RRMx2;	Sequence	UTR	0.035	IGF2BP1	eCLIP
-	Sequence	UTR	0.01	FXR2	eCLIP
-	Sequence	UTR	0.044	FAM120A	eCLIP
-	Sequence	UTR	0.0085	PPIG	eCLIP
-	Sequence	UTR	0.03	ZC3H8	eCLIP
CSDx1; Znf_CCHCx2	Structure	CDS	0.048	LIN28B	PARCLIP
-	Structure	CDS	0.03	PRPF4	eCLIP
-	Structure	CDS	0.031	FASTKD2	eCLIP
AAA_11; AAA_12; ResIII; UPF1-type	Structure	CDS	0.049	UPF1	eCLIP
-	Structure	CDS	0.031	FMR1	eCLIP
Helicase|ATP-binding; Helicase|C-terminal	Structure	CDS	0.048	DDX3X	eCLIP
-	Structure	CDS	0.046	RBM22	eCLIP
-	Structure	CDS	0.037	FTO	eCLIP
DRBMx1; DRBMx2; DZF	Structure	CDS	0.013	ILF3	eCLIP
-	Structure	transcript	0.00095	PUS1	eCLIP
G-patch; R3H	Structure	transcript	0.049	NKRF	eCLIP
-	Structure	transcript	0.042	UTP18	eCLIP
RRM	Structure	transcript	0.041	NCBP2	eCLIP
RRM; SAP	Structure	UTR	0.043	SLTM	eCLIP
G-patch; R3H	Structure	UTR	0.024	NKRF	eCLIP
RRM	Structure	UTR	0.024	NCBP2	eCLIP
-	Structure	UTR	0.038	HNRNPUL1	eCLIP
-	Structure	UTR	0.039	SERBP1	eCLIP

Discussion

Oligodendrocytes have active roles in axonal maintenance and survival (Nave 2010), neuronal circuitry modulation and adaptation (Tomassy et al. 2014; Mount and Monje 2017; Moore et al. 2020), and even immunomodulatory functions (Falcão et al. 2018). Not surprisingly, oligodendrocyte and/or myelin disturbances are often associated with neuropathologies and neurodevelopmental disorders (Stadelmann et al. 2019; Nasrabady et al. 2018; Lorente Pons et al. 2020; Cassoli et al. 2015). In light of these paradigm shifting findings, it is perplexing that we are still detailing some of the most basic properties of OLGs. Many factors have contributed to the knowledge gaps associated with these cells, among them the complicated and sometimes inefficient protocols for the isolation of primary cells, especially from adult brains; the lack of defined stage specific markers and the lack of adequate transgenic tools that would allow the manipulation of these cells *in vitro*. With improved technology and a renewed interest, the scientific community has recently begun to address many long-held questions. Indeed, new technological developments such as human OLGs derived from iPSCs could provide a scalable, renewable and easier to gene edit source of cells. Such access would increase our ability to interrogate the oligodendrocyte physiology and provide insights into how these cells contribute to axonal survival and brain homeostasis.

To establish protocols to efficiently and reproducibly generate human OLGs from iPSCs, I conducted a comparative study. Given the inconsistency of the results from different laboratories and the lack of standardisation and benchmarking, iPSC derived iOLGs are not a widely accessible resource. As a first step towards establishing iOLG best practices, we established a transgenic approach to compared differentiation efficiency between two previously described methodologies overexpressing oligodendrocyte specific transcription factors. I showed that significant efficiency variations were found between the transcription factors that cannot be reduced to differences in neuronal differentiation methodology, media composition or donor variability. Overexpression of SOX10 solely allows the expression of both O4 and MBP expressing oligodendrocytes, but these cells show a more immature morphology and low yields. On the other hand, the combination of three transcription factors, SOX10, OLIG2, and NKX6.2, greatly improved the differentiation efficiency. Suggesting that the OLG differentiation regulatory network might be sensitive to an imbalance between SOX10 and OLIG2 gene expression. Moreover, by including a purification step I significantly improved oligodendrocyte differentiation yields and reduced the population heterogeneity, which will facilitate the application of these cells in bulk experiments, for example. Furthermore, using this platform, I demonstrated—for the first time to our knowledge—that human myelinating oligodendrocytes show the granular expression of *Mbp* mRNA. This indicates that human myelin development is regulated in part by the translocation and local translation of *Mbp* mRNA, which demonstrates the feasibility of modelling the mechanisms of human

oligodendrocyte myelin formation and maintenance *in vitro* using this platform. The preliminary results showcasing the myelinating capacity of iOLGs in *in vitro* co-culture systems of iPSC-derived cortical neurons, astrocytes and microglia is particularly exciting. Such a 3D multicellular models would enable easy access and manipulation of the different brain cell types, while maintaining a microenvironment that can better approximate the appropriate brain cytoarchitecture. Overall, iPSC-derived OLGs are a useful tool for studying many aspects of oligodendrocyte biology and through co-culture systems potentially investigate axonal targeting, network maturation, activity regulated myelination, axonal-oligodendroglial and glia-glia interactions, to name a few examples.

Ultimately, the development of reliable and cost-effective human iPSC-derived oligodendrocyte models will have a lasting impact in the field, especially in drug development and clinical trials. Afterall, more than 90% of promising therapeutic compounds for Multiple Sclerosis, fail to reproduce the effects when tested in patients (’t Hart et al. 2021), which is at least in part likely resulting from the inherent inter-species differences observed between mice and human oligodendrocytes in signalling factors response (Bradl and Lassmann 2010) and remyelination response after myelin damage (Franklin et al. 2021). Unfortunately, the elevated costs and time necessary to obtain iPSC derived OLGs reduce its accessibility to many research groups. By overexpressing oligodendrocyte specific transcription factors, we can greatly reduce the differentiation time and increase the differentiation efficiency, when compared to morphogen-based cell specification (Chanoumidou et al. 2020). Such a fast development will have implications in the cells ability to completely mimic the native cell phenotypes. Indeed, we observed that iOLGs overexpressing SON do not express PDGFRA, a well-known OPC marker. This suggests that the forced cell differentiation takes place without the generation of some intermediate progenitor cell types, similar to what has been shown for transdifferentiation methods (Vierbuchen and Wernig 2011). And even though these cells have been shown to have a global gene profile similar to primary human oligodendrocytes, it is unclear what degree of cellular authenticity and maturity can be achieved with these protocols (Ehrlich et al. 2017; García-León et al. 2018). Current characterisation studies of human iPSC derived OLGs are rather superficial and typically restricted to observations of myelination events in mouse xenografts and in infrequent and ambiguous myelin-like events in human co-culture systems or organoids (Rodrigues et al. 2017; Marton et al. 2019; Shaker et al. 2021; Li et al. 2016; Douvaras et al. 2014). Further research is needed to fully characterise the nature of iOLGs differentiated via the ectopic expression of transcription factors and how these compare to the native cortical and spinal cord-derived oligodendrocytes. Using data driven approaches such as single cell RNA sequencing, we can have a better understanding of these cells' genetic and metabolic profile throughout differentiation. This data will help inform the best strategies for future method development and its appropriate experimental applications. Moreover, it is important to establish clear criteria for what constitutes mature myelin formations by showing: I) the physiologically appropriate thickness and II) the formation of compactly wrapped myelin lamellae through electron microscopy; III) and the presence

of the proper structural organisation into discrete nodal and paranodal domains of the myelinated axons, by immunocytochemistry (James et al. 2021). In summary, providing unbiased benchmarking criteria for reproducibility and robustness of iPSC derived OLGs, will promote and facilitate the wide utilisation of these cells and help define its suitability for disease modelling and drug screens.

The second component of this thesis directly relates to the wider knowledge gap of the mechanism of axonal support by myelinating oligodendrocytes. Upon neuronal iron-mediated cytotoxicity, oligodendrocytes secrete ferritin heavy chain protein, which can potentially be internalised by neighbouring neurons. The FTH1 protein will then protect the neurons by storing and detoxifying excess intracellular iron (Mukherjee et al. 2020). Evidence from previous studies indicates that FTH1 does not behave like a myelin-resident protein and further corroborates a cytoprotective function for FTH1 in post-myelinating cells (Mukherjee et al. 2020; Ward et al. 2014; Wan et al. 2020). Moreover, the presence of high levels of an *Fth1* mRNA isoform with 3' UTR in the myelin sheath (Thakurela et al. 2016; Gould et al. 2000) could suggest a mechanism for the active transport of this transcript, followed by its local translation and secretion.

I aimed to characterise the nature of the *Fth1* transcript in myelin and identify the RNA-binding proteins that promote its localization or translation repression. I observed that *Fth1* mRNA and FTH1 protein content increased throughout oligodendrocyte differentiation in both mouse and human oligodendrocytes. *Fth1* mRNA shows the characteristic granular distribution along the distal processes, reminiscent of other locally repressed mRNAs. I also showed that *Fth1* mRNA is not associated with P-bodies or stress granules in mature oligodendrocytes, instead the *Fth1* mRNA puncta appears to be a unique type of RNA granule in oligodendrocytes. I further developed a proteomics approach to selectively isolate native RNA-protein complexes, and identify potential interacting RNPs involved in the transport and translational repression of *Fth1* mRNA in mature oligodendrocytes. Using this approach, I identified 19 potential RNPs candidates that could be associated with *Fth1* mRNA translocation and/or translation repression in oligodendrocytes. Further experiments are needed to validate the identified proteins as *Fth1* mRNA binding partners in mature oligodendrocytes. For example, the live imaging of fluorescently-labelled RNP proteins or their chemical inhibition, while imaging labelled *Fth1* mRNA (MS2-fluorescence complementation (Wu et al. 2014; Park et al. 2020)) should provide additional insights into RNA granule specific transport. Methods to visualise local translation of nascent proteins (Na et al. 2016) would provide exciting new insights into if and how the intracellular sorting of *Fth1* mRNA can be regulated by intercellular communication with neurons. Unfortunately, such labelling systems are complex to implement when little is known about the RNP binding location in the mRNA sequence, which coupled with the low transfection potential of primary mouse oligodendrocytes has made it particularly challenging to establish such techniques. However, human iOLGs derived from iPSCs could provide an alternative source of mature and myelinating cells that is easier to genetically manipulate, which will facilitate RNA

granules research. Overall, our understanding of the different mRNA-RNP complexes and their roles in oligodendrocytes is still lacking. Moreover, it remains to be established whether local protein translation plays a role in neuronal-induced exosome secretion. Nevertheless, the *Fth1* mRNA and protein expression in myelin suggests the existence of a previously unknown RNA trafficking mechanism. Additional clues about the functional characteristics of *Fth1* mRNA granules will likely come from studies targeting its interacting RNP proteins. Certainly, the RNP protein candidates identified in the *Fth1* mRNA specific pulldown are an important clue in this regard. Our results have provided the foundation for additional insights into the function of *Fth1* mRNA granules and associated proteins in oligodendrocytes.

Despite recent research efforts, many aspects governing the mRNA dynamics of localising mRNAs in the brain remain unknown. In oligodendrocytes, research has centred in HNRNPA2/B1 granules complexes together with *Mbp* and *Mobp* mRNAs. Little is known about other potential RNPs and localising mRNA in oligodendrocytes, which is surprising as localising RNAs were first described in this cell type (Kristensson et al. 1986; Colman et al. 1982; Ainger et al. 1993). In neurons, localising mRNAs can be found at synapses and have been shown to play a role in synaptic plasticity, learning and memory (Kelleher et al. 2004). Newly synthesised mRNA transcripts are selectively targeted to active synapses, where they mediate the local synthesis of proteins that become part of the synapse (Steward and Worley 2001). This is a very interesting finding confirming that not only are mRNAs associated with RNPs for directed transport, but there are specific signalling mechanisms that can regulate and distinguish between RNA-RNP complex populations. As oligodendrocytes can ensheathment multiple axons, a similar signalling mechanism could provide an effective way for oligodendrocytes to rapidly respond to neuronal stimuli, by directing the targeted mRNA translocation, translation and protein secretion at the specific myelin edge that is interacting with the injured axonal process. An important challenge will be to identify which mRNA binding proteins are responsive to neuronal activity or cytotoxic cues. Future work will have to unravel the protein composition of RNA granules and to determine their function. This knowledge will ultimately result in a better understanding of how exactly a granule with a specific composition is assembled and which cellular states trigger, maintain, or dismantle the RNP granule. Undoubtedly, future discoveries will lead to a number of interesting findings that will alter our view of RNA granule biology in brain cells.

References

Ainger, K., Avossa, D., Morgan, F., Hill, S. J., Barry, C., Barbarese, E., & Carson, J. H. (1993). Transport and localization of exogenous myelin basic protein mRNA microinjected into oligodendrocytes. The *Journal of Cell Biology*, 123(2), 431–441.

Andrews, M. G., & Nowakowski, T. J. (2019). Human brain development through the lens of cerebral organoid models. *Brain Research*, 1725, 146470.

Aprato, J., Sock, E., Weider, M., Elsesser, O., Fröb, F., & Wegner, M. (2020). Myrf guides target gene selection of transcription factor Sox10 during oligodendroglial development. *Nucleic Acids Research*, 48(3), 1254–1270.

Barbarese, E., Koppel, D. E., Deutscher, M. P., Smith, C. L., Ainger, K., Morgan, F., & Carson, J. H. (1995). Protein translation components are colocalized in granules in oligodendrocytes. *Journal of Cell Science*, 108 (Pt 8), 2781–2790.

Baron, W., Ozgen, H., Klunder, B., de Jonge, J. C., Nomden, A., Plat, A., Trifilieff, E., et al. (2015). The major myelin-resident protein PLP is transported to myelin membranes via a transcytotic mechanism: involvement of sulfatide. *Molecular and Cellular Biology*, 35(1), 288–302.

Barres, B. A. (2008). The mystery and magic of glia: a perspective on their roles in health and disease. *Neuron*, 60(3), 430–440.

Batish, M., van den Bogaard, P., Kramer, F. R., & Tyagi, S. (2012). Neuronal mRNAs travel singly into dendrites. *Proceedings of the National Academy of Sciences of the United States of America*, 109(12), 4645–4650.

Besse, F., & Ephrussi, A. (2008). Translational control of localized mRNAs: restricting protein synthesis in space and time. Nature Reviews. *Molecular Cell Biology*, 9(12), 971–980.

Bradl, M., & Lassmann, H. (2010). Oligodendrocytes: biology and pathology. *Acta Neuropathologica*, 119(1), 37–53.

Briscoe, J., Sussel, L., Serup, P., Hartigan-O'Connor, D., Jessell, T. M., Rubenstein, J. L., & Ericson, J. (1999). Homeobox gene Nkx2.2 and specification of neuronal identity by graded Sonic hedgehog signalling. *Nature*, 398(6728), 622–627.

Burke, K. S., Antilla, K. A., & Tirrell, D. A. (2017). A Fluorescence in Situ Hybridization Method To Quantify mRNA Translation by Visualizing Ribosome-mRNA Interactions in Single Cells. *ACS central science*, 3(5), 425–433.

Cassoli, J. S., Guest, P. C., Malchow, B., Schmitt, A., Falkai, P., & Martins-de-Souza, D. (2015). Disturbed macro-connectivity in schizophrenia linked to oligodendrocyte dysfunction: from structural findings to molecules. *Schizophrenia*, 1, 15034.

Chamling, X., Kallman, A., Fang, W., Berlinicke, C. A., Mertz, J. L., Devkota, P., Pantoja, I. E. M., et al. (2021). Single-cell transcriptomic reveals molecular diversity and developmental heterogeneity of human stem cell-derived oligodendrocyte lineage cells. *Nature Communications*, 12(1), 652.

Chanoumidou, K., Hernández-Rodríguez, B., Windener, F., Thomas, C., Stehling, M., Mozafari, S., Albrecht, S., et al. (2021). One-step Reprogramming of Human Fibroblasts into Oligodendrocyte-like Cells by SOX10, OLIG2, and NKX6.2. *Stem cell reports*, 16(4), 771–783.

Chanoumidou, K., Mozafari, S., Baron-Van Evercooren, A., & Kuhlmann, T. (2020). Stem cell derived oligodendrocytes to study myelin diseases. *Glia*, 68(4), 705–720.

Colman, D. R., Kreibich, G., Frey, A. B., & Sabatini, D. D. (1982). Synthesis and incorporation of myelin polypeptides into CNS

myelin. *The Journal of Cell Biology*, 95(2 Pt 1), 598–608.

Crichton, R. R., Dexter, D. T., & Ward, R. J. (2012). Brain iron metabolism and its perturbation in neurological diseases. In W. Linert & H. Kozlowski (Eds.), *Metal ions in neurological systems* (pp. 1–15).

Czepiel, M., Boddeke, E., & Copray, S. (2015). Human oligodendrocytes in remyelination research. *Glia*, 63(4), 513–530.

Czopka, T., Ffrench-Constant, C., & Lyons, D. A. (2013). Individual oligodendrocytes have only a few hours in which to generate new myelin sheaths in vivo. *Developmental Cell*, 25(6), 599–609.

De Kleijn, K. M. A., Zuure, W. A., Peijnenborg, J., Heuvelmans, J. M., & Martens, G. J. M. (2019). Reappraisal of human HOG and MO3.13 cell lines as a model to study oligodendrocyte functioning. *Cells*, 8(9).

Douvaras, P., & Fossati, V. (2015). Generation and isolation of oligodendrocyte progenitor cells from human pluripotent stem cells. *Nature Protocols*, 10(8), 1143–1154.

Douvaras, P., Wang, J., Zimmer, M., Hanchuk, S., O'Bara, M. A., Sadiq, S., Sim, F. J., et al. (2014). Efficient generation of myelinating oligodendrocytes from primary progressive multiple sclerosis patients by induced pluripotent stem cells. *Stem cell reports*, 3(2), 250–259.

Doyle, M., & Kiebler, M. A. (2011). Mechanisms of dendritic mRNA transport and its role in synaptic tagging. *The EMBO Journal*, 30(17), 3540–3552.

Du, Y., & Dreyfus, C. F. (2002). Oligodendrocytes as providers of growth factors. *Journal of Neuroscience Research*, 68(6), 647–654.

Duncan, G. J., Simkins, T. J., & Emery, B. (2021). Neuron-Oligodendrocyte Interactions in the Structure and Integrity of Axons. *Frontiers in cell and developmental biology*, 9, 653101.

Ehrlich, M., Mozafari, S., Glatza, M., Starost, L., Velychko, S., Hallmann, A.-L., Cui, Q.-L., et al. (2017). Rapid and efficient generation of oligodendrocytes from human induced pluripotent stem cells using transcription factors. *Proceedings of the National Academy of Sciences of the United States of America*, 114(11), E2243–E2252.

Emery, B., & Dugas, J. C. (2013). Purification of oligodendrocyte lineage cells from mouse cortices by immunopanning. *Cold Spring Harbor Protocols*, 2013(9), 854–868.

Emery, B., Agalliu, D., Cahoy, J. D., Watkins, T. A., Dugas, J. C., Mulinyawe, S. B., Ibrahim, A., et al. (2009). Myelin gene regulatory factor is a critical transcriptional regulator required for CNS myelination. *Cell*, 138(1), 172–185.

Falcão, A. M., van Bruggen, D., Marques, S., Meijer, M., Jäkel, S., Agirre, E., Samudyata, et al. (2018). Disease-specific oligodendrocyte lineage cells arise in multiple sclerosis. *Nature Medicine*, 24(12), 1837–1844.

Fard, M. K., van der Meer, F., Sánchez, P., Cantuti-Castelvetri, L., Mandad, S., Jäkel, S., Fornasiero, E. F., et al. (2017). BCAS1 expression defines a population of early myelinating oligodendrocytes in multiple sclerosis lesions. *Science Translational Medicine*, 9(419).

Franklin, R. J. M., Frisén, J., & Lyons, D. A. (2021). Revisiting remyelination: Towards a consensus on the regeneration of CNS myelin. Seminars in Cell & Developmental Biology, 116, 3–9.

Frühbeis, C., Fröhlich, D., Kuo, W. P., Amphornrat, J., Thilemann, S., Saab, A. S., Kirchhoff, F., et al. (2013). Neurotransmitter-triggered transfer of exosomes mediates oligodendrocyte-neuron communication. *PLoS Biology*, 11(7).

Gao, Y., Tatavarty, V., Korza, G., Levin, M. K., & Carson, J. H. (2008). Multiplexed dendritic targeting of alpha calcium calmodulin-dependent protein kinase II, neurogranin, and

activity-regulated cytoskeleton-associated protein RNAs by the A2 pathway. *Molecular Biology of the Cell*, 19(5), 2311–2327.

García-León, J. A., García-Díaz, B., Eggermont, K., Cáceres-Palomo, L., Neyrinck, K., Madeiro da Costa, R., Dávila, J. C., et al. (2020). Generation of oligodendrocytes and establishment of an all-human myelinating platform from human pluripotent stem cells. *Nature Protocols*, 15(11), 3716–3744.

García-León, J. A., Kumar, M., Boon, R., Chau, D., One, J., Wolfs, E., Eggermont, K., et al. (2018). SOX10 Single Transcription Factor-Based Fast and Efficient Generation of Oligodendrocytes from Human Pluripotent Stem Cells. *Stem cell reports,* 10(2), 655–672.

Gautier, H. O. B., Evans, K. A., Volbracht, K., James, R., Sitnikov, S., Lundgaard, I., James, F., et al. (2015). Neuronal activity regulates remyelination via glutamate signalling to oligodendrocyte progenitors. *Nature Communications*, 6, 8518.

Goldman, S. A., & Kuypers, N. J. (2015). How to make an oligodendrocyte. *Development*, 142(23), 3983–3995.

Gould, R. M., Freund, C. M., Palmer, F., & Feinstein, D. L. (2000). Messenger RNAs located in myelin sheath assembly sites. *Journal of Neurochemistry*, 75(5), 1834–1844.

Gunkel, N., Yano, T., Markussen, F. H., Olsen, L. C., & Ephrussi, A. (1998). Localization-dependent translation requires a functional interaction between the 5' and 3' ends of oskar mRNA. *Genes & Development*, 12(11), 1652–1664.

Hill, R. A., Li, A. M., & Grutzendler, J. (2018). Lifelong cortical myelin plasticity and age-related degeneration in the live mammalian brain. *Nature Neuroscience*, 21(5), 683–695.

Jahn, O., Tenzer, S., & Werner, H. B. (2009). Myelin proteomics: molecular anatomy of an insulating sheath. *Molecular Neurobiology*, 40(1), 55–72.

Jäkel, S., Agirre, E., Mendanha Falcão, A., van Bruggen, D., Lee, K. W., Knuesel, I., Malhotra, D., et al. (2019). Altered human oligodendrocyte heterogeneity in multiple sclerosis. *Nature*, 566(7745), 543–547.

Jakovcevski, I., Filipovic, R., Mo, Z., Rakic, S., & Zecevic, N. (2009). Oligodendrocyte development and the onset of myelination in the human fetal brain. *Frontiers in Neuroanatomy*, 3, 5.

James, O. G., Selvaraj, B. T., Magnani, D., Burr, K., Connick, P., Barton, S. K., Vasistha, N. A., et al. (2021). iPSC-derived myelinoids to study myelin biology of humans. *Developmental Cell*, 56(9), 1346-1358.e6.

Jung, M., Krämer, E., Grzenkowski, M., Tang, K., Blakemore, W., Aguzzi, A., Khazaie, K., et al. (1995). Lines of Murine Oligodendroglial Precursor Cells Immortalized by an Activatedneu Tyrosine Kinase Show Distinct Degrees of Interaction with AxonsIn Vitro andIn Vivo. *European Journal of Neuroscience*, 7(6), 1245–1265.

Kelleher, R. J., Govindarajan, A., Jung, H.-Y., Kang, H., & Tonegawa, S. (2004). Translational control by MAPK signaling in long-term synaptic plasticity and memory. *Cell*, 116(3), 467–479.

Kim, H., Xu, R., Padmashri, R., Dunaevsky, A., Liu, Y., Dreyfus, C. F., & Jiang, P. (2019). Pluripotent Stem Cell-Derived Cerebral Organoids Reveal Human Oligodendrogenesis with Dorsal and Ventral Origins. *Stem cell reports*, 12(5), 890–905.

Kristensson, K., Holmes, K. V., Duchala, C. S., Zeller, N. K., Lazzarini, R. A., & Dubois-Dalcq, M. (1986). Increased levels of myelin basic protein transcripts in virus-induced demyelination. *Nature*, 322(6079), 544–547.

Kuhn, S., Gritti, L., Crooks, D., & Dombrowski, Y. (2019). Oligodendrocytes in development, myelin generation and beyond. *Cells*, 8(11).

Küspert, M., Hammer, A., Bösl, M. R., & Wegner, M. (2011). Olig2 regulates Sox10 expression in oligodendrocyte precursors through an evolutionary conserved distal enhancer. *Nucleic Acids Research*, 39(4), 1280–1293.

Lee, S., Leach, M. K., Redmond, S. A., Chong, S. Y. C., Mellon, S. H., Tuck, S. J., Feng, Z.-Q., et al. (2012). A culture system to study oligodendrocyte myelination processes using engineered nanofibers. *Nature Methods*, 9(9), 917–922.

Li, P., Li, M., Tang, X., Wang, S., Zhang, Y. A., & Chen, Z. (2016). Accelerated generation of oligodendrocyte progenitor cells from human induced pluripotent stem cells by forced expression of Sox10 and Olig2. Science China. *Life sciences*, 59(11), 1131–1138.

Lorente Pons, A., Higginbottom, A., Cooper-Knock, J., Alrafiah, A., Alofi, E., Kirby, J., Shaw, P. J., et al. (2020). Oligodendrocyte pathology exceeds axonal pathology in white matter in human amyotrophic lateral sclerosis. *The Journal of Pathology*, 251(3), 262–271.

Lyons, D. A., Naylor, S. G., Scholze, A., & Talbot, W. S. (2009). Kif1b is essential for mRNA localization in oligodendrocytes and development of myelinated axons. *Nature Genetics*, 41(7), 854–858.

Madhavan, M., Nevin, Z. S., Shick, H. E., Garrison, E., Clarkson-Paredes, C., Karl, M., Clayton, B. L. L., et al. (2018). Induction of myelinating oligodendrocytes in human cortical spheroids. *Nature Methods*, 15(9), 700–706.

Marton, R. M., Miura, Y., Sloan, S. A., Li, Q., Revah, O., Levy, R. J., Huguenard, J. R., et al. (2019). Differentiation and maturation of oligodendrocytes in human three-dimensional neural cultures. *Nature Neuroscience*, 22(3), 484–491.

Mikl, M., Vendra, G., & Kiebler, M. A. (2011). Independent localization of MAP2, CaMKIIα and β-actin RNAs in low copy numbers. *EMBO Reports*, 12(10), 1077–1084.

Mitew, S., Hay, C. M., Peckham, H., Xiao, J., Koenning, M., & Emery, B. (2014). Mechanisms regulating the development of oligodendrocytes and central nervous system myelin. *Neuroscience*, 276, 29–47.

Moore, S., Meschkat, M., Ruhwedel, T., Trevisiol, A., Tzvetanova, I. D., Battefeld, A., Kusch, K., et al. (2020). A role of oligodendrocytes in information processing. *Nature Communications*, 11(1), 5497.

Mount, C. W., & Monje, M. (2017). Wrapped to Adapt: Experience-Dependent Myelination. *Neuron*, 95(4), 743–756.

Mukherjee, C., Kling, T., Russo, B., Miebach, K., Kess, E., Schifferer, M., Pedro, L. D., et al. (2020). Oligodendrocytes provide antioxidant defense function for neurons by secreting ferritin heavy chain. *Cell Metabolism*, 32(2), 259-272.e10.

Müller, C., Bauer, N. M., Schäfer, I., & White, R. (2013). Making myelin basic protein -from mRNA transport to localized translation. *Frontiers in Cellular Neuroscience*, 7, 169.

Munro, T. P., Magee, R. J., Kidd, G. J., Carson, J. H., Barbarese, E., Smith, L. M., & Smith, R. (1999). Mutational analysis of a heterogeneous nuclear ribonucleoprotein A2 response element for RNA trafficking. *The Journal of Biological Chemistry*, 274(48), 34389–34395.

Na, Y., Park, S., Lee, C., Kim, D.-K., Park, J. M., Sockanathan, S., Huganir, R. L., et al. (2016). Real-Time Imaging Reveals Properties of Glutamate-Induced Arc/Arg 3.1 Translation in Neuronal Dendrites. *Neuron*, 91(3), 561–573.

Nasrabady, S. E., Rizvi, B., Goldman, J. E., & Brickman, A. M. (2018). White matter changes in Alzheimer's disease: a focus on myelin and oligodendrocytes. *Acta neuropathologica communications*, 6(1), 22.

Nave, K.-A. (2010). Myelination and the trophic support of long axons. *Nature Reviews. Neuroscience*, 11(4), 275–283.

Nave, K.-A., & Werner, H. B. (2021). Ensheathment and myelination of axons: evolution of glial functions. *Annual Review of Neuroscience*, 44, 197–219.

Nery, S., Wichterle, H., & Fishell, G. (2001). Sonic hedgehog contributes to oligodendrocyte specification in the mammalian forebrain. *Development*, 128(4), 527–540.

Pang, Y., Zheng, B., Kimberly, S. L., Cai, Z., Rhodes, P. G., & Lin, R. C. S. (2012). Neuron-oligodendrocyte myelination co-culture derived from embryonic rat spinal cord and cerebral cortex. *Brain and behavior*, 2(1), 53–67.

Park, S. Y., Moon, H. C., & Park, H. Y. (2020). Live-cell imaging of single mRNA dynamics using split superfolder green fluorescent proteins with minimal background. *RNA*, 26(1), 101–109.

Patzig, J., Jahn, O., Tenzer, S., Wichert, S. P., de Monasterio-Schrader, P., Rosfa, S., Kuharev, J., et al. (2011). Quantitative and integrative proteome analysis of peripheral nerve myelin identifies novel myelin proteins and candidate neuropathy loci. *The Journal of Neuroscience*, 31(45), 16369–16386.

Pawlowski, M., Ortmann, D., Bertero, A., Tavares, J. M., Pedersen, R. A., Vallier, L., & Kotter, M. R. N. (2017). Inducible and Deterministic Forward Programming of Human Pluripotent Stem Cells into Neurons, Skeletal Myocytes, and Oligodendrocytes. *Stem cell reports*, 8(4), 803–812.

Percy, M. E., Wong, S., Bauer, S., Liaghati-Nasseri, N., Perry, M. D., Chauthaiwale, V. M., Dhar, M., et al. (1998). Iron metabolism and human ferritin heavy chain cDNA from adult brain with an elongated untranslated region: new findings and insights. *The Analyst*, 123(1), 41–50.

Ponka, P. (1999). Cellular iron metabolism. Kidney International. Supplement, 69, S2-11.

Rodrigues, G. M. C., Gaj, T., Adil, M. M., Wahba, J., Rao, A. T., Lorbeer, F. K., Kulkarni, R. U., et al. (2017). Defined and Scalable Differentiation of Human Oligodendrocyte Precursors from Pluripotent Stem Cells in a 3D Culture System. *Stem cell reports*, 8(6), 1770–1783.

Saab, A. S., Tzvetanova, I. D., & Nave, K.-A. (2013). The role of myelin and oligodendrocytes in axonal energy metabolism. *Current Opinion in Neurobiology*, 23(6), 1065–1072.

Saab, A. S., Tzvetavona, I. D., Trevisiol, A., Baltan, S., Dibaj, P., Kusch, K., Möbius, W., et al. (2016). Oligodendroglial NMDA receptors regulate glucose import and axonal energy metabolism. *Neuron*, 91(1), 119–132.

Schäfer, I., Müller, C., Luhmann, H. J., & White, R. (2016). MOBP levels are regulated by Fyn kinase and affect the morphological differentiation of oligodendrocytes. *Journal of Cell Science*, 129(5), 930–942.

Shaker, M. R., Pietrogrande, G., Martin, S., Lee, J.-H., Sun, W., & Wolvetang, E. J. (2021). Rapid and efficient generation of myelinating human oligodendrocytes in organoids. *Frontiers in Cellular Neuroscience*, 15, 631548.

Simons, M., & Nave, K.-A. (2015). Oligodendrocytes: myelination and axonal support. Cold Spring Harbor *Perspectives in Biology*, 8(1), a020479.

Snaidero, N., Velte, C., Myllykoski, M., Raasakka, A., Ignatev, A., Werner, H. B., Erwig, M. S., et al. (2017). Antagonistic functions of MBP and CNP establish cytosolic channels in CNS myelin. *Cell reports*, 18(2), 314–323.

Stadelmann, C., Timmler, S., Barrantes-Freer, A., & Simons, M. (2019). Myelin in the central nervous system: structure, function, and pathology. *Physiological Reviews*, 99(3), 1381–1431.

Stassart, R. M., Möbius, W., Nave, K.-A., & Edgar, J. M. (2018). The Axon-Myelin Unit in

Development and Degenerative Disease. *Frontiers in Neuroscience*, 12, 467.

Steward, O., & Worley, P. F. (2001). A cellular mechanism for targeting newly synthesized mRNAs to synaptic sites on dendrites. *Proceedings of the National Academy of Sciences of the United States of America,* 98(13), 7062–7068.

't Hart, B. A., Luchicchi, A., Schenk, G. J., Killestein, J., & Geurts, J. J. G. (2021). Multiple sclerosis and drug discovery: A work of translation. *EBioMedicine*, 68, 103392.

Thakurela, S., Garding, A., Jung, R. B., Müller, C., Goebbels, S., White, R., Werner, H. B., et al. (2016). The transcriptome of mouse central nervous system myelin. *Scientific Reports*, 6, 25828.

Tomassy, G. S., Berger, D. R., Chen, H.-H., Kasthuri, N., Hayworth, K. J., Vercelli, A., Seung, H. S., et al. (2014). Distinct profiles of myelin distribution along single axons of pyramidal neurons in the neocortex. *Science*, 344(6181), 319–324.

Tong, C. K., Fuentealba, L. C., Shah, J. K., Lindquist, R. A., Ihrie, R. A., Guinto, C. D., Rodas-Rodriguez, J. L., et al. (2015). A Dorsal SHH-Dependent Domain in the V-SVZ Produces Large Numbers of Oligodendroglial Lineage Cells in the Postnatal Brain. *Stem cell reports*, 5(4), 461–470.

Torvund-Jensen, J., Steengaard, J., Reimer, L., Fihl, L. B., & Laursen, L. S. (2014). Transport and translation of MBP mRNA is regulated differently by distinct hnRNP proteins. *Journal of Cell Science*, 127(Pt 7), 1550–1564.

van Tilborg, E., de Theije, C. G. M., van Hal, M., Wagenaar, N., de Vries, L. S., Benders, M. J., Rowitch, D. H., et al. (2018). Origin and dynamics of oligodendrocytes in the developing brain: Implications for perinatal white matter injury. *Glia*, 66(2), 221–238.

Vierbuchen, T., & Wernig, M. (2011). Direct lineage conversions: unnatural but useful? *Nature Biotechnology,* 29(10), 892–907.

Wake, H., Lee, P. R., & Fields, R. D. (2011). Control of local protein synthesis and initial events in myelination by action potentials. *Science*, 333(6049), 1647–1651.

Wan, R., Cheli, V. T., Santiago-González, D. A., Rosenblum, S. L., Wan, Q., & Paez, P. M. (2020). Impaired postnatal myelination in a conditional knockout mouse for the ferritin heavy chain in oligodendroglial cells. *The Journal of Neuroscience*, 40(40), 7609–7624.

Ward, R. J., Zucca, F. A., Duyn, J. H., Crichton, R. R., & Zecca, L. (2014). The role of iron in brain ageing and neurodegenerative disorders. *Lancet Neurology*, 13(10), 1045–1060.

White, R., Gonsior, C., Krämer-Albers, E.-M., Stöhr, N., Hüttelmaier, S., & Trotter, J. (2008). Activation of oligodendroglial Fyn kinase enhances translation of mRNAs transported in hnRNP A2-dependent RNA granules. *The Journal of Cell Biology*, 181(4), 579–586.

Wilson, H. C., Onischke, C., & Raine, C. S. (2003). Human oligodendrocyte precursor cells in vitro: phenotypic analysis and differential response to growth factors. *Glia*, 44(2), 153–165.

Wolf, N. I., Ffrench-Constant, C., & van der Knaap, M. S. (2021). Hypomyelinating leukodystrophies - unravelling myelin biology. Nature Reviews. *Neurology*, 17(2), 88–103.

Wu, B., Chen, J., & Singer, R. H. (2014). Background free imaging of single mRNAs in live cells using split fluorescent proteins. *Scientific Reports*, 4, 3615.

Xiao, L., Ohayon, D., McKenzie, I. A., Sinclair-Wilson, A., Wright, J. L., Fudge, A. D., Emery, B., et al. (2016). Rapid production of new oligodendrocytes is required in the earliest stages of motor-skill learning. *Nature Neuroscience*, 19(9), 1210–1217.

Yeung, M. S. Y., Zdunek, S., Bergmann, O., Bernard, S., Salehpour, M., Alkass, K., Perl, S., et al. (2014). Dynamics of oligodendrocyte generation and myelination in the human brain. *Cell*, 159(4), 766–774.

Zalc, B. (2016). The acquisition of myelin: An evolutionary perspective. *Brain Research*, 1641 (Pt A), 4–10.

List of figures

List of tables

List of abbreviations

A2RE	A2 response element
AAVS1	Adeno-Associated Virus Integration Site 1
ASO	RNA antisense oligonucleotides
BCAS1	breast carcinoma amplified sequence 1
Bio	Biotin
BL	Brain lysate
CAGpro	chicken beta-actin promoter
cAMP	N6,2′-O-Dibutyryladenosine 3′,5′-cyclic monophosphate sodium salt
CNP	2', 3'-cyclic nucleotide 3'-phosphodiesterase
CNS	Central nervous system
DCP1A	mRNA-decapping enzyme 1A
DIV	Days *in vitro*
Dox	Doxycycline
Elu	eluate
endo	Endogenous expression
ENPP6	ectonucleotide pyrophosphatase/phosphodiesterase 6
FGF2	fibroblast growth factor 2
Flow	flowthrough
FLP	flippase
FRT	flippase recognition target
FTH1	Ferritin heavy chain
G3BP1	Ras-GAP SH3 binding protein 1
GAPDH	Glyceraldehyde 3-phosphate dehydrogenase
GFAP	astrocytic marker glial fibrillary acidic protein
GFP	Green Fluorescent Protein
GO	gene ontology

HGF	hepatocyte growth factor
HNRNPA2	heterogeneous nuclear ribonucleoprotein A2
HNRNPE1	heterogeneous nuclear ribonucleoprotein E1
HYG-TK	hygromycin-resistance/thymidine kinase selection cassette
IGF	insulin growth factor
iOLG	iPSC derived oligodendrocyte
iPSC	Induced pluripotent stem cell
IRE	iron regulatory element
IRES	Internal ribosome entry site
IRP	iron responsive element binding proteins
ISH	*in situ* hybridization
KW	UniProt keywords
LFQ	label-free quantification
m2rtTA	reverse tetracycline controlled transactivator
MACS	magnetic-activated cell sorting
MAG	myelin-associated glycoprotein
MBP	Myelin basic protein
MCC	Mander's correlation coefficient
MCL	master cell line
MKI67	Marker Of Proliferation Ki-67
MOG	Myelin oligodendrocyte glycoprotein
mOLG	Myelinating oligodendrocyte
My	Myelin fractions
MYRF	myelin regulatory factor
NANOG	Homeobox Transcription Factor Nanog
NKX2.2	NK2 homeobox 2
NKX6.2	NK6 Homeobox 2
NMDA	N-methyl-D-aspartate receptor

NPC	Neuronal precursor cell
NT3	neurotrophin 3
OCT4	Octamer-binding transcription factor 4
OLG	Oligodendrocytes
OLG-TF	Oligodendrocyte specific transcription factors
OLIG2	oligodendrocyte transcription factor 2
OPC	Oligodendrocyte precursor cell
over	overexpression
PAX6	Paired box protein 6
P-bodies	processing bodies
PCC	Pearson's correlation coefficient
pcw	Post conception weeks (human)
PDGFRA	platelet-derived growth factor receptor alpha
PLP1	Proteolipid protein
pre-mOLG	Pre-myelinating oligodendrocyte
Puro	puromycin resistance cassette
RA	Retinoic acid
RFP	Red Fluorescent Protein
RMCE	recombinase-mediated cassette exchange
RNP	Ribonucleoprotein
RT-qPCR	reverse transcription quantitative real-time polymerase chain reaction
SAG	smoothened agonist
SG	stress granules
SMAD inhibitor	SB431542 and LDN193189
sncRNA715	small non-coding RNA 715
SON	SOX10, OLIG2 and NKX6.2
SOX10	SRY-box 10
SYP	synaptophysin

T3	thyroid hormone
TRE	tetracycline responsive element
UTR	Untranslated regions
XFP	Fluorescent Protein
YFP	Yellow Fluorescent Protein

List of publications

Cantuti-Castelvetri, L.*, Ojha, R.*, **Pedro, L. D.***, Djannatian, M.*, Franz, J.*, Kuivanen, S.*, van der Meer, F., Kallio, K., Kaya, T., Anastasina, M., Smura, T., Levanov, L., Szirovicza, L., Tobi, A., Kallio-Kokko, H., Österlund, P., Joensuu, M., Meunier, F. A., Butcher, S. J., Winkler, M. S., Mollenhauer, B., Helenius, A., Gokce, O., Teesalu, T., Hepojoki, J., Vapalahti, O., Stadelmann, C., Balistreri, G. and Simons, M. (2020) "Neuropilin-1 facilitates SARS-CoV-2 cell entry and infectivity.," *Science*, 370(6518), pp. 856–860. doi: 10.1126/science.abd2985.

Mukherjee, C., Kling, T., Russo, B., Miebach, K., Kess, E., Schifferer, M., **Pedro, L. D.**, Weikert, U., Fard, M. K., Kannaiyan, N., Rossner, M., Aicher, M.-L., Goebbels, S., Nave, K.-A., Krämer-Albers, E.-M., Schneider, A. and Simons, M. (2020) "Oligodendrocytes provide antioxidant defense function for neurons by secreting ferritin heavy chain.," *Cell Metabolism*, 32(2), pp. 259-272.e10. doi: 10.1016/j.cmet.2020.05.019.

Jugdaohsingh, R., **Pedro, L. D.**, Watson, A. and Powell, J. J. (2015) "Silicon and boron differ in their localization and loading in bone." *Bone reports*, 1, pp. 9–15. doi: 10.1016/j.bonr.2014.10.002.

Jugdaohsingh, R., Kessler, K., Messner, B., Stoiber, M., **Pedro, L. D.**, Schima, H., Laufer, G., Powell, J. J. and Bernhard, D. (2015) "Dietary Silicon Deficiency Does Not Exacerbate Diet-Induced Fatty Lesions in Female ApoE Knockout Mice." *The Journal of Nutrition*, 145(7), pp. 1498–1506. doi: 10.3945/jn.114.206193.

Jugdaohsingh, R., Watson, A. I. E., **Pedro, L. D.** and Powell, J. J. (2015) "The decrease in silicon concentration of the connective tissues with age in rats is a marker of connective tissue turnover.," *Bone*, 75, pp. 40–48. doi: 10.1016/j.bone.2015.02.004.

Copyright of figures taken from publications

Introduction: Fig 2

Rights and permissions for Wolf et al. 2021:

SPRINGER NATURE LICENSE
TERMS AND CONDITIONS
Jun 08, 2022

This Agreement between Liliana Pedro ("You") and Springer Nature ("Springer Nature") consists of your license details and the terms and conditions provided by Springer Nature and Copyright Clearance Center.

License Number	5324201427620
License date	Jun 08, 2022
Licensed Content Publisher	Springer Nature
Licensed Content Publication	Nature Reviews Neurology
Licensed Content Title	Hypomyelinating leukodystrophies — unravelling myelin biology
Licensed Content Author	Nicole I. Wolf et al
Licensed Content Date	Dec 15, 2020
Type of Use	Thesis/Dissertation
Requestor type	academic/university or research institute
Format	print and electronic
Portion	figures/tables/illustrations
Number of figures/tables/illustrations	1
High-res required	no
Will you be translating?	no
Circulation/distribution	1 - 29
Author of this Springer Nature content	no
Title	Oligodendrocytes from stem cells to RNA

Institution name	DZNE
Expected presentation date	Jun 2022
Portions	Fig1 B and C
Requestor Location	Liliana Pedro Feodor-Lynen-Strasse 17 Muenchen, 81377 Germany Attn: Ms
Total	0.00 USD

Terms and Conditions

Springer Nature Customer Service Centre GmbH
Terms and Conditions

This agreement sets out the terms and conditions of the licence (the **Licence**) between you and **Springer Nature Customer Service Centre GmbH** (the **Licensor**). By clicking 'accept' and completing the transaction for the material (**Licensed Material**), you also confirm your acceptance of these terms and conditions.

1. Grant of License

1. 1. The Licensor grants you a personal, non-exclusive, non-transferable, world-wide licence to reproduce the Licensed Material for the purpose specified in your order only. Licences are granted for the specific use requested in the order and for no other use, subject to the conditions below.

1. 2. The Licensor warrants that it has, to the best of its knowledge, the rights to license reuse of the Licensed Material. However, you should ensure that the material you are requesting is original to the Licensor and does not carry the copyright of another entity (as credited in the published version).

1. 3. If the credit line on any part of the material you have requested indicates that it was reprinted or adapted with permission from another source, then you should also seek permission from that source to reuse the material.

2. Scope of Licence

2. 1. You may only use the Licensed Content in the manner and to the extent permitted by these Ts&Cs and any applicable laws.

2. 2. A separate licence may be required for any additional use of the Licensed Material, e.g. where a licence has been purchased for print only use, separate

permission must be obtained for electronic re-use. Similarly, a licence is only valid in the language selected and does not apply for editions in other languages unless additional translation rights have been granted separately in the licence. Any content owned by third parties are expressly excluded from the licence.

2. 3. Similarly, rights for additional components such as custom editions and derivatives require additional permission and may be subject to an additional fee. Please apply to Journalpermissions@springernature.com/bookpermissions@springernature.com for these rights.

2. 4. Where permission has been granted **free of charge** for material in print, permission may also be granted for any electronic version of that work, provided that the material is incidental to your work as a whole and that the electronic version is essentially equivalent to, or substitutes for, the print version.

2. 5. An alternative scope of licence may apply to signatories of the STM Permissions Guidelines, as amended from time to time.

3. Duration of Licence

3. 1. A licence for is valid from the date of purchase ('Licence Date') at the end of the relevant period in the below table:

Scope of Licence	**Duration of Licence**
Post on a website	12 months
Presentations	12 months
Books and journals	Lifetime of the edition in the language purchased

4. Acknowledgement

4. 1. The Licensor's permission must be acknowledged next to the Licenced Material in print. In electronic form, this acknowledgement must be visible at the same time as the figures/tables/illustrations or abstract, and must be hyperlinked to the journal/book's homepage. Our required acknowledgement format is in the Appendix below.

5. Restrictions on use

5. 1. Use of the Licensed Material may be permitted for incidental promotional use and minor editing privileges e.g. minor adaptations of single figures, changes of format, colour and/or style where the adaptation is credited as set out in Appendix 1 below. Any other changes including but not limited to, cropping, adapting, omitting material that affect the meaning, intention or moral rights of the author are strictly prohibited.

5. 2. You must not use any Licensed Material as part of any design or trademark.

5. 3. Licensed Material may be used in Open Access Publications (OAP) before publication by Springer Nature, but any Licensed Material must be removed from OAP sites prior to final publication.

6. Ownership of Rights

6. 1. Licensed Material remains the property of either Licensor or the relevant third party and any rights not explicitly granted herein are expressly reserved.

7. Warranty

IN NO EVENT SHALL LICENSOR BE LIABLE TO YOU OR ANY OTHER PARTY OR ANY OTHER PERSON OR FOR ANY SPECIAL, CONSEQUENTIAL, INCIDENTAL OR INDIRECT DAMAGES, HOWEVER CAUSED, ARISING OUT OF OR IN CONNECTION WITH THE DOWNLOADING, VIEWING OR USE OF THE MATERIALS REGARDLESS OF THE FORM OF ACTION, WHETHER FOR BREACH OF CONTRACT, BREACH OF WARRANTY, TORT, NEGLIGENCE, INFRINGEMENT OR OTHERWISE (INCLUDING, WITHOUT LIMITATION, DAMAGES BASED ON LOSS OF PROFITS, DATA, FILES, USE, BUSINESS OPPORTUNITY OR CLAIMS OF THIRD PARTIES), AND WHETHER OR NOT THE PARTY HAS BEEN ADVISED OF THE POSSIBILITY OF SUCH DAMAGES. THIS LIMITATION SHALL APPLY NOTWITHSTANDING ANY FAILURE OF ESSENTIAL PURPOSE OF ANY LIMITED REMEDY PROVIDED HEREIN.

8. Limitations

8. 1. **BOOKS ONLY:**Where 'reuse in a dissertation/thesis' has been selected the following terms apply: Print rights of the final author's accepted manuscript (for clarity, NOT the published version) for up to 100 copies, electronic rights for use only on a personal website or institutional repository as defined by the Sherpa guideline (www.sherpa.ac.uk/romeo/).

8. 2. For content reuse requests that qualify for permission under the STM Permissions Guidelines, which may be updated from time to time, the STM

Permissions Guidelines supersede the terms and conditions contained in this licence.

9. Termination and Cancellation

9. 1. Licences will expire after the period shown in Clause 3 (above).

9. 2. Licensee reserves the right to terminate the Licence in the event that payment is not received in full or if there has been a breach of this agreement by you.

Appendix 1 — Acknowledgements:

For Journal Content:
Reprinted by permission from [**the Licensor**]: [**Journal Publisher** (e.g. Nature/Springer/Palgrave)] [**JOURNAL NAME**] [**REFERENCE CITATION** (Article name, Author(s) Name), [**COPYRIGHT**] (year of publication)

For **Advance Online Publication papers**:
Reprinted by permission from [**the Licensor**]: [**Journal Publisher** (e.g. Nature/Springer/Palgrave)] [**JOURNAL NAME**] [**REFERENCE CITATION** (Article name, Author(s) Name), [**COPYRIGHT**] (year of publication), advance online publication, day month year (doi: 10.1038/sj.[JOURNAL ACRONYM].)

For Adaptations/Translations:
Adapted/Translated by permission from [**the Licensor**]: [**Journal Publisher** (e.g. Nature/Springer/Palgrave)] [**JOURNAL NAME**] [**REFERENCE CITATION** (Article name, Author(s) Name), **[COPYRIGHT**] (year of publication)

Note: For any republication from the British Journal of Cancer, the following credit line style applies:

Reprinted/adapted/translated by permission from [**the Licensor**]: on behalf of Cancer Research UK: : [**Journal Publisher** (e.g. Nature/Springer/Palgrave)] [**JOURNAL NAME**] [**REFERENCE CITATION** (Article name, Author(s) Name), [**COPYRIGHT**] (year of publication)

For **Advance Online Publication** papers:
Reprinted by permission from The [**the Licensor**]: on behalf of Cancer Research UK: [**Journal Publisher** (e.g. Nature/Springer/Palgrave)] [**JOURNAL NAME**] [**REFERENCE CITATION** (Article name, Author(s) Name), [**COPYRIGHT**] (year of publication), advance online publication, day month year (doi: 10.1038/sj.[JOURNAL ACRONYM])

For Book content:
Reprinted/adapted by permission from [**the Licensor**]: [**Book Publisher** (e.g. Palgrave Macmillan, Springer etc) [**Book Title**] by [**Book author**(s)] [**COPYRIGHT**] (year of publication)

Other Conditions:

Version 1.3

Questions? customercare@copyright.com or +1-855-239-3415 (toll free in the US) or +1-978-646-2777.

Introduction: Fig 4 A

Rights and permissions for Thakurela et al. 2016:
This work is licensed under a Creative Commons Attribution 4.0 International License. The images or other third-party material in this article are included in the article's Creative Commons license, unless indicated otherwise in the credit line; if the material is not included under the Creative Commons license, users will need to obtain permission from the license holder to reproduce the material. To view a copy of this license, visit http://creativecommons.org/licenses/by/4.0/

Introduction: Fig 4 B and C

Rights and permissions for Mukherjee et al. 2020:
The below table explains the rights that authors have when they publish with Elsevier, for authors who choose to publish either open access or subscription. These apply to the corresponding author and all co-authors.

Author rights in Elsevier's proprietary journals	**Published open access**	**Published subscription**
Retain patent and trademark rights	√	√
Retain the rights to use their research data freely without any restriction	√	√
Receive proper attribution and credit for their published work	√	√
Re-use their own material in new works without permission or payment (with full acknowledgement of the original article):	√	√

1. Extend an article to book length 2. Include an article in a subsequent compilation of their own work 3. Re-use portions, excerpts, and their own figures or tables in other works.		
Use and share their works for scholarly purposes (with full acknowledgement of the original article): 1. In their own classroom teaching. Electronic and physical distribution of copies is permitted 2. If an author is speaking at a conference, they can present the article and distribute copies to the attendees 3. Distribute the article, including by email, to their students and to research colleagues who they know for their personal use 4. Share and publicize the article via Share Links, which offers 50 days' free access for anyone, without signup or registration 5. Include in a thesis or dissertation (provided this is not published commercially) 6. Share copies of their article privately as part of an invitation-only work group on commercial sites with which the publisher has a hosting agreement	√	√
Publicly share the preprint on any website or repository at any time.	√	√
Publicly share the accepted manuscript on non-commercial sites	√	√ using a CC BY-NC-ND license and usually only after an embargo period (see Sharing Policy for more information)
Publicly share the final published article	√ in line with the author's choice of end user license	×
Retain copyright	√	×

Acknowledgments

I would like to thank my supervisor Prof. Mikael Simons for the opportunity to join his research group for my doctoral studies. I would also like to thank both Prof. Mikael Simons and Prof. Dr. Dominik Paquet for their scientific guidance and fruitful discussions. Furthermore, I would like to thank Prof. Dr. Martin Kerschensteiner and Dr. Fabiana Perocchi for their scientific input into my project in their role as thesis advisor committee.

I would like to thank the "Graduate School of Systemic Neurosciences". I am thankful for being a part of this great program that has provided me with a social community when I first arrived and a support system latter on when the unpredictable happened.

I would like to acknowledge Prof. Dr. Ulrike Gaul. I will forever cherish everything I have learnt and, especially, everyone I have met, during my time as a member of the fly lab.

Many people have supported me in this adventure, I am lucky enough to have an amazing group of friends and colleagues that have been there for me in the good moments, sharing laughs and sunny Apperols. But more importantly they have listened to my concerns and fears, helping and encouraging me to be better personally and professionally. I wish you all the very best the world has to offer.

I special thank you to Sara for all the guidance, to Miro for the IKEA adventures and for always being up to some last-minute dancing, to Andrea and Alessio for the laughs, to Shao for just listening, to Stefano for his keep calm and carry-on attitude, to Christophe for teaching me so much about microscopy and image analysis.

Thank you to Mar, Martina and Kerstin, may the sun shine, the oranges be juicy, the prosecco never run out and the pizza be delivered on time ;). You girls were truly amazing throughout this experience and there were moments I am sure I would not have made it so gracefully without your support.

Thank you to the Alkmini and Gary the lovely Greek ladies, may your beautiful laughs resonate for all eternity. Thank you to Vini and Jianping may you never run out of questions, your curiosity is inspiring. Thank you to Ioannis, Shima and Chaitali for being here in the very beginning teaching me the first steps. Thank you to Seiji for always being willing to stop everything just to help me out. Thank you to Lennart, Martin, Shreya, Swathi and Stephan, you may have just arrived but your presence was felt and your passion for science welcomed.

Thank you to Julien and Dennis for being willing to listen to my constant and sometimes repetitive questions. To Carolina, I did not realise how much I missed speaking and

singing in Portuguese until you arrive, may the Radio Comercial always be with us. To Angelika for all the last minute, late dinners. To Judith, Joey and Sophie, you guys always have the best parties.

Thank you to Veronika, Jaime, Nico, Vilim, Laura, Alex and Anna. You guys were always there for me when I first arrived, you welcomed me with open arms and I will never forget it.

Thank you Ksenia and Drago, you are my favourite foodies with hearts of gold. Thank you for showing me all the great food secrets of Munich. Thank you for being so king hearted and willing to support the causes that matter so much to me.

Thank you, Judi, for everything, your strength is inspiring and I am very proud of all you have conquered. Thank you for your help at any time with any topic. Thank you for all the support, laughs, dance and music sessions and political and artistic debates.

Thank you to everyone from 15x4 Munich, thank you for allowing to be part of this amazing group of hardworking and fun people.

Thank you to my Soapbox Science girls and founding members of a certain yellow secret society: Judi, Cilia and Becky. You girls are amazing and it was such an incredible pleasure to have spent these last few years working and partying with you. To be able to be as serious as we are silly all in the space of second. Johanna thank you for being so king and patient.

Obrigada aos meus pais, Jorge e Rosalina, e irmãos, André e Afonso, o vosso apoio e suporte incondicional durante esta aventura não passou despercebido. Obrigada por tudo, vocês são parte da razão porque eu consegui chegar aqui. Beijinhos.

Affidavit/Eidesstattliche Versicherung

I hereby confirm that the dissertation “Generation of oligodendrocytes and characterization of their role in axonal support” is the result of my own work and that I have only used sources or materials listed and specified in the dissertation.

Hiermit versichere ich an Eides statt, dass ich die vorliegende Dissertation „Generation of oligodendrocytes and characterization of their role in axonal support“ selbstständig angefertigt habe, mich außer der angegebenen keiner weiteren Hilfsmittel bedient und alle Erkenntnisse, die aus dem Schrifttum ganz oder annähernd übernommen sind, als solche kenntlich gemacht und nach ihrer Herkunft unter Bezeichnung der Fundstelle einzeln nachgewiesen habe.

München, 15.06.2022 Liliana Domingues Pedro

Author Contributions

We hereby declare that the following authors contributed to the results of this study in the following manner:

Dominik Paquet, Julien Klimmt and Carolina Cardoso Gonçalves established the iPSCs-derived neuronal and astrocyte differentiation protocols. Julien Klimmt and Carolina Cardoso Gonçalves have also established 3D spheroid co-culture systems.

Gernot Kleinberg and Dominik Paquet developed the microglia differentiation protocol.

Carolina Cardoso Gonçalves provided technical assistance for the setup of the 3D co-culture systems and assisted with image acquisition.

Agata Rhomberg provided technical assistance with RT-qPCRs.

Stephan A. Müller and Stefan F. Lichtenthaler analysed the proteomic profile of selected mRNAs by mass spectrometry and performed the subsequent bioinformatic analysis.

All other experiments, sample preparations, sample processing, sample analysis, statistical analysis and data visualization were performed by Liliana Domingues Pedro.

Yours faithfully,

Munich, 15.06.2022 Liliana Domingues Pedro Prof. Mikael Simons

Curriculum Vitae

Liliana Domingues Pedro

Education

2017 – present PhD SYSTEMIC NEUROSCIENCES
Graduate School of Systemic Neurosciences (GSN) - LMU, Munich, Germany
Project 1: *A comparative study of iPSC derived oligodendrocyte differentiation via transcription factors ectopic expression.*
Project 2*: Characterisation of Fth1 mRNA granules in oligodendrocytes.*
Supervisor: Prof. Dr. Mikael Simons, German Center for Neurodegenerative Diseases (DZNE)

2015 – 2017 PhD SYSTEMIC NEUROSCIENCES
Graduate School of Systemic Neurosciences (GSN) - LMU, Munich, Germany
Project: *Characterisation of a novel bicistronic gene essential for blood brain barrier formation in Drosophila melanogaster*.
Supervisor: Prof. Dr. Ulrike Gaul, Gene Center Munich

2011 – 2013 MSc. MOLECULAR BIOTECHNOLOGY (Grade: 17/20)
University of Aveiro, Portugal & Medical Research Council – Human Nutrition Research, Cambridge, UK
Silicon and vascular health: the role of silicon in the structure and metabolism of ageing connective tissue. (Grade: 18/20)

2008 – 2011 BSc. BIOCHEMISTRY (Grade: 15/20)
University of Aveiro, Portugal
Neuroprotective effects of phenolic compounds in Huntington's disease. (Grade: 18/20)

Work & Research Experience

Aug 2013 – Jul 2014 RESEARCH ASSISTANT
MRC – Human Nutrition Research, UK

Sept 2009 – Sept 2010 UNDERGRADUATE RESEARCH SCHOLARSHIP
Centre for Research in Ceramics and Composite Materials, Portugal
Optimization of bacterial cellulose production for biomedical applications from industrial residues.
Granting institutions: Science and Technology Foundation (FCT) and University of Aveiro. PT.

Fellowships, Awards and Accomplishments

2012 – FULL MEMBER OF THE BOARD OF EUROPEAN STUDENTS OF TECHNOLOGY (BEST)
2009 – CRIOESTUDANTE PROJECT AWARD, Crioestaminal Laboratories, Portugal**.**
2009 – SEMINAR SPEAKER AWARD (First place), University of Aveiro, Department of Chemistry, Portugal.

Volunteer Experience

2017 – Present – Soapbox Science Munich, Munich, Germany
2017 – Present – 15x4 Munich, Munich, Germany
2017 – 2021 – NeuroCamp Munich, Munich, Germany
2014 – 2015 – Caritas Jovem, supported by Caritas Leiria-Fatima, Portugal
2011 – Present – Children's summer camp monitor, supported by Caritas, Portugal.
2010 & 2011 –Universidade de Aveiro Help Line (LUA), University of Aveiro, Portugal.

Publications

Cantuti-Castelvetri, L.*, Ojha, R.*, **Pedro, L. D.***, Djannatian, M.*, Franz, J.*, Kuivanen, S.*, van der Meer, F., Kallio, K., Kaya, T., Anastasina, M., Smura, T., Levanov, L., Szirovicza, L., Tobi, A., Kallio-Kokko, H., Österlund, P., Joensuu, M., Meunier, F. A., Butcher, S. J., Winkler, M. S., Mollenhauer, B., Helenius, A., Gokce, O., Teesalu, T., Hepojoki, J., Vapalahti, O., Stadelmann, C., Balistreri, G. and Simons, M. (2020) "Neuropilin-1 facilitates SARS-CoV-2 cell entry and infectivity.," *Science*, 370(6518), pp. 856–860. doi: 10.1126/science.abd2985.

Mukherjee, C., Kling, T., Russo, B., Miebach, K., Kess, E., Schifferer, M., **Pedro, L. D.**, Weikert, U., Fard, M. K., Kannaiyan, N., Rossner, M., Aicher, M.-L., Goebbels, S., Nave, K.-A., Krämer-Albers, E.-M., Schneider, A. and Simons, M. (2020) "Oligodendrocytes provide antioxidant defense function for neurons by secreting ferritin heavy chain.," *Cell Metabolism*, 32(2), pp. 259-272.e10. doi: 10.1016/j.cmet.2020.05.019.

Jugdaohsingh, R., **Pedro, L. D.**, Watson, A. and Powell, J. J. (2015) "Silicon and boron differ in their localization and loading in bone.," *Bone reports*, 1, pp. 9–15. doi: 10.1016/j.bonr.2014.10.002.

Jugdaohsingh, R., Kessler, K., Messner, B., Stoiber, M., **Pedro, L. D.**, Schima, H., Laufer, G., Powell, J. J. and Bernhard, D. (2015) "Dietary Silicon Deficiency Does Not Exacerbate Diet-Induced Fatty Lesions in Female ApoE Knockout Mice.," *The Journal of Nutrition*, 145(7), pp. 1498–1506. doi: 10.3945/jn.114.206193.

Jugdaohsingh, R., Watson, A. I. E., **Pedro, L. D.** and Powell, J. J. (2015) "The decrease in silicon concentration of the connective tissues with age in rats is a marker of connective tissue turnover.," *Bone*, 75, pp. 40–48. doi: 10.1016/j.bone.2015.02.004.